9-9-2010

The partial molar volume of carbon dioxide in peridotite partial melt at high pressure

Megan Duncan

Megan S. Duncan
Candidate

Earth and Planetary Sciences
Department

This thesis is approved, and it is acceptable in quality and form for publication:

Approved by the Thesis Committee:

Carl B. Agee, Chairperson

Penelope L. King

Rhian Jones

THE PARTIAL MOLAR VOLUME OF CARBON DIOXIDE IN PERIDOTITE PARTIAL MELT AT HIGH PRESSURE

BY

MEGAN S. DUNCAN

BACHELORS GEOLOGY CLEMSON UNIVERSITY 2007

THESIS

Submitted in Partial Fulfillment of the
Requirements for the Degree of

Master of Science
Earth and Planetary Sciences

The University of New Mexico
Albuquerque, New Mexico

July 2010

ACKNOWLEDGMENTS

I would like to thank Mike Spilde and Ara Kooser for their help with detecting carbon with the electron microprobe, Dr. Penny King with her help with FTIR, Dr. Carl Agee for his role as advisor on this project.

THE PARTIAL MOLAR VOLUME OF CARBON DIOXIDE IN PERIDOTITE PARTIAL MELT AT HIGH PRESSURE

BY

MEGAN S. DUNCAN

ABSTRACT OF THESIS

Submitted in Partial Fulfillment of the
Requirements for the Degree of

Master of Science
Earth and Planetary Sciences

The University of New Mexico
Albuquerque, New Mexico

July 2010

The partial molar volume of carbon dioxide in peridotite partial melt at high pressure

Megan S. Duncan

Bachelor of Science, Geology, Clemson University, 2007
Master of Science, Earth and Planetary Sciences, University of New Mexico, 2010

ABSTRACT

The partial molar volume of CO_2 ($\overline{V}_{CO_2}$) in silicate melt was determined for a komatiite composition using high pressure sink/float experiments in a multi-anvil press. The density of the experimental melt at pressure was determined by observing sinking and floating of pure forsterite (Fo100) and 90% forsterite (Fo90) buoyancy markers. Values for $\overline{V}_{CO_2}$ were bracketed at 4.3 GPa (23.71 cm^3/mol) and at 5.5 GPa (22.06 cm^3/mol), normalized to 1850°C. Combining the current data with previous work we now more accurately constrain the compression curve of $\overline{V}_{CO_2}$ over the pressure range of 1 bar to 20 GPa. These data allow the calculation of density at pressure of carbonated silicate melts, such as kimberlite and silica undersaturated alkali basalts, and the determination of their buoyancy and eruptibility.

Table of Contents

List of Figures

List of Tables

Chapter 1

Carbon dioxide is present in the mantle of the Earth and as one of the most abundant volatile species in the Earth, its effect on melt behavior needs to be well understood. The presence of carbon dioxide affects the behavior of mantle melts by lowering their density and solidus and liquidus temperatures; therefore how CO_2 interacts with mantle melts must be studied and understood so that mantle processes can be quantified. One way to quantify the effect of CO_2 on a mantle melt is by determining its partial molar volume ($\overline{V}_{CO_2}$), and how this value changes with pressure. Using an average upper mantle composition, derived from a peridotite partial melt, we have experimentally determined $\overline{V}_{CO_2}$ at upper mantle pressures.

Molar volume cannot be measured directly so we must use a modified version of Equation (1-1), and simple compositions with known densities to calculate $\overline{V}_{CO_2}$. In order to accurately do this, two simple peridotite-derived komatiite compositions were synthesized with similar major element abundances except that one composition had an added 5.7 wt% CO_2. We experimentally determined the densities of each melt, and were able to approximate the $\overline{V}_{CO_2}$ from the differences between the densities of the two compositions.

Molar volume ($\overline{V}$) is an intensive variable that, ideally, is not controlled by the amount of the component, i.e. the number of moles of the component in the system, but can be controlled by changes in the system such as in temperature and pressure. When a melt consists of many liquid oxides, the change in volume that 1 mole of each oxide

imparts on the melt is its partial molar volume ($\overline{V}_i$). If the $\overline{V}_i$ s of all components and their amounts (X_i) are known then the melt density can be calculated using:

$$\rho = \sum_i X_i M_i / X_i \overline{V}_i \qquad \textbf{(1-1)}$$

where ρ is the density of the melt, X_i is the mole fraction of liquid oxide component i, M_i is its gram formula weight, and $\overline{V}_i$ is its partial molar volume (Bottinga and Weill, 1970). For example: CO_2 is a gas at Standard Temperature and Pressure (STP, 25°C and 1 atm) and 1 cm^3 of this gas contains approximately 2.5×10^{19} CO_2 molecules, whereas 1 cm^3 of SiO_2, a solid at STP, consists 2.7×10^{22} molecules: three orders of magnitude more than CO_2. In order to compare CO_2 and SiO_2 they are converted to molar volumes (cm^3/mol) using $\overline{V}_i = \frac{1}{n_i} V_i$, where n_i is the number of moles of component i and V_i is its volume. At these conditions, the calculated molar volumes are approximately 24,500 cm^3/mol for CO_2, and 22.8 cm^3/mol for SiO_2, which makes sense because CO_2 under these conditions is a gas and 1 mole of a gas has a larger volume than 1 mole of a solid.

Carbon in the Earth

As CO_2 is one of the most abundant volatile species in mantle-derived magma source regions (Anderson, 1975; Canil and Scarfe, 1990), it is vital to understand the effect it has on melt behavior. Carbon dioxide's effect on a melt's density and eruptibility must be quantified in order to fully detail mantle processes. Carbon dioxide is found outgassing from volcanoes and is seen as carbon in the form of graphite and diamonds. Carbon entered the mantle during the accretion of the planet and/or by meteorite impact on the early Earth's magma ocean (i. e. late veneer when volatile-rich bodies impacted the Earth after accretion creating a volatile layer on the Earth's surface

see Kuramoto, 1997; Turekian and Clark, 1975 for discussion), and enters the mantle today by subduction of ocean slabs in minerals such as magnesite and dolomite. The actual amount of CO_2 in the interior of the Earth is unknown, but estimates can be made based on element ratios, volcanic gas measurements, recycling models, and through analysis of mantle rocks (McDonough and Sun, 1995; Taran et al., 1998). Depending on which mantle rock is analyzed (peridotite, basalt, kimberlite, komatiite) estimates of the amount of CO_2 in the primitive mantle range from 230-550 ppm (Wyllie and Ryabchikov, 2000; Zhang and Zindler, 1993), and <50 to >500 ppm carbon in the Earth's upper mantle today (McDonough and Sun, 1995).

The presence of CO_2 in the mantle affects properties such as liquidus and solidus temperatures, melt density, and the behavior of partial melts in the mantle (Bourgue and Richet, 2001; Eggler, 1978; Hirose, 1997; Liu and Lange, 2003; Wendlandt and Mysen, 1980). To explore the behavior of CO_2 at elevated pressures and temperatures, numerous studies have been carried out. Many studies have focused on the solubility of CO_2 in various mantle compositions, measuring the amount of CO_2 dissolved in different partial melt compositions (Dobson et al., 1996; Pan et al., 1991; Stolper and Holloway, 1988; Thibault and Holloway, 1994). The findings from this previous work show that pressure, temperature, and composition have a significant effect on the solubility of CO_2 in silicate melts (Brooker et al., 2001a; Dasgupta and Hirschmann, 2007; Dixon et al., 1995; Eggler and Rosenhauer, 1978; Mysen et al., 1976; Taylor, 1990), with pressure increasing solubility dramatically, temperature decreasing solubility, and melts with non-bridging oxygen (NBO) to tetrahedral network-forming cation (T, e.g. Si^{2+} and Al^{3+}) ratios greater than zero showing the highest CO_2 concentrations.

Carbon dioxide is most soluble in mafic and ultramafic melts because of the increased NBO/T ratios most affected by lower amounts of SiO_2. The silica tetrahedra polymerize the melt creating bridging oxygens. In order for CO_2 to enter a melt there must be non-bridging, or "free", oxygens for the molecule to bond with (Brooker et al., 2001a). This creates the carbonate anion in the melt, the most common form of carbon in mantle melts (Mysen et al., 1976). Studies done on the forms of CO_2 in basaltic melts using Raman spectroscopy and Infrared spectroscopy found that while CO_3^{2-} is most common, molecular CO_2 and CO are also possible in melts with lower NBO/T ratios such as andesite or rhyolite (Brooker et al., 2001a; Dixon and Pan, 1995; Fine and Stolper, 1985; Lange, 1994) These studies determined that the form of carbon in the melt is affected by the availability of non-bridging oxygens. Non-bridging oxygens are created when network modifying cations (e. g. Mg^{2+}, Ca^{2+}) enter the melt and break the bonds of SiO_2 and Al_2O_3 tetrahedra. Those melts with NBO/T < 0.5 will tend to contain dissolved CO_2, while melts with NBO/T > 0.5 are more likely to contain CO_3^{2-}, along an approximately linear relationship. An ultramafic composition, such as komatiite, will dissolve CO_2, as CO_3^{2-}, and is appropriate as an upper mantle analog, and therefore is our choice for this study.

Composition

The upper mantle of the Earth is thought to be roughly peridotitic in composition. Peridotite was first proposed by Bowen (1928) based on mantle seismic velocity and basaltic magma compositions which are thought to be partial melts of peridotite. Since that time, peridotite has been further investigated and found to fit the geochemical and geophysical properties of the mantle (Palme and O'Neill, 2003; Ringwood, 1966). Many

peridotite xenoliths exist on or near the Earth's surface and have been studied thoroughly. Such xenoliths are present in southern New Mexico at Kilbourne Hole. A sample from this site, KLB-1, was studied by Takahashi (1986) because it was thought to represent an undepleted, upper mantle composition and is similar to the pyrolite composition for the mantle proposed by Ringwood (1966).

A simplified version of a partial melt of this peridotite sample – a komatiite, containing only major elements, was used for these experiments because of its standing as a good upper mantle average and its ability to take large (~5 wt%) amounts of dissolved CO_2 into its melt structure. As stated above, CO_2 should dissolve in the melt as CO_3^{2-} due to the ultramafic nature and the NBO/T value of the experimental composition. The NBO/T value for our composition is approximately 0.93 and, as shown in Figure 3 of Brooker et al. (2001a), this NBO/T value indicates that ~6.0 wt% CO_2 can dissolve in the melt at 1.5 GPa for simple, Fe-free compositions. Dixon (1997) modeled CO_2 solubility in Fe-bearing, more Mg-rich compositions and determined a compositional parameter, Π, to describe CO_2 solubility. This parameter is based on melt depolymerization (i. e. the amount of Si^{4+} and Al^{3+} present in the melt) and the potential of cations to react with carbonate (i. e. network modifying cations that form non-bridging oxygens), where $\Pi = -6.50(Si^{4+} + Al^{3+}) + 20.17(Ca^{2+}\ 0.8K^{1+} + 0.7Na^{1+} + 0.4Mg^{2+} + 0.4Fe^{2+})$, with the cations in molar proportions. The Π parameter for our experimental composition is approximately 1.48. This indicates, from Figure 2B of Dixon (1997), that our melt will dissolve ~4.0 wt% CO_2 at 2.0 GPa. Due the pressure affect on CO_2 solubility, our experiments done at pressures above 3.5 GPa, should easily dissolve ≥ 5.0 wt% CO_2.

Previous Studies

Earlier studies indicated that dissolved CO_2 should have a large effect on silicate liquid density (Bourgue and Richet, 2001; Dasgupta et al., 2007), however there are few experimental data at high pressure on possible mantle compositions. Here we contribute to this database by determining the densities of carbonated komatiite melt and the same melt with no CO_2 at high pressure. Using these data, we were able to derive the partial molar volume of CO_2 ($\overline{V}_{CO_2}$) by difference in the silicate melt as a function of pressure using a modified version of Equation (1-1). Our results bridge the large gap between 1 bar and 19.5 GPa, where $\overline{V}_{CO_2}$ has been measured.

Previous studies have determined the partial molar volumes of other liquid oxides (e.g. CaO, MgO, H_2O) in order to better determine the origin and behavior of magmatic systems (Agee, 2008a; Lange and Carmichael, 1987). Using a Equation (1-1) and the molar volumes of melt components, the density of the melt can be determined using thermal expansivity ($\partial V_i/\partial T$) values at a given temperature. By knowing the density and composition of carbonated and non-carbonated silicate melts of similar major element abundance, the difference between the melt molar volumes will be $\overline{V}_{CO_2}$. Determining $\overline{V}_{CO_2}$ values at various pressures will lead to the derivation of a compression curve, which describes how $\overline{V}_{CO_2}$ changes with pressure. This curve can then be used to explain the behavior of carbonated silicate melts in the upper mantle.

Studies done on carbonated compositions that measured the density of the melt can be used to estimate $\overline{V}_{CO_2}$ for those compositions (Table 1-1). Since most of these studies were done with carbonate compositions rather than silicate, it may not be appropriate to apply the $\overline{V}_{CO_2}$ values determined to carbonated silicates, such as in the

mantle. Also, many of these experiments were performed at 1 bar, and cannot be used to constrain the $\overline{V}_{CO_2}$ compression curve at high pressure.

Table 1-1. Calculated partial molar volumes of CO_2 from previous carbonate and carbonated silicate studies.

Composition	$\overline{V}_{CO_2}$ (cm^3/mol)	*P* (GPa)	*T* (°C)	Reference
$CaCO_3$	25.81	1.0×10^{-4}	827	Liu and Lange (2003)
Na_2CO_3	28.73	1.0×10^{-4}	827	Liu and Lange (2003)
K_2CO_3	32.35	1.0×10^{-4}	827	Liu and Lange (2003)
$CaCO_3$	33.36	0.1	1364	Genge et al. (1995)
$K_2Ca(CO_3)_2$	35.20	1.0×10^{-4}	1677	Dobson et al. (1996)
$K_2Ca(CO_3)_2$	31.76	2.5	1677	Dobson et al. (1996)
$K_2Ca(CO_3)_2$	29.92	4.0	1677	Dobson et al. (1996)
Tholeiite	23.14	0.1	1200	Pan et al. (1991)
MORB	33.00	0.1	1200	Stolper and Holloway (1988)
Ca-rich Leucitite	22.03	0.1	1200	Thibault and Holloway (1994)
Alkaline silicate melts	19.90	2.0	1400	Liu and Lange (2003)
Carbonated MORB	20.98	19.5	2300	Ghosh et al. (2007)

A preliminary compression curve for $\overline{V}_{CO_2}$ was determined by Ghosh et al. (2007). They used sink/float experiments at 19 and 20 GPa with a diamond buoyancy marker and determined the $\overline{V}_{CO_2}$ for a mid-ocean ridge basalt (MORB) to be 20.98 cm^3/mol at 19.5 GPa and 2300°C. In order to calculate an equation of state for $\overline{V}_{CO_2}$, Ghosh et al. (2007) calculated 1 bar, 2.5 GPa, and 4.0 GPa $\overline{V}_{CO_2}$ values from the carbonate liquid density studies of Genge et al. (1995) and Dobson et al. (1996), correcting for temperature using $\partial V_{CO2}/\partial T = 4.0 \times 10^{-3}$ cm^3/mol-K (Liu and Lange, 2003) (Table 1-1). They then derived values for the isothermal bulk modulus ($K_T = 3.7$ GPa) and its pressure derivative ($K' = 9.0$) from the Vinet equation of state (EOS).

Since the effect of composition on $\overline{V}_{CO_2}$ is thought to be negligible only for silicate melts in the range of 40 to 80 mol% SiO_2 (Bockris et al., 1956; Bottinga and Weill, 1970; Shartsis et al., 1952; Tomlinson et al., 1958), carbonate melt compositions

with no SiO_2 may not accurately describe $\overline{V}_{CO_2}$ for silicate melts. Because the presence of SiO_2 in a melt will alter melt structure from that of a carbonate melt, it follows that the 1 bar, 2.5 GPa, and 4.0 GPa $\overline{V}_{CO_2}$ values, which were calculated from carbonate compositions and not silicate, may not be accurate to apply to Si-bearing mantle analogs. Our experiments on carbonated silicate melt now fill in the gap between 1 bar and 19.5 GPa thus removing the need to rely on non-silicate-bearing melt high pressure data. With an updated $\overline{V}_{CO_2}$ compression curve, based on carbonated silicate melts, the densities of these melts can be defined more accurately at upper mantle pressures. These densities are important to know so that the physical properties and behaviors of carbonated silicate melts, e.g. kimberlite buoyancy and eruption, can be described more accurately.

Chapter 2

Experimental Procedures

A simplified komatiite starting composition was chosen for the experimental runs based on the composition of Dasgupta et al. (2007) (Table 2-1). This composition (PERC) was a carbonated partial melt derived from peridotite KLB-1. The KLB-1 sample is a good representation of an undepleted, average upper mantle (Takahashi, 1986), and therefore a good analog to determine $\overline{V}_{CO_2}$ in a carbonated silicate melt. The simplified composition was used to ensure there was no compositional control on $\overline{V}_{CO_2}$, which may be influenced by the form of carbonate present in the melt ($CaCO_3$ rather than K_2CO_3, Na_2CO_3: Liu and Lange, 2003). Two komatiite mixes were made with the same major element abundances using reagent grade powdered oxides. One mix, DG-5, contained $CaCO_3$ which translates to approximately 5.7 wt% CO_2 (Table 2-1). This amount is more than is found in partial melts derived from peridotite compositions (~90-134 ppm in the MORB source region: Shaw et al., 2010), but was chosen because it should be detected easily by analytical methods. The other mix, DG-N, only contained CaO so that a non-carbonated baseline density could be determined, which allows for a more accurate calculation of $\overline{V}_{CO_2}$.

Table 2-1. Composition of peridotite KLB-1, its carbonated experimental partial melt (PERC) at 3 GPa, and our simplified starting compositions based on PERC + 5 wt% CO_2.

Oxide (wt%)	KLB-1 Takahashi (1986)	PERC Dasgupta et al. (2007)	Starting Material DG-5	Starting Material DG-N
SiO_2	44.48	43.19	43.36	46.69
TiO_2	0.16	0.47		
Al_2O_3	3.59	7.27	6.97	7.30
Cr_2O_3	0.31	0.33		
FeO	8.10	9.64	10.02	10.60
MnO	0.12	0.20		
MgO	39.22	25.92	26.63	28.29
CaO	3.44	7.30	7.29	7.13
Na_2O	0.30	0.57		
K_2O	0.02	0.04		
NiO	0.25			
CO_2		5.09	5.72	
Total	99.99	100.00	100.0	100.00
NBO/T	n/a	0.93		n/a
Π	n/a	1.48		n/a
Mg#	89.62	82.62	82.58	82.64

The sink/float experimental method (Agee and Walker, 1988, 1993) was used in order to determine the density of the melt in each experiment. This was accomplished by loading the powdered starting composition into molybdenum (Mo) capsules along with two mineral spheres. Molybdenum capsules were used because of the oxygen fugacity (f_{O2} ~1+ Iron-Wustite oxygen buffer) they impart on the charge and for the lack of influence that dissolved Mo has on the melt structure (Agee and Walker, 1988). The capsule, lid, and both mineral spheres were cleaned with ethanol in a sonicator for 50 seconds and allowed to dry before use to ensure no contamination of the experimental melt composition. Approximately 10 mg of the powered mix was loaded into the capsule with spheres; the capsule contents were layered: mix-sphere-mix-sphere-mix, so that there was no contact between the spheres and capsule walls to which the spheres could adhere during the run which would restrict their movement. This layering was also done

to ensure that one sphere was near the bottom of the capsule, while the other was near the top, to allow for enough space for their movement and making any movement easier to determine after the run.

Mineral spheres of known density were used to calculate the density of the experimental melt, which in turn allowed for the calculation of $\overline{V}_{CO_2}$. These mineral spheres, or density markers, have well defined density/pressure (compressibility) curves with constant temperature. Starting with forsterite 100 (Fo100), which was the lowest density mineral used, the compressibility curves of the two melts was constrained at low pressure (~4 GPa). San Carlos olivine, approximately forsterite 90 (Fo90), was used to constrain the compressibility curves of the silicate melts at increasingly higher pressures (between 4 and 6 GPa) to begin to fill in the gap between 1 bar and 19.5 GPa. Melt density was determined by relative sphere placement at the end of the run. If the mineral spheres were denser than the experimental melt, they sank, while if they were less dense they were located at the top of the capsule at the end of the run. The ideal pressure and temperature conditions need to be reached where the spheres and melt have the same density – a neutral buoyancy – where the relative sphere positions remain unchanged from their initial placement.

A brief note on olivine sphere size – mineral spheres were made using the Bond air mill technique which uses air pressure to push mineral fragments around a chamber that is lined with carbide paper thereby grinding them into "spheres" (Bond, 1951). Ideal size is between 400 and 650 microns determined from these experiments. We found that spheres bigger than ~700 μm do not have enough space to move in the capsule and yield false neutral buoyancy results. We also found that spheres smaller than ~350 μm melted

completely during the experiment and consequently their relative positions could not be determined.

Experiments were run in a Walker style multi-anvil press at the University of New Mexico using 8 mm truncated edge length (TEL) WC cubes, suitable for experimental run pressures of this study. Once the capsule was loaded and capped with a friction fit Mo lid, it was placed in a 14 mm octahedral edge length ceramic octahedron with crushable alumina spacers above and below it to keep the capsule centered in the heater next to the W26%Re and W5%Re thermocouple connection, and a hard-fired alumina sleeve around the capsule to ensure no contact with the rhenium heater (Figure A-1). The octahedron was then surrounded by the WC cubes connected by circuit boards to ensure no contact with the metal anvils of the pressure vessel.

The charge was then pressurized to the appropriate value for the run and held there while temperature was applied using a Eurotherm 3504 temperature controller. The temperature was set above the liquidus of the experimental composition to ensure complete melting, and the ramp rate was fast, approximately 350°C/minute in order to keep the mineral spheres from melting. Once the target temperature was reached, the experiment was held at pressure and temperature for 20-60 seconds. This is enough time to ensure melting without the formation of equilibrium crystals which would affect sphere movement (Agee and Walker, 1993). After time elapsed, the experiment was quenched by turning off the temperature controller. Once the experiment depressurized, the capsule was removed from the press and octahedron, mounted in epoxy and allowed to set overnight.

Once set, the experimental charge was ground into to expose the inside of the capsule. This allows for confirmation of melting by the presence of quench crystals visible under the optical microscope, and the determination of relative sphere position (Figure 2-1).

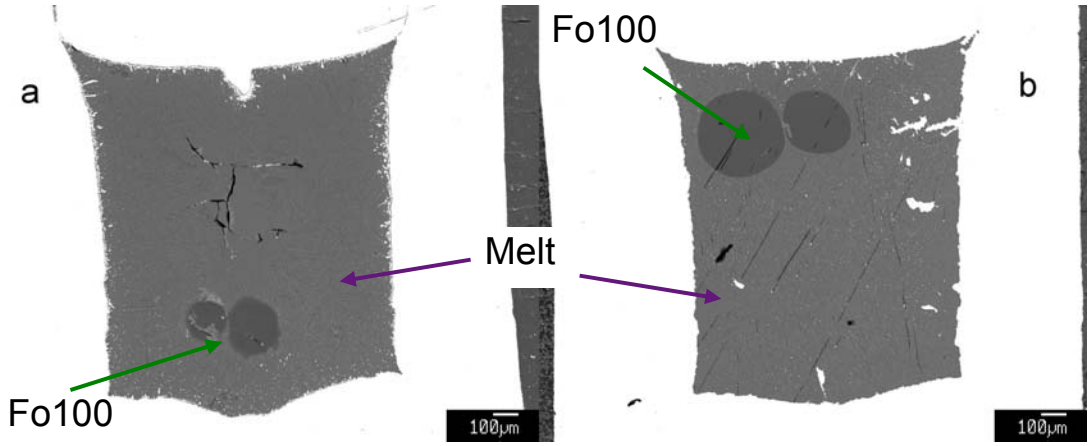

Figure 2-1. BSE images of experimental run products with Fo100 spheres. a) Sink DG-5-9, b) Float DG-N-7

For each melt composition and each mineral density marker, a neutral buoyancy, sink and float are required to ensure the accuracy of the density measurement. The exception is when the sink and float are within a few tenths of a GPa of each other in which case a neutral buoyancy is not required. From the neutral buoyancy result, the density of the melt can be calculated using the density of the mineral spheres. The density of the melt at neutral buoyancy run conditions was calculated using elastic properties for the mineral spheres (Table 2-2), assuming linear mixing of the olivine endmembers, and the third order Birch-Murnaghan EOS:

$$P = \frac{3}{2} K_T \left[\left(\frac{\rho}{\rho_0} \right)^{\frac{7}{3}} - \left(\frac{\rho}{\rho_0} \right)^{\frac{5}{3}} \right] \left\{ 1 - \frac{3}{4}(4 - K') \left[\left(\frac{\rho}{\rho_0} \right)^{\frac{2}{3}} - 1 \right] \right\} \quad \textbf{(2-1)}$$

where P is pressure in GPa, K_T is the isothermal bulk modulus of the mineral spheres, K' is its pressure derivative, ρ is the density of the spheres at experimental pressure, and ρ_0 is the zero pressure density at the experimental temperature, which can be written as:

$$\rho_{T,0} = \rho_{298}(T) \exp \int_{298}^{T} \alpha(T) dT \quad \textbf{(2-2)}$$

in which the thermal expansion α is defined as:

$$\alpha(T) = \alpha_0 + \alpha_1 T + \alpha_2 T^{-2} \quad \textbf{(2-3)}$$

Table 2-2. Elastic parameters for endmember olivines used to calculate density with the 3rd order Birch-Murnaghan EOS.

Mineral	K_T (GPa)	K'	dK/dT	α_0 (x10^{-5})	α_1 (x10^{-9})	α_2	V_0 (cm^3/mol)
Forsterite	127.5[a]	4.8[a]	-0.02[b]	3.034	7.422	-0.5381[c]	43.68[d]
Fayalite	134.6[e]	5.2[f]	-0.024[e]	2.386	11.53	-0.0518[g,h,i]	46.22[i]

[a] (Jacobs and de Jong, 2007), [b] (Liu and Li, 2006), [c] (Suzuki, 1975), [d] (Hushur et al., 2009), [e] (Graham et al., 1988), [f] (Isaak et al., 1993), [g] (Suzuki et al., 1981), [h] (Smyth, 1975), [i] (Hazen, 1977)

Once sphere position was determined using the optical microscope, the run products were analyzed using the JEOL JXA-8200 electron microprobe and Fourier Transform micro-Infrared Spectroscopy (FTIR). This was done to ensure CO_2 was retained during the run, and acted as a check on the melt composition. (See Chapter 3 and Appendices B and C for complete discussion on analytical techniques.)

After melt density was calculated and composition was confirmed with the microprobe, the partial molar volume of CO_2 ($\overline{V}_{CO_2}$) of the carbonated melt was determined at the pressure and temperature of the experimental run using a modified version of the equation of Bottinga and Weill (1970) (see Appendix A for conversion steps):

$$\overline{V}_{CO_2}^{P,T} = \left\{ \left(\sum_i M_i X_i \Big/ \rho_{CO_2}^{P,T} \right) - \left[\left(\sum_i M_i X_i - M_{CO_2} X_{CO_2} \right) \Big/ \rho_N^{P,T} \right] \right\} \Big/ X_{CO_2} \qquad \textbf{(2-4)}$$

where X_{CO2} is the mole fraction of CO_2 in the melt, M_{CO2} is the molar mass of CO_2, $\rho_{CO_2}^{P,T}$ is the density of the carbonated melt (DG-5) at the neutral buoyancy pressure and temperature, $\rho_N^{P,T}$ is the density of the non-carbonated melt (DG-N) at neutral buoyancy pressure and temperature. The $\overline{V}_{CO_2}$ was calculated at every neutral buoyancy pressure and at 1850°C to create the compression curve from 1 bar to 19.5 GPa, using our data combined with literature data.

Chapter 3

Analytical Techniques

The run products were analyzed with the electron microprobe (EMPA) for major elements to verify consistency with starting composition and to quantify Mo ingress. In previous studies (Dalton and Presnall, 1998; Ghosh et al., 2007) the CO_2 content of quenched melt run products were determined by difference from 100% electron microprobe totals. Although this method has been widely used previously, it is not an ideal way to determine volatile content, so in this study we attempted to determine bulk carbon content using a JEOL JXA 8200 electron microprobe with silver or gold coatings on the sample and standard surfaces. Overall, our analyses for carbon were broadly consistent with the starting CO_2 content, as well as the CO_2 content estimated by difference from 100% totals, confirming that CO_2 loss during the experiments was negligible or minor.

We also attempted to analyze the run products using Fourier Transform micro-Infrared Spectroscopy (FTIR) in reflectance and transmission modes, which detects carbon-bearing species such as CO, CO_2 and CO_3^{2-}. While this technique is proven for homogeneous glasses, it was not successful for our run products because they contained heterogeneous quench crystals distributed with glass domains. An added complication is tiny, highly reflective Mo blebs dispersed in our quenched melts that may induce scatter or interference of the FTIR beam, masking the C-O signal. Future work may improve this technique by employing high spatial resolution IR spectral maps which would aid in characterizing small heterogeneous samples from high pressure solid media devices.

We note that earlier work by Dixon (1997) predicts that our melt composition should readily take 5.7 wt% CO_2 (most likely as CO_3^{2-}: Mysen et al., 1976) into solution at the high pressures of our experiments (see Chapter 1-Composition). Supporting evidence for complete solubility of CO_2 comes from lack of bubbles or supercritical fluid phases in our run products. To test this we ran some experiments with 5.7 wt% CO_2 at low pressure (1 GPa) and observed fluid phase bubbles in our quench melt, consistent with the expectation of lower CO_2 solubility at modest pressures.

Electron Microprobe

The convention for determining the amount of CO_2 in carbonated samples with the electron microprobe is to calculate it by difference. In this procedure, a sample is analyzed for all oxides except CO_2 and it is assumed that the deficit from a total of 100% is due to CO_2. Carbon is usually analyzed directly by some other means (e. g. FTIR, Raman spectroscopy) thereby confirming that the microprobe deficit is due to CO_2. This method has been used repeatedly with some success, but is not ideal. However, the samples analyzed are typically natural or experimentally quenched glasses. In these experiments the quench product is quench crystals containing small areas of glass, not a clear glass, which is typical for ultramafic compositions. Because the quench crystals cause the sample to be extremely heterogeneous, and can become large (~10-50 μm wide and a few 100 μm long) creating abrupt grain boundaries that a glass does not have, microprobe analysis is difficult. Nevertheless, we tried to detect carbon directly with the microprobe.

Clearly when analyzing for carbon in the electron microprobe, the samples cannot be carbon-coated. We began by using a silver-coat (Ag-coat) which we applied to the

experiments and standards (McGuire et al., 1992). The first set of standards were SiC for C; olivine for Si, Mg, and O; and andradite for Fe, Al, and Ca. The standard for Mo was the capsule of an experiment, because there was no readily accessible Ag-coated Mo standard. We began with an accelerating voltage of 15 kV, a current of 2.5×10^{-8} A, and a beam diameter of 20 µm, which are ideal operating conditions to analyze silicate glasses. All analyses were done using the Wavelength Dispersive Spectrometer (WDS) on a metal basis using φρz correction and a LDE2 crystal to detect carbon. There was some difficulty accurately detecting carbon – it was present in non-carbonated samples in similar amounts as those found in the carbonated samples (Figure 3-1).

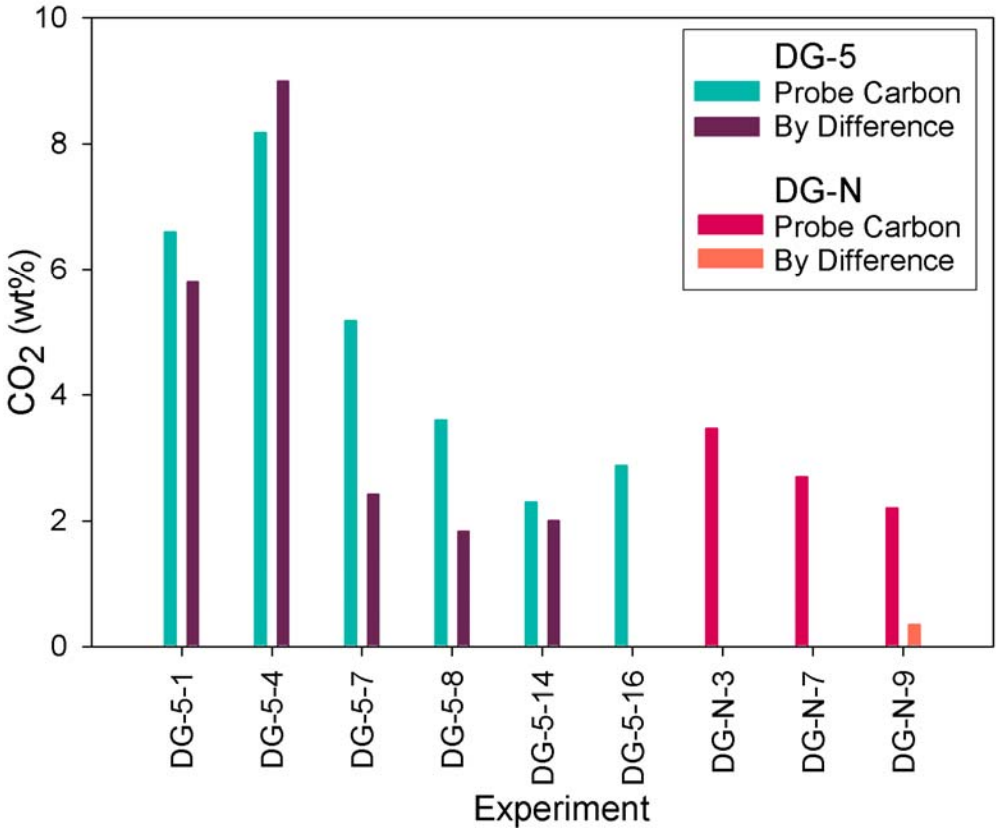

Figure 3-1. EPMA for CO_2 of Ag-coated experiments. The amount of CO_2 was calculated two ways: 1. Based on the amount of C detected by the microprobe (Probe Carbon), 2. Based on the by difference method described above (By Difference). The carbonated experiments (DG-5) Probe Carbon amounts are turquoise, and the By Difference are purple. The non-carbonated experiments (DG-N) Probe Carbon amounts are red, and the By Difference are orange. On average, the amount of CO_2 determined from Probe Carbon is the same for the DG-5 and DG-N experiments.

We then tried using a gold-coat (Au-coat) along with different carbon standards and different operating conditions to see if we could reduce the background amount of carbon (the carbon detected in non-carbonated samples) which could then be subtracted from the carbon amount detected in the carbonated samples. See Table B-1 for all Ag-coated operating conditions and the experiments analyzed, Appendix B for our other attempts at detecting carbon directly, and Tables B-3 through B-10 and B-12 through B-14 for the analytical results.

We have not yet definitively detected carbon accurately with the electron microprobe. For these particular samples – which contain heterogeneous quench crystals – it seems that there is no difference between the Ag- and Au-coats when analyzing for carbon, although the Ag-coat seems to work better for oxygen detection. For the Au-coated samples, for which there is more variation in analytical operating conditions, it appears that a spot size of 50 μm gives a better average over the sample, along with a lower accelerating voltage 10-12 kV and an increased current of 4.0×10^{-8} to 8.0×10^{-8} A. Dasgupta and Walker (2008) used the electron microprobe to analyze for carbon in Fe-Ni-carbides and found that a reduced peak counting time reduced the background carbon detected (10 second peak measuring time, 5 second background measuring time). We have not been able to replicate these results most likely due to the state of carbon in our samples: carbonate rather than carbide. The limited success we had with the Ag-coats and conditions needs to be reproduced and more conditions need to be tested to try and reduced the carbon background.

Fourier Transform Infrared Spectroscopy

Due to the ambiguity in the electron microprobe analyses and the different analytical conditions of FTIR, we also tried FTIR in our quest to detect carbon in our samples. This method is much more accurate than EMPA when analyzing for light elements such as carbon, oxygen and hydrogen, but will also detect silicon, aluminum and iron. FTIR has been used on many natural and experimental carbonated glasses with success. We therefore utilized this method to analyze our carbonated quenched melts.

Carbon can take many forms in magma; the most common form is the carbonate anion (Mysen et al., 1976) though CO_2 and CO are also possible (Brooker et al., 2001b; Dixon and Pan, 1995; Fine and Stolper, 1985; Lange, 1994). The form that carbon should take in these experimental melts should be CO_3^{2-} due to the ultramafic composition (see Chapter 1-Composition). The carbonate anion's $\nu 3$ antisymmetric stretch usually appears as a doublet in IR spectra located approximately at 1550 and 1420 cm^{-1}. The exact location, shape, and size of this doublet depend on the state of the anion in the melt. The typical splitting of the doublet, the distance between the peaks measured as $\Delta\nu 3$, in silicate melts is between 70 and 100 cm^{-1} (Brooker et al., 2001b; Fine and Stolper, 1986; King and Holloway, 2002). This splitting largely depends on the distortion of CO_3^{2-}. With more depolymerized silicate melts such as the one in this study, the distortion is less and $\Delta\nu 3$ becomes smaller. This may be due to the presence of Ca^{2+} which depolymerizes the melt and bonds with CO_3^{2-}, in which case there should be a peak around ~1461 cm^{-1} with $\Delta\nu 3 \leq 80$ cm^{-1} in our samples (Brooker et al., 2001b). Although for "poorly quenched" samples, i. e. samples that are not glasses such as our experiments, a single peak ($\Delta\nu 3 = 0$ cm^{-1}) may exist at ~1440 cm^{-1}.

We used micro-FTIR in reflectance mode to analyze the experiments with a KBr beamsplitter. The metal coating necessary for the electron microprobe analyses was removed and the samples were cleaned with acetone before being placed under the FTIR microscope. In order to have the microscope in focus while still keeping a seal around the sample to minimize the background, the epoxy mounts had to be cut down significantly with a diamond saw to ≤ 3 mm thick. Spectra were collected either before or after a background was collected on an Au plate, which was necessary in order to subtract out any atmospheric signal in the sealed chamber under the microscope. The resultant reflectance spectra that were collected were smoothed using either a 21 or 11 point window, depending on the resolution, and converted into absorbance spectra using Kramers-Kroning conversion. Absorbance spectra are quantitative, so from the intensity of the peaks the amount of carbonate in the quenched melt can be calculated. Unfortunately, we were not able to detect carbon in any form in our samples, see Appendix C for full details.

There are several possibilities that may preclude our ability to find the carbonate. The potential of a Si overtone is unlikely because the peak we detected in some carbonated and non-carbonated experiments at ~1420 cm^{-1}, disappeared in the smoother samples. If the peak had been caused by the presence of Si, it would have been present in all spectra because each experiment contained the same amount of Si. If the carbon is not in an oxidized form, perhaps as a carbide instead of CO_3^{2-}, FTIR would not detect it. Because the Mo capsules impart an f_{O2} approximately one log unit above IW, the carbon should be in an oxidized form at the pressures and temperatures of the experiments. The carbon could be leaking out of the capsule after the experiment is run – during

depressurization – as the capsule is not sealed. An experiment was run to be tested on a sealed gas line where any carbon present could be frozen out and measured (DG-5-20). The most likely problem is the presence of small Mo blebs in the melt from the capsule. These metal blebs reflect the IR beam randomly, scattering it so that any carbonate signal that is present does not reach the detector. Although it would be ideal to re-run the experiments in sealed Pt capsules, this is beyond the scope of this project.

Experimental CO_2

Because we could not accurately detect the amount of CO_2 in our experiments with either the microprobe or FTIR, we began to wonder if it was even there, and if so how much. To be sure that the carbon was actually present during the runs, we ran an experiment at low pressure where a vapor phase should be present (DG-5-17, see discussion in Chapter 1-Composition for details). To know the low pressure accurately for this experiment, a Depths of the Earth quickpress was used. The DG-5 mix was placed in a Mo capsule without spheres so that any bubbles present would be obvious. The experiment was held at 1 GPa and ~1780°C for 30 seconds and then quenched isobarically. During the grinding process, using kerosene and alcohol, the sample was checked at short intervals using an optical microscope and bubbles were visible throughout the melt, as well as a high amount of Mo, confirming that CO_2 was present during the run.

We are in the process of synthesizing better carbon standards using the same reagent grade starting powders used in this study to create carbonated silicate glasses (nephelinite and basalt) by melting and quenching them at low pressure in the piston cylinder. Once completed, these compositions should give better standard calibrations

for carbon in a silicate composition, compared to the carbon in carbonates that were used for this project.

The microprobe values used to calculate $\overline{V}_{CO_2}$ were collected using Ag-coated experiments with an accelerating voltage of 15 kV, a current of 2.5×10^{-8} A, and a beam diameter of 20 μm (Table 4-4). These data were used because the oxide totals were much closer to 100% than those of the Au-coated samples. Between 20 and 30 analyses were taken for each experiment, and their results averaged to get a bulk composition. Unfortunately, there is still error when the samples are analyzed, and therefore the composition used to calculate $\overline{V}_{CO_2}$ is ideal.

Chapter 4

Experimental Results

The densities of carbonated silicate melt (DG-5, Table 4-1) and non-carbonated silicate melt (DG-N, Table 4-2) of the same major element composition were bracketed by observing the sinking and floating of gem quality olivines Fo100 and Fo90 at high pressure (Figure 2-1). Detailed run conditions for all successful DG-5 and DG-N experiments are presented in Appendix A.

A zero pressure density was calculated for each melt (DG-5 ρ_0 = 2.59 g/cm^3, DG-N ρ_0 = 2.75 g/cm^3) using molar volumes for the liquid oxides determined by Lange and Carmichael (1987; Lange and Carmichael, 1990) and combined with our neutral buoyancy densities at high pressure to derive elastic constants (K_T and K') for DG-5 and DG-N Birch-Murnaghan compression curves at 1850°C. The densities were corrected to 1850°C using $\partial\rho/\partial T_{\text{DG-5}}$ = -2.10 x 10^{-4} g/cm^3°C, and $\partial\rho/\partial T_{\text{DG-N}}$ = -2.11 x 10^{-4} g/cm^3°C. The DG-5 densities used to calculate the compression curve were the neutral buoyancies at 4.7±0.1 GPa (3.14±0.05 g/cm^3) and 5.9±0.1 GPa (3.31±0.05 g/cm^3). The best fit Birch-Murnaghan elastic constants were K_T = 17.22±0.01 GPa and K' = 3.1. The DG-N densities used were the neutral buoyancies at 4.0±0.1 GPa (3.12±0.05 g/cm^3) and 5.1±0.1 GPa (3.28±0.05 g/cm^3). The best fit Birch-Murnaghan elastic constants were K_T = 22.89±0.01 GPa and K' = 3.1 (Figure 4-1, Table 4-3). These values are exact, three-point solutions of the Birch-Murnaghan EOS, however given the small number of pressure-density data points for each melt, a wide array of possible combinations of K_T and K' are also allowable, see Chapter 5.

Table 4-1. Carbonated experimental run conditions and results, where ρ is the density of the melt from the mineral sphere density and ρ_{1850} is that density corrected to 1850°C. The experiments with * are those used for compression curve calculation.

Experiment	Pressure (GPa)	Temp (°C)	Time (sec)	Spheres	Position	ρ (g/cm^3)	ρ_{1850} (g/cm^3)
DG-5-19	4.1	1800	30	Fo 100	Sink	< 3.13	< 3.12
DG-5-9	4.3	1800	30	Fo 100	Sink	< 3.14	< 3.13
DG-5-7	4.6	1805	30	Fo 100	NB	3.15	3.14
DG-5-21*	4.7	1800	30	Fo 100	NB	3.15	3.14
DG-5-1	4.7	1815	25	Fo 100	NB	3.15	3.14
DG-5-4	4.8	1825	30	Fo 100	Float	> 3.15	> 3.14
DG-5-18	4.8	1850	30	Fo 100	Float	> 3.15	> 3.15
DG-5-11	5.6	1850	30	Fo 90	Sink	< 3.29	< 3.29
DG-5-23	5.7	1950	45	Fo 90	NB	3.27	3.29
DG-5-22*	5.9	1950	35	Fo 90	NB	3.29	3.31
DG-5-14	6.1	1950	30	Fo 90	NB	3.29	3.31
DG-5-16	6.3	1950	30	Fo 90	Float	> 3.29	> 3.31

Table 4-2. Non-carbonated experimental run conditions and results, where ρ is the density of the melt from the mineral sphere density and ρ_{1850} is that density corrected to 1850°. The experiments with * are those used for compression curve calculation.

Experiment	Pressure (GPa)	Temp (°C)	Time (sec)	Spheres	Position	ρ (g/cm^3)	ρ_{1850} (g/cm^3)
DG-N-20	3.9	1850	30	Fo 100	Sink	< 3.12	< 3.12
DG-N-3	3.9	1850	30	Fo 100	Sink	< 3.12	< 3.12
DG-N-23	4.1	1850	30	Fo 100	NB	3.13	3.13
DG-N-7	4.1	1850	30	Fo 100	Float	> 3.13	> 3.13
DG-N-26	4.3	1850	45	Fo 100	Float	> 3.13	> 3.13
DG-N-22	4.5	1925	45	Fo 90	Sink	< 3.24	< 3.26
DG-N-17	4.8	1925	30	Fo 90	NB	3.25	3.26
DG-N-14*	5.1	1925	30	Fo 90	NB	3.27	3.28
DG-N-33	5.4	1975	23	Fo 90	NB	3.26	3.29
DG-N-13	5.6	1925	30	Fo 90	Float	> 3.27	> 3.29
DG-N-32	5.7	1975	45	Fo 90	Float	> 3.27	> 3.30

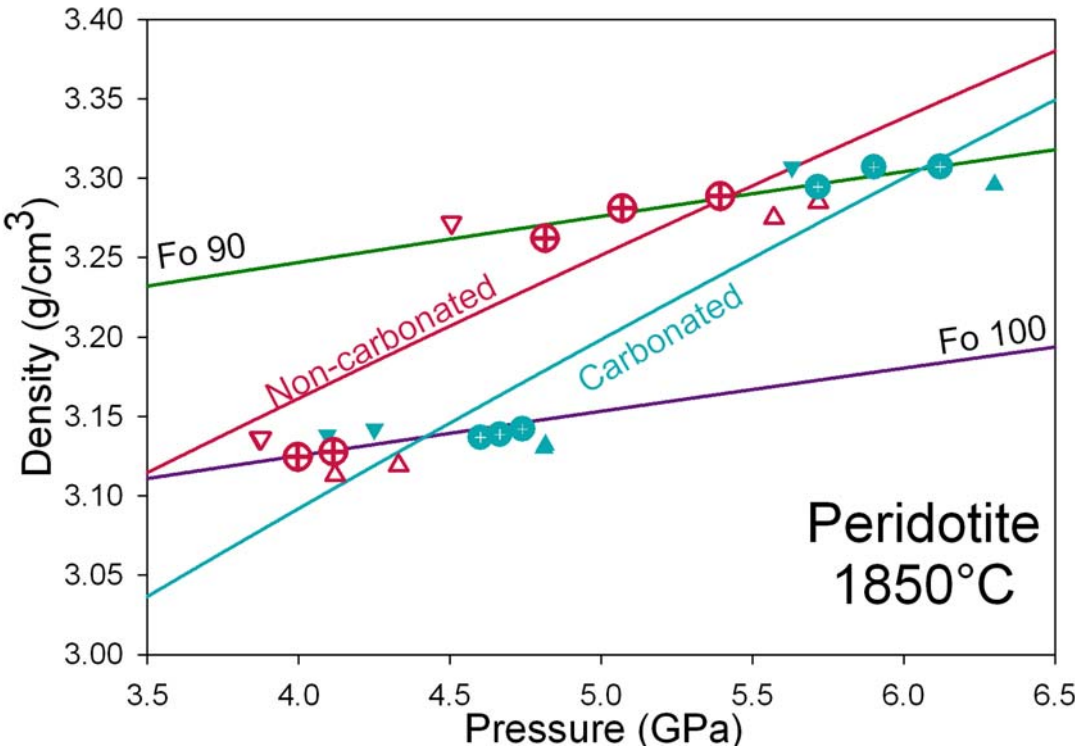

Figure 4-1. Experimental results: up arrow = float, down arrow = sink, circle = neutral buoyancy, turquoise symbols = DG-5 experiments and best fit Birch-Murnaghan compression curve: K_T = 17.22 GPa, K' = 3.1, ρ_0 = 2.59 g/cm^3; red symbols = DG-N experiments and best fit Birch-Murnaghan compression curve: K_T = 22.89 GPa, K' = 3.1, ρ_0 = 2.75 g/cm^3, note the "neutral buoyancy" of the DG-N experiments at 4.0 GPa is not from an experiment, but the midpoint between the sink at 3.9 GPa and the float at 4.1 GPa. Compression curves for the olivine density markers (Fo100 and Fo90) were determined at 1850°C.

As shown in Figure 4-1, the carbonated compression curve fits the experimental data well, but the DG-N (non-carbonated) curve does not. In order to see if the fit could be improved, we adjusted the ρ_0 value of the DG-N curve until it passed through the experimental data (ρ_0 = 2.46 g/cm^3). The DG-5 ρ_0 was then adjusted by the same amount (ρ_0 = 2.32 g/cm^3) and new compression curves were determined. The best fit elastic constants then became K_T = 11.60±0.01 GPa and K' = 3.1 for the DG-N melt, and K_T = 9.95±0.01 GPa and K' = 3.1 for the DG-5 melt (Figure 4-2). Even though the new compression curves are good fits for both melts, a value of ρ_0 = 2.46 g/cm^3 for a non-carbonated komatiite is comparatively too low when compared to calculated values of

peridotites and komatiites (ρ_0 = 2.65-2.85 g/cm^3, e.g. Agee and Walker, 1988; Suzuki and Ohtani, 2003), which may indicate that forcing the fit this way is not a valid treatment.

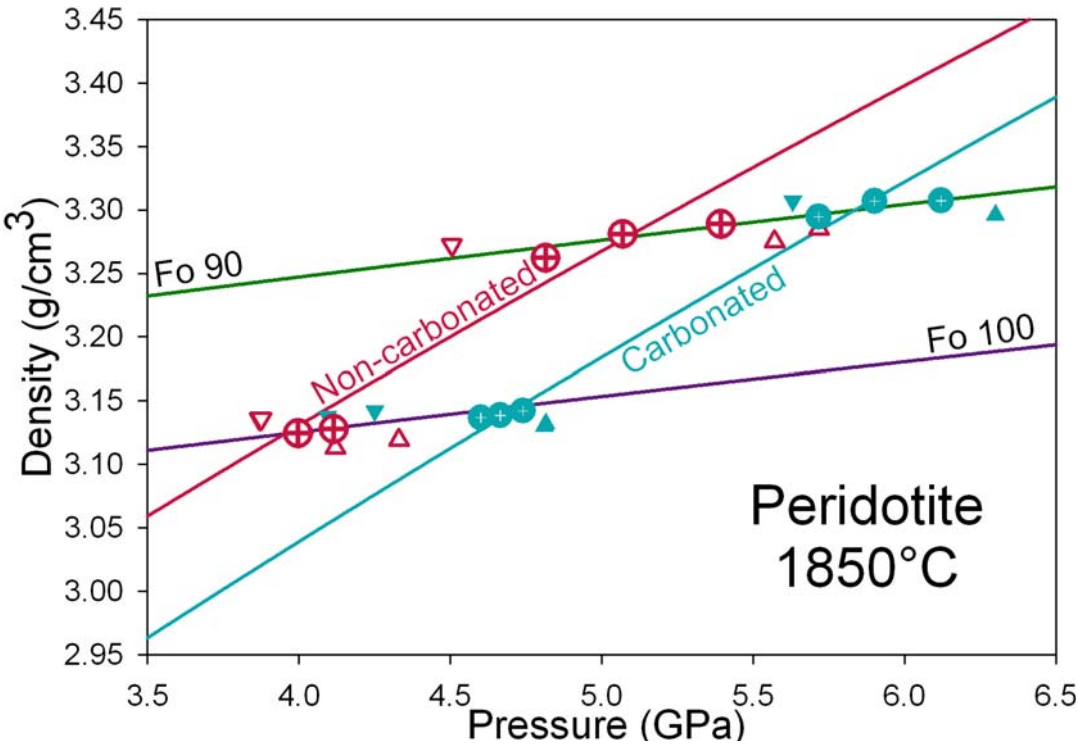

Figure 4-2. Experimental results: up arrow = float, down arrow = sink, circle= neutral buoyancy, turquoise symbols = DG-5 experiments and best fit Birch-Murnaghan compression curve: K_T = 9.95 GPa, K' = 3.1, ρ_0 = 2.32 g/cm^3; red symbols = DG-N experiments and best fit Birch-Murnaghan compression curve: K_T = 11.60 GPa, K' = 3.1, ρ_0 = 2.46 g/cm^3, note the "neutral buoyancy" of the DG-N experiments at 4.0 GPa is not from an experiment, but the midpoint between the sink at 3.9 GPa and the float at 4.1 GPa. Compression curves for the olivine density markers (Fo100 and Fo90) were determined at 1850°C.

The densities used to create the compression curves were not corrected for slight differences in the melt composition of each experiment, mostly resulting from the amount of Mo dissolved in the melt. The presence of Mo, dissolved in the melt mostly as MoO_3, will change the density of the melt. Based on the average of the variation in melt composition, more accurate values of ρ_0 for the DG-5 and DG-N melts are 2.57 g/cm^3 and 2.73 g/cm^3 respectively, similar to those densities used in the above calculations. This may indicate that the K_T and K' determined for the poorly fitting curves (Figure 4-1, Table 4-3) are most accurate in describing the melt behavior of these experiments.

Table 4-3. Best fit Birch-Murnaghan EOS parameters used for $\overline{V}_{CO_2}$ calculation and their R^2 values.

	DG-5	DG-N
ρ_0 (g/cm^3)	2.59	2.75
K_T (GPa)	17.22	22.89
K'	3.10	3.10
R^2	0.9957	0.9842

The most important result from the experiments is the density difference ($\Delta\rho$) between the two melts at their neutral buoyancies at each olivine compression curve crossover: $\Delta\rho$ = 0.025 (Fo100) and 0.021 (Fo90), which are much smaller than the zero pressure $\Delta\rho$ of 0.143. The calculated density difference between the carbonated and non-carbonated silicate melts allowed calculation of $\overline{V}_{CO_2}$ using Equation (2-4):

$$\overline{V}_{CO_2}^{P,T} = \left\{ \left(\sum_i M_i X_i \Big/ \rho_{CO_2}^{P,T} \right) - \left[\left(\sum_i M_i X_i - M_{CO_2} X_{CO_2} \right) \Big/ \rho_N^{P,T} \right] \right\} \Big/ X_{CO_2} \tag{2-4}$$

where X_{CO2} is the mole fraction of CO_2 in the melt, M_{CO2} is the molar mass of CO_2, $\rho_{CO_2}^{P,T}$ is the density of the carbonated silicate melt (DG-5) at the neutral buoyancy pressure and temperature, $\rho_N^{P,T}$ is the density of the non-carbonated silicate melt (DG-N) at neutral buoyancy pressure and temperature. The use of this equation requires accurate knowledge of the densities of the melts (Tables 4-1, 4-2, 4-3) and their CO_2 concentrations (Table 4-4).

Table 4-4. Composition used to calculate $\overline{V}_{CO_2}$.

Oxide	DG-5	DG-N
SiO_2	43.25	44.90
Al_2O_3	6.40	6.97
FeO	9.50	11.23
MgO	25.60	27.65
CaO	8.70	5.71
MoO_3	3.05	4.01
CO_2	4.79	0.00
Total	101.2	100.4

Assuming all the CO_2 (~5 wt%, X_{CO2} = 0.0593, Table 4-4) was present in the melt during the run, the resulting $\overline{V}_{CO_2}$ values are 23.71±1.30 cm^3/mol at 4.3±0.1 GPa and 22.06±1.29 cm^3/mol at 5.5±0.1 GPa, both at 1850°C. These values are considered to be minimum, ideal values of $\overline{V}_{CO_2}$ since they represent the maximum possible amount of CO_2 (i.e. the starting material CO_2 concentration) dissolved in the silicate melt. Our CO_2 concentration estimates in the run products based on Ag-coated electron microprobe by difference totals give lower CO_2 contents (~3.5 wt%, X_{CO2} = 0.0441) and thus slightly higher values of $\overline{V}_{CO_2}$which are 25.14 cm^3/mol at 4.3 GPa and 24.39 cm^3/mol at 5.5 GPa.

Because of the extremely low solubility of CO_2 at 1 bar, determining its molar volume is difficult. For this reason, we have calculated a zero pressure value of $\overline{V}_{CO_2}$ = 36.57±1.54 cm^3/mol using the zero pressure melt densities determined above (Lange and Carmichael, 1987; Lange and Carmichael, 1990). This value is similar to the calculated zero pressure value of 35.28 cm^3/mol corrected to 1850°C determined by Ghosh et al. (2007) using carbonate composition values, which may indicate a lack of compositional control on $\overline{V}_{CO_2}$ at very low pressure.

Compositional effects on $\overline{V}_{CO_2}$ have been seen in previous studies (Dobson et al., 1996; Genge et al., 1995; Liu and Lange, 2003; Pan et al., 1991; Stolper and Holloway,

1988; Thibault and Holloway, 1994) (Table 1-1), though some of the variation can be attributed to different temperatures and pressures of the estimates. For example, melts containing potassium, sodium, or calcium carbonates yield significantly different values for $\overline{V}_{CO_2}$ at the same temperatures and pressures. Furthermore it is possible that $\overline{V}_{CO_2}$ derived from studies on non-silicate carbonated liquids are unsuitable for application to carbonated silicate melts such as partial melts of upper mantle peridotite.

In order to calculate K_T and K' for $\overline{V}_{CO_2}$ using our data, we follow the convention proposed by Ghosh et al. (2007) for highly compressible materials and used the Vinet EOS (Vinet et al., 1989):

$$P = 3K_T\left(\frac{V}{V_0}\right)^{\frac{-2}{3}}\left[1-\left(\frac{V}{V_0}\right)^{\frac{1}{3}}\right]\exp\left\{\frac{3}{2}(K'-1)\left[1-\left(\frac{V}{V_0}\right)^{\frac{1}{3}}\right]\right\} \quad \textbf{(4-1)}$$

where P is pressure in GPa, V is the volume, V_0 is the zero pressure volume, K_T is the isothermal bulk modulus, and K' is the pressure derivative of the bulk modulus.

Combining the experimentally determined values from Equation (2-4), the calculated zero pressure value, and the 19.5 GPa value of 19.18 cm^3/mol at 1850°C from Ghosh et al. (2007), we used least square regression to obtain a best fit Vinet EOS curve for $\overline{V}_{CO_2}$ of K_T = 0.36±0.01 GPa and K' = 15.12±0.30 (Figure 4-3). Given the reasonably good fit of the Vinet EOS (R^2 = 0.9927), we are confident that it can adequately explain the compression of $\overline{V}_{CO_2}$.

We also fit our data to the 3rd order Birch-Murnaghan EOS which yielded K_T = 0.1 GPa and K' = 192.3 (Figure 4-3). Both of these curves are meant for use in describing the compressibility of solids, not for liquids, and therefore do not fit ideally.

Unfortunately, there is no equation of state for liquids as yet. In search of a curve that better fits the liquid data, we fit the data to a 3-parameter hyperbolic curve that has been shown to fit experimental data (Agee, 2008b), of the form:

$$f = y_0 + \left(\frac{ab}{b+x} \right) \tag{4-2}$$

where f is equivalent to $\overline{V}_{CO_2}^{P,T}$, x is equivalent to P in GPa, and a, b, and y_0 are constants that describe the shape of the curve. When this equation is fit to our data it becomes (Figure 4-3):

$$\overline{V}_{CO2}^{P,1850} = 17.334 + \left(\frac{19.246 \times 1.985}{1.985 + P} \right) \tag{4-3}$$

We have not, as yet, been able to determine elastic parameters to explain the compression of $\overline{V}_{CO_2}$ from the hyperbolic curve.

Figure 4-3 shows our updated compression curve for $\overline{V}_{CO_2}$, which is now much better constrained for pressures below 10 GPa than the earlier version of Ghosh et al. (2007). The curve shows a rapid decrease in $\overline{V}_{CO_2}$ in the pressure range 0-3 GPa which indicates extremely high compressibility of CO_2 in melts in the shallow upper mantle. In the pressure range 3-5 GPa, the steepness of the curve levels off indicating a much lower compressibility of $\overline{V}_{CO_2}$ in the deeper mantle.

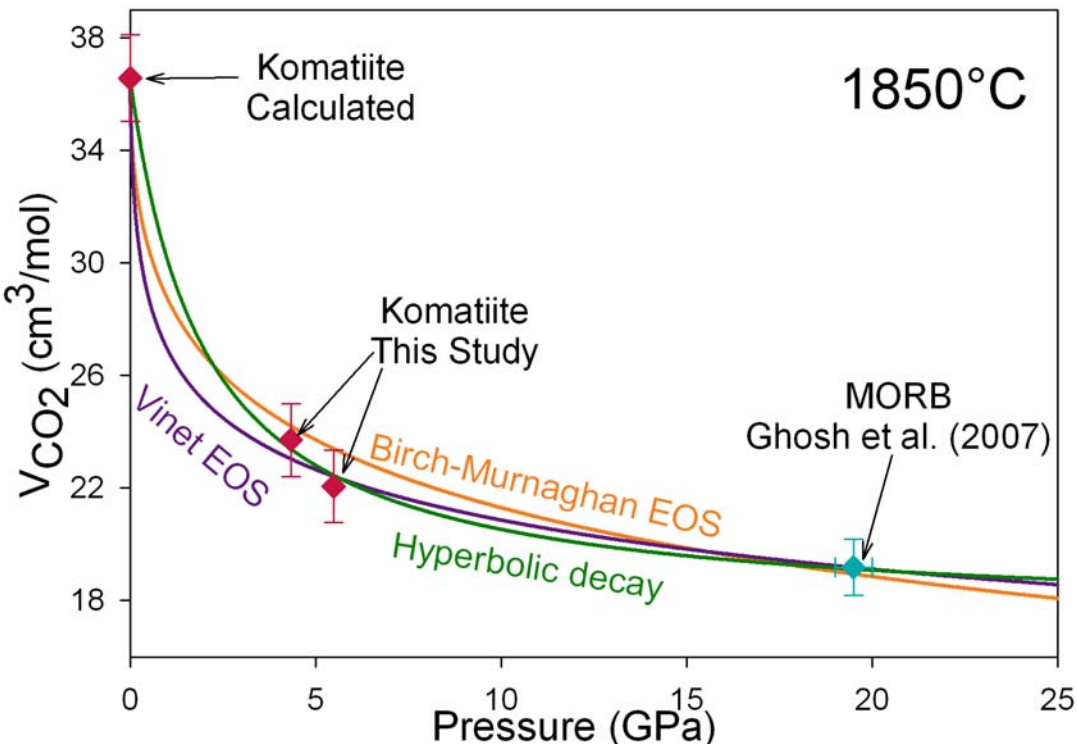

Figure 4-3. Compression curves for CO_2 fit to ideal data, Vinet: K_T = 0.36 GPa, K' = 15.12, R_2 = 0.9927; Hyperbolic: a = 19.25, b = 1.98, y_0 = 17.33, R^2 = 0.9985, Birch-Murnaghan: K_T = 0.1 GPa, K' = 192.3, R^2 = 0.9594.

The values we determined for the Vinet EOS (K_T = 0.36 GPa and K' = 15.12) are different from the values of K_T = 3.7 GPa and K' = 9.0 calculated by Ghosh et al. (2007), but the K_T value is similar to that determined for $\overline{V}_{H_2O}$: K_T = 0.6 GPa and K' = 4.5 (Agee, 2008b) for the Vinet EOS. This may indicate that dissolved water and carbon dioxide have comparable compression behavior in mantle melts at high pressure (Figure 4-4). Both compression curves of CO_2 and H_2O decrease rapidly at low pressure (<5 GPa) and then level off as a function of pressure (Figure 4-4) indicating that compression of both species reaches a maximum – a point beyond which they cannot be compressed any further. The maximum of CO_2 (~15 cm^3/mol) is comparable to the molar volumes of the other liquid oxides (e. g. MgO~12 cm^3/mol, CaO~17 cm^3/mol both at 1600°C: Lange and Carmichael, 1987), which are fairly constant with pressure. Also visible in Figure 4-4 is

that H_2O is more compressible than CO_2, likely due to the smaller size of the H_2O molecule.

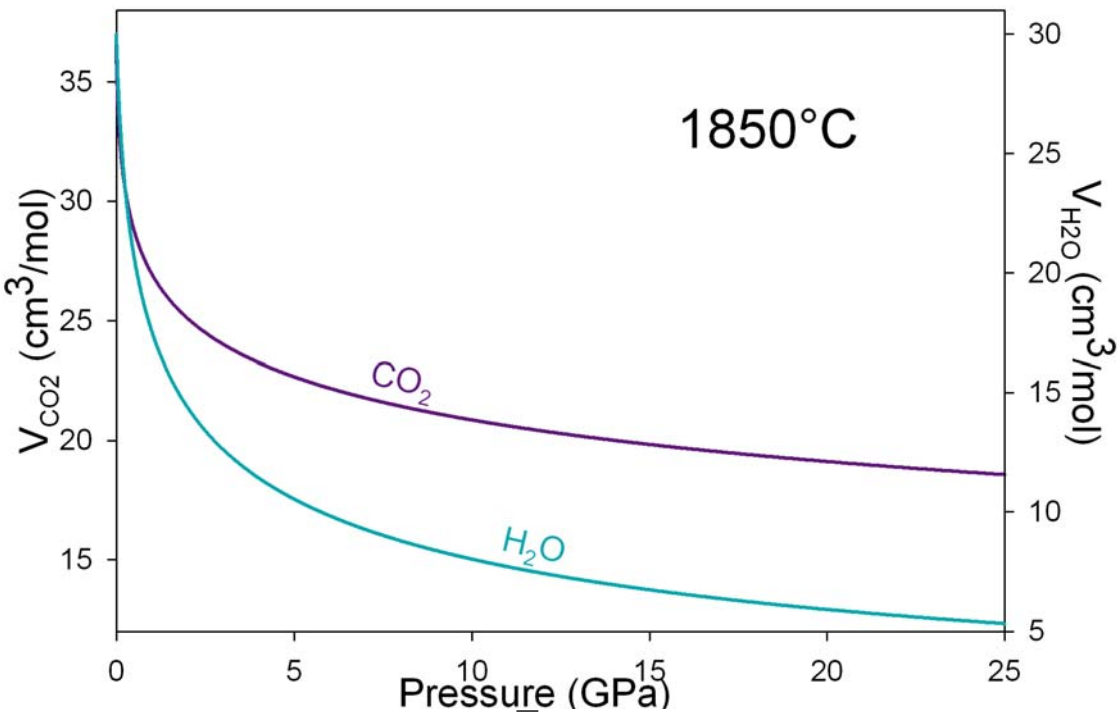

Figure 4-4. Vinet EOS compression curves for $\overline{V}_{CO_2}$(K_T = 0.36 GPa, K' = 15.12, V_0 = 36.57 cm^3/mol) and $\overline{V}_{H_2O}$ (K_T = 0.6 GPa, K' = 4.5, V_0 = 30.01 cm^3/mol). Notice the different scales of the y-axes, this is to make the curves start at the same point.

Chapter 5

Error Analysis

There were several sources of error in this project the largest being compositional variation, see the error bars in Figure 4-3. In order to determine the error in melt density and $\overline{V}_{CO_2}$, several factors were considered: the error from the experiments due to the variation in neutral buoyancy position, the error from different mineral sphere parameters, and the error from the analyzed melt composition. The experimental and mineral sphere parameter errors directly affect the determination of melt density, though it is relatively small. These errors also affect the molar volume calculations, although the compositional error due to the unknown amount of CO_2 in the melt is much more significant.

Density

Because there were several neutral buoyancy results between each sink and float result, different best fit, compression curves were calculated using different melt densities. Four different curves were chosen for each composition based on the placement of the neutral buoyancies. The first set of curves determined was based on the middle of the neutral buoyancy results and used the Birch-Murnaghan EOS. The second set of Birch-Murnaghan curves used the same neutral buoyancy result for the Fo100 crossover due to the smaller amount of scatter, and the highest pressure Fo90 crossover. The third set fit a Birch-Murnaghan curve to all of the neutral buoyancy results, while the forth set used the same neutral buoyancies as the first set, but fit the Vinet EOS rather than the Birch-Murnaghan EOS. They are outlined below in detail:

For DG-5:

1. 5 5.9 – used the neutral buoyancies at 4.7 GPa and 5.9 GPa
2. 5 6.1 – used 4.7 GPa and 6.1 GPa neutral buoyancy values
3. 5 All – used all experimental neutral buoyancy values (Table 4-1)
4. 5 V – used 4.7 GPa and 5.9 GPa values fit to the Vinet EOS

For DG-N:

1. N 5.1 – used the neutral buoyancies at 4.0 GPa and 5.1 GPa
2. N 5.4 – used 4.0 GPa and 5.4 GPa neutral buoyancy values
3. N All – used all neutral buoyancy values (Table 4-2)
4. N V – used 4.0 GPa and 5.1 GPa values fit to Vinet EOS

All DG-5 and DG-N compression curves were calculated using the same zero pressure density and thermal expansion ($\partial\rho/\partial T$) parameters (Table 5-1) calculated from Lange and Carmichael (1987), based on the ideal melt composition (Table 4-4). All densities were corrected to 1850°C, before determining the Birch-Murnaghan curve parameters and $\overline{V}_{CO_2}$ values, using:

$$\rho_T = \rho_{\exp} + \left(T - T_{\exp}\right)\frac{\partial\rho}{\partial T} \tag{5-1}$$

where ρ_T is the density at the reference temperature, T, ρ_{exp} is the density at the experimental temperature, T_{exp}, and $\partial\rho/\partial T$ is the thermal expansion parameter.

Table 5-1. Zero pressure density and thermal expansion parameters used to calculate DG-5 and DG-N compression curves.

DG-5		DG-N	
ρ_0 (g/cm^3)	$\partial\rho/\partial T$ (g/cm^3°C)	ρ_0 (g/cm^3)	$\partial\rho/\partial T$ (g/cm^3°C)
2.59	-2.10x10^{-4}	2.75	-2.11 x10^{-4}

The first set of curves calculated (Table 5-2) were determined from the mineral sphere parameters presented in Chapter 2 (Table 2-2).

Table 5-2. Birch-Murnaghan EOS parameters for different neutral buoyancy results. 5 5.9 and N 5.1 are the results presented in Chapter 4.

	DG-5				DG-N			
	5 5.9	5 6.12	5 All	5 V	N 5.1	N 5.4	N All	N V
K_T (GPa)	17.22	17.62	17.32	17.10	22.89	23.56	22.89	22.83
K'	3.10	3.10	3.10	3.10	3.10	3.10	3.10	3.10

The K_T values for the DG-5 melts vary within 0.52 of each other indicating the robustness of the compression curve for each melt. The DG-N K_T values have slightly more variance (0.73), indicating a worse fit, visible in Figure 4-1. For both melts, these variances are smaller than the symbols on Figures 4-1 and 4-2, and are too small to influence the calculation of $\overline{V}_{CO_2}$.

The density of the melt at the neutral buoyancy point also depends on the density of the mineral spheres. Due to the different analytical techniques used in different studies, the values used to calculate sphere density vary. I used five additional sets of values for the elastic parameters (K_T, K', dK/dT), the thermal expansion (α_0, α_1, α_2), and the zero pressure molar volumes of endmember forsterite and fayalite from different sources (Table 5-3), hereafter 1-4, used the following equations:

$$\alpha(T) = \alpha_0 + \alpha_1 T + \alpha_2 T^{-2} \tag{5-2}$$

$$V_{0,T} = V_{0,298}(T) \exp \int_{298}^{T} \alpha(T) dT \tag{5-3}$$

$$\rho_0 = [MW] / [V_{0,T}] \tag{5-4}$$

$$\rho_{0,Olivine} = \rho_{0,Fo} X_{Mg} + \rho_{0,Fa} X_{Fe} \tag{5-5}$$

$$K_T = \left[K_T (T - T_0) dK/dT\right] X_{Mg} + \left[K_T (T - T_0) dK/dT\right] X_{Fe} \tag{5-6}$$

$$K' = K'X_{Mg} + K'X_{Fe} \tag{5-7}$$

where α_0, α_1, α_2 are thermal expansion parameters for the endmember olivine (Table 5-3), $V_{0,T}$ is the zero pressure volume at experimental temperature T, $V_{0,298}$ is the zero pressure volume at 298 K in cm^3/mol, MW is the molecular weight of the mineral, $\rho_{0,Fo}$ is the zero pressure density of the forsterite endmember, $\rho_{0,Fa}$ is the zero pressure density of the fayalite endmember, X_{Mg} is the Mg number of the olivine, $X_{Fe} = 1 - X_{Mg}$, T_0 is the reference temperature 298 K, K_T is the isothermal bulk modulus of the endmember, dK/dT is its temperature derivative, K' is its pressure derivative (Table 5-3).

Table 5-3. Mineral sphere elastic parameters

	K_T (GPa)	K'	dK/dT	α_0 (x10^{-5})	α_1 (x10^{-9})	α_2	V_0 (cm^3/mol)	
Forsterite	127.5[a]	4.8[a]	-0.02[b]	3.034	7.422	-0.5381[c]	42.99[a]	**1**
	127.84[d]	5.34[e]	-0.02272[d]	2.635	14.036	-0.0000[f]	43.61[f]	**2**
	"	"	"	2.854	10.08	-0.3842[g]	"	**3**
	"	"	"	3.407	8.674	-0.7545[h]	"	**4**
Fayalite	134.6[i]	5.2[j]	-0.024[i]	2.386	11.53	-0.0518[k,l,m]	46.22[i]	**1**
	137.24[n]	5.0[n]	-0.02768[n]	"	"	"	46.38[n]	**2,3,4**
Fo/Fa mix	128.544	5.3	-0.02176[o]					**5**

[a] (Jacobs and de Jong, 2007), [b] (Liu and Li, 2006), [c] (Suzuki, 1975), [d] (Suzuki et al., 1983), [e] (Kumazawa and Anderson, 1969), [f] (Hazen, 1976), [g] (Kajiyoshi, 1986), [h] (Matsui and Manghnani, 1985), [i] (Graham et al., 1988), [j] (Isaak et al., 1993), [k] (Suzuki et al., 1981), [l] (Smyth, 1975), [m] (Hazen, 1977), [n] (Sumino, 1979), [o] (Circone and Agee, 1996)

The fifth set of values (5) is not for endmember olivines, but for olivines of any composition along solid solution lines (Agee and Walker, 1988; Hazen, 1977). For these values the following equations were used (see Agee and Walker, 1988 for details and full references):

$$\rho_{0,T} = \left(954.2X_{Fe} + 535.4X_{Mg} + 399\right) \Big/ \left(289.45 + 17X_{Fe} + 0.00856T + 2.01\times10^{-6}T^2\right) \tag{5-8}$$

$$K_T = \left[K_T\left(T - T_0\right) dK \big/ dT\right] \tag{5-9}$$

Each of these sphere parameters were used to calculate melt density at each neutral buoyancy result (Table 5-4). Then, using the same technique described at the beginning of this chapter for the variation in neutral buoyancy position, compression curves were determined for each sphere parameter (Table 5-5).

Table 5-4. Neutral buoyancy melt density values at experimental pressures and 1850°C for carbonated (DG-5) and non-carbonated (DG-N) runs for each set of olivine values. 1-5 indicate which sphere parameter was used, see Table 5-3.

DG-5						DG-N					
P (GPa)	*ρ* (g/cm^3)					*P* (GPa)	*ρ* (g/cm^3)				
NB	**1**	**2**	**3**	**4**	**5**	NB	**1**	**2**	**3**	**4**	**5**
4.6	3.19	3.12	3.14	3.12	3.13	4.0	3.17	3.11	3.12	3.11	3.12
4.7	3.19	3.12	3.14	3.12	3.13	4.1	3.18	3.11	3.13	3.11	3.12
4.7	3.19	3.12	3.14	3.12	3.13	4.8	3.31	3.24	3.26	3.24	3.26
5.7	3.34	3.28	3.29	3.28	3.29	5.1	3.33	3.26	3.28	3.26	3.28
5.9	3.35	3.29	3.31	3.29	3.30	5.4	3.33	3.27	3.29	3.27	3.28
6.1	3.35	3.29	3.31	3.29	3.30						

The densities that vary most from the ones calculated in Chapter 4 are set 1 which are 0.04-0.05 g/cm^3 lower. Set 3 matches exactly, and sets 2, 4 and 5 vary from 0.01 to 0.02 g/cm^3 above the values used in Chapter 4. These differences do not change the K_T and *K'* determined for their compression curves (Table 5-5) drastically from those determined previously for the Chapter 2 sphere parameters.

Table 5-5. Best fit Birch-Murnaghan K_T (GPa) values to different neutral buoyancies for DG-5 and DG-N keeping *K'* = 3.1. 1-5 indicate which sphere parameter was used, see Table 5-3.

K_T (GPa)	DG-5				DG-N			
Olivine parameter	5 5.9	5 6.12	5 all	5 V	N 5.1	N 5.4	N all	N V
1	15.84	16.20	15.92	15.75	20.56	21.20	20.63	20.51
2	17.80	18.21	17.91	17.71	23.94	24.67	23.93	23.88
3	17.21	17.61	17.31	17.12	22.91	23.58	22.91	22.85
4	17.78	18.19	17.88	17.69	23.91	24.61	23.89	23.86
5	17.38	17.79	17.48	17.29	23.16	23.87	23.14	23.10

As with the density calculations, Set 1 had the most difference from the values in Table 5-2, with K_T values about 1.4 GPa lower for the DG-5 melt and 2.3 GPa lower for the DG-N melt. Accordingly, Set 3 matches best with Table 5-2, while sets 2, 4, and 5

were ~0.6 GPa above the DG-5 K_T values and ~1.0 GPa above the DG-N K_T values. These curves were calculated because they influence the molar volume calculation and induce error onto $\overline{V}_{CO_2}$.

Molar Volume

Due to the ambiguity of the electron microprobe results for carbon, three different composition sets (DG-5 and DG-N, Table 5-6) were used to determine $\overline{V}_{CO_2}$ at each experimental pressure, the best fit Vinet EOS compression curves, and hyperbolic curves from the calculated zero pressure $\overline{V}_{CO_2}$ to 19.18 cm^3/mol at 19.5 GPa and 1850°C from Ghosh et al. (2007) (Tables 5-7 through 5-9). The composition sets were:

1. Ag – averaged probe totals from Ag-coated analyses using the carbon detected by the microprobe for the carbonated composition and the By Difference values for the non-carbonated composition. This represents the maximum amount of CO_2 present in the melt, resulting in the lowest $\overline{V}_{CO_2}$.
2. Start – not a melt composition, but the wt% of each powder added to create the starting mixes with approximately 3 wt% MoO_3 added and normalized to 100%
3. By Diff – the By Difference microprobe results from the Ag-coated experiments

Each of the microprobe compositions (Ag, By Diff) used the averages of the same Ag-coated experiments analyzed with the same conditions (6 carbonated experiments and 3 non-carbonated experiments). The averages for the carbonated experiments include DG-5-1 (32 analysis points), DG-5-4 (27 analyses), DG-5-7 (17 analyses), DG-5-8 (35 analyses), DG-5-14 (23 analyses), and DG-5-16 (23 analyses). The averages for the non-carbonated experiments used DG-N-3 (27 analysis points), DG-N-7 (24 analyses), and DG-N-9 (23 analyses).

Table 5-6. Composition sets used in calculating $\overline{V}_{CO_2}$.

Oxide	Ag		Start		By Diff	
	DG-5	DG-N	DG-5	DG-N	DG-5	DG-N
SiO_2	43.25	44.90	41.99	44.64	43.25	44.90
Al_2O_3	6.40	6.97	6.75	6.98	6.40	6.97
FeO	9.50	11.23	9.70	10.13	9.50	11.23
MgO	25.60	27.65	25.79	27.05	25.60	27.65
CaO	8.70	5.71	7.07	6.81	8.70	5.71
MoO_3	3.05	4.01	3.14	4.39	3.05	4.01
CO_2	4.79	0.00	5.54	0.00	3.51	0.00
Total	101.2	100.4	100.0	100.0	100.0	100.4

The $\overline{V}_{CO_2}$ values determined using the main set of sphere parameters (Table 2-2), the calculated melt densities (Tables 4-1 and 4-2), and the calculated K_T values for the DG-5 and DG-N compression curves are presented in Table 5-7.

Table 5-7. $\overline{V}_{CO_2}$ values for each composition and each NB at pressure, with the best fit Vinet K_T and K' and hyperbolic curve parameters with R^2 values. These values were calculated using sphere parameters presented in Table 2-2.

	Ag	Start	By Diff	5 5.9 N 5.1	5 6.12 N 5.4	5 all N all	5 V N V
P (GPa)	$\overline{V}_{CO_2}$ (cm^3/mol)						
1x10^{-4}	36.57	35.05	37.22	36.57	36.57	36.57	36.57
4.3	23.71	22.73	25.30	23.71	23.68	23.88	23.91
5.5	22.06	21.15	23.79	22.06	22.03	22.43	22.29
	Vinet EOS parameters						
K_T (GPa)	0.36	0.08	2.00	0.36	0.34	0.57	0.51
K'	15.12	21.84	8.92	15.12	15.32	13.545	13.925
R^2	0.9927	0.9841	0.9988	0.9927	0.9924	0.9963	0.9942
	Hyperbolic curve parameters						
a	19.25	17.23	21.06	19.25	19.23	19.38	19.38
b	1.98	1.55	3.22	1.98	1.96	2.17	2.14
y_0	17.33	17.83	16.17	17.33	17.35	17.20	17.20
R^2	0.9985	0.9976	0.9997	0.9985	0.9985	0.9993	0.9988

The $\overline{V}_{CO_2}$ variation based on different compositions (Ag, Start, By Diff, Table 5-7 columns 1-3) is much larger than the variation based on different DG-5 and DG-N compression curves (Table 5-7, columns 4-7). Composition is therefore the largest

source of error – the unknown amount of CO_2 in the melt. Using the $\overline{V}_{CO_2}$ determined from the Ag composition as the ideal, the value of $\overline{V}_{CO_2}$ may be as much as 1.0 cm^3/mol lower if the amount of CO_2 is increased by 0.75 wt%, and as much as 1.7 cm^3/mol higher if the amount of CO_2 is decreased by 1.3 wt% (see error bars on komatiite data in Figure 4-3).

The variation in $\overline{V}_{CO_2}$ due to the different mineral sphere parameters (from Table 5-3) was also calculated (Table 5-9), though the error is much less than that due to the unknown amount of CO_2 present in the melt.

We also calculated $\overline{V}_{CO_2}$ from compositions that contained Mo rather than MoO_3. Because we analyzed for elements with the electron microprobe, the By Diff method required that oxygen be assigned to all cations, then the deficit from 100% was assumed to be due to CO_2. This is appropriate due to the f_{O2}, ~ 1+IW; Mo should be MoO_3 when dissolved in the melt. However, the state of Mo in the quenched samples is more commonly Mo therefore "giving" it oxygen decreases the size of the deficit from 100% and decreases the amount of CO_2 calculated to be in the melt. As Table 5-8 shows, calculating the Mo content of the melt as Mo rather than MoO_3 has little effect on the $\overline{V}_{CO_2}$ values for the Ag and Start melt compositions, while the By Diff values have an increase of ~0.80 cm^3/mol.

Table 5-8. $\overline{V}_{CO_2}$ values for each composition using Mo instead of MoO_3, with the best fit Vinet K_T and K' with R^2 values. These values were calculated using sphere parameters presented in Table 2-2.

	Ag	Start	By Diff
CO_2 (wt%)	4.79	5.60	4.52
P (GPa)	$\overline{V}_{CO_2}$ (cm^3/mol)		
$1x10^{-4}$	36.57	35.05	37.22
4.3	23.96	22.96	26.07
5.5	22.33	21.39	24.65
	Vinet EOS Parameters		
K_T (GPa)	0.55	0.15	3.50
K'	13.67	19.55	7.04
R^2	0.9943	0.9876	0.9996

Of the various sources of error – the error from the experiments due to the variation in neutral buoyancy position, the error from different mineral sphere parameters, and the error from the analyzed melt composition – the unknown amount of CO_2 had the largest effect. The experimental and mineral sphere parameter errors are relatively small, slightly less than the size of the symbols on Figures 4-1 and 4-2. The compositional error due to the unknown amount of CO_2 in the melt is much more significant and is shown in the error bars of Figure 4-3.

Table 5-9. $\bar{V}_{CO_2}$ **values for each composition at pressure, with the best fit Vinet K_T and K' and hyperbolic curve parameters with R^2 values. 1-5 indicate which sphere parameter was used, see Table 5-3.**

	1			2			3			4			5		
	Ag	Start	By Diff	Ag	Start	By Diff	Ag	Start	By Diff	Ag	Start	By Diff	Ag	Start	By Diff
P (GPa)	$\bar{V}_{CO_2}$ (cm^3/mol)			$\bar{V}_{CO_2}$ (cm^3/mol)			$\bar{V}_{CO_2}$ (cm^3/mol)			$\bar{V}_{CO_2}$ (cm^3/mol)			$\bar{V}_{CO_2}$ (cm^3/mol)		
1x10^{-4}	36.57	35.05	37.22	36.57	35.05	37.22	36.57	35.05	37.22	36.57	35.05	37.22	36.57	35.05	37.22
4.3	23.90	22.88	25.65	23.57	22.64	25.10	23.57	22.70	25.12	23.56	22.63	25.09	23.68	22.73	25.27
5.5	22.28	21.32	24.18	21.91	21.04	23.56	21.91	21.12	23.59	21.90	21.03	23.56	22.04	21.14	23.75
	Vinet EOS Parameters			Vinet EOS Parameters			Vinet EOS Parameters			Vinet EOS Parameters			Vinet EOS Parameters		
K_T (GPa)	0.49	0.13	2.50	0.27	0.06	1.70	0.29	0.07	1.90	0.28	0.05	1.70	0.34	0.08	1.95
K'	14.07	20.07	8.17	16.12	22.89	9.46	15.87	22.33	9.08	15.99	23.57	9.46	15.32	21.84	9.00
R^2	0.9942	0.9869	0.9992	0.9914	0.9817	0.9984	0.9914	0.9834	0.9982	0.9913	0.9815	0.9984	0.9925	0.9839	0.9987
	Hyperbolic Parameters			Hyperbolic Parameters			Hyperbolic Parameters			Hyperbolic Parameters			Hyperbolic Parameters		
a	19.37	17.30	21.40	19.17	17.18	20.88	19.16	17.21	20.90	19.16	17.17	20.88	19.23	17.22	21.03
b	2.13	1.65	3.60	1.89	1.48	3.02	1.88	1.52	3.04	1.88	1.47	3.01	1.97	1.54	3.18
y_0	17.21	17.75	15.83	17.41	17.88	16.35	17.42	17.84	16.33	17.42	17.88	16.36	17.35	17.83	16.20
R^2	0.9988	0.9979	0.9998	0.9984	0.9975	0.9996	0.9984	0.9976	0.9996	0.9984	0.9974	0.9996	0.9985	0.9976	0.9997

Chapter 6

Application to the Earth and other Terrestrial Planets

The information from the $\overline{V}_{CO_2}$ compression curve enables more accurate calculation of density and compressibility for carbonated magmas, such as kimberlites and carbonatites. By being able to calculate magma density and knowing the depth of origin of the magma, the minimum amount of CO_2 necessary to cause the magma to be buoyant and possibly erupt can be established (Figure 6-1). This may also indicate minimum lithospheric abundances of CO_2, compared to the magma source region, and give insight into the origin and behavior of these carbonated magmatic systems.

Kimberlites

We have used $\partial V_i/\partial T$ values from Lange and Carmichael (1987) and Liu and Lange (2003) for the liquid oxides (CaO, MgO, SiO_2, etc), the $\overline{V}_{H_2O}$ values from Agee (2008b) and the $\overline{V}_{CO_2}$ values from this study to calculate compression curves for primary kimberlite melts using an expanded version of Equation (1-1). A proposed primary kimberlite melt (Kopylova et al., 2007) contains 9.9 wt% H_2O and 9.1 wt% CO_2. In order to determine its compression curve using the new CO_2 data, we first determined a "dry" kimberlite composition based on the primary melt above and then determined its compression curve (without volatiles) using K_T = 26.7 GPa, K' = 4.0 (Agee and Walker, 1988, 1993) and $\rho_{dry}^{P,T}$ = 2.90 g/cm^3 calculated from Lange and Carmichael (1987). These K_T and K' values are for a komatiite melt because kimberlite has not been studied for its elastic properties. We chose komatiite values because of the silicate melts studied, it has a lower amount of SiO_2 and a higher amount of CaO, and is therefore the closest

approximation of a kimberlite melt. From there we determined $\overline{V}_{CO_2}$ and $\overline{V}_{H_2O}$ at four given pressures and used:

$$\rho_{vol}^{P,T} = \sum_i M_i X_i \Bigg/ \left[\overline{V}_{CO_2}^{P,T} X_{CO_2} + \overline{V}_{H_2O}^{P,T} X_{H_2O} + \left(\sum_i M_i X_i - M_{CO_2} X_{CO_2} - M_{H_2O} X_{H_2O} \right) \Big/ \rho_{dry}^{P,T} \right] \quad \textbf{(6-1)}$$

to calculate the volatile-bearing kimberlite density, $\rho_{vol}^{P,T}$, at those pressures and then fit a Birch-Murnaghan curve to the points. Sparks et al. (2006) suggested that the kimberlite source region could contain 5-20 wt% CO_2 and Brey et al. (1991) discovered that kimberlitic melts could contain more than 20 wt% dissolved CO_2 at pressures greater than 5-6 GPa. We added various amounts of CO_2 and H_2O to the dry kimberlite melt (Table 6-1) and used the above technique to determine the shape of their compression curves (Figure 6-1).

Table 6-1. Kimberlite melt compositions including ρ_0, K_T, and K' for Birch-Murnaghan EOS.

	Kopylova et al. (2007)	Dry	H_2O only	CO_2 only	Max CO_2
SiO_2	26.70	32.95	29.37	29.66	23.07
TiO_2	1.73	2.14	1.90	1.92	1.49
Al_2O_3	1.57	1.94	1.73	1.74	1.36
Cr_2O_3	0.36	0.44	0.40	0.40	0.31
FeO	7.58	9.35	8.34	8.42	6.55
MnO	0.18	0.22	0.20	0.20	0.16
MgO	28.25	34.86	31.07	31.38	24.40
CaO	12.90	15.92	14.19	14.33	11.14
Na_2O	0.10	0.12	0.11	0.11	0.09
K_2O	1.26	1.55	1.39	1.40	1.09
P_2O_5	0.40	0.49	0.44	0.44	0.35
H_2O	9.88	0.00	10.87	0.00	10.00
CO_2	9.07	0.00	0.00	10.00	20.00
Total	99.98	100.0	100.00	100.00	100.00
ρ_0 (g/cm^3)	1.94	2.90	2.06	2.56	1.76
K_T (GPa)	1.77	26.70	2.48	9.80	0.96
K'	11.2	4.0	8.5	9.6	16.7

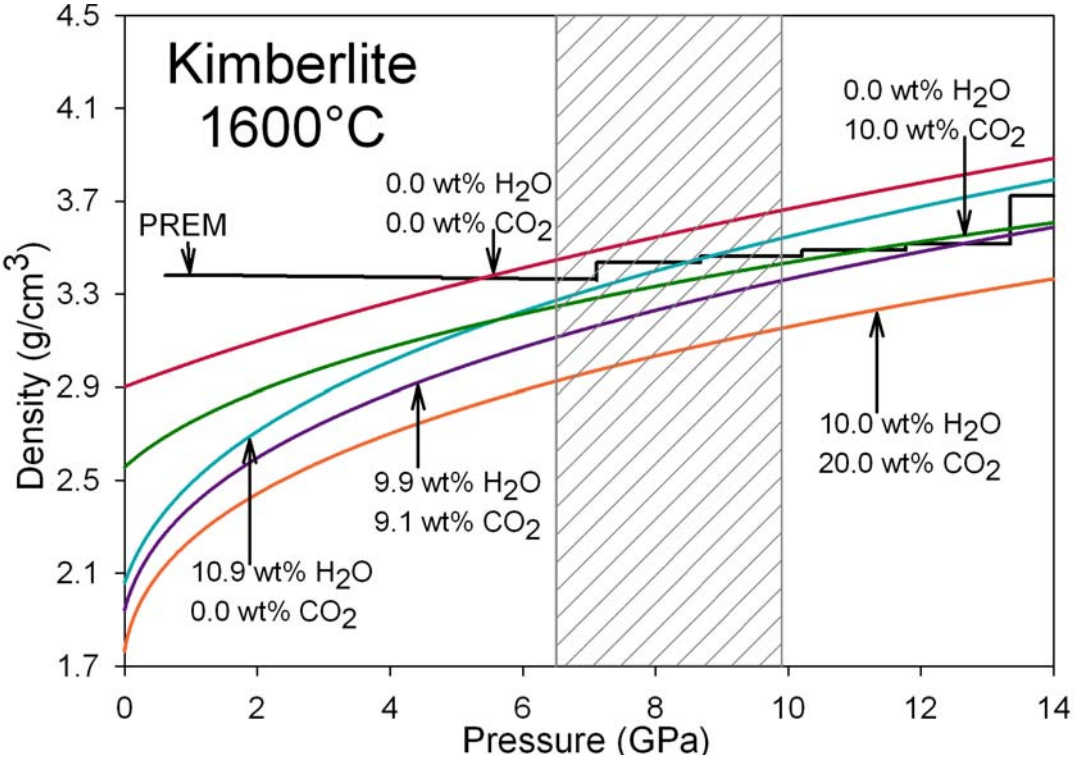

Figure 6-1. Kimberlite melt Birch-Murnaghan compression curves with varying amounts of CO_2 and H_2O. The gray box indicates possible kimberlite source region, ~200-300 km. PREM is the average mantle density (Dziewonski and Anderson, 1981).

The potential source region of kimberlites is approximately 200-300 km depth, so believed due to the presence of diamonds (Canil and Scarfe, 1990). As shown in Figure 6-1, the hypothetical "dry" kimberlite melt is predicted to be denser than a model mantle (Preliminary Reference Earth Model – PREM: Dziewonski and Anderson, 1981) at pressures >5 GPa, and would be too dense to rise from a depth greater than 200 km or even 150 km. The proposed primary melt (9.9 wt% H_2O and 9.1 wt% CO_2) would be less dense than the average mantle (to pressures ≤13 GPa) and therefore could rise to the surface from the kimberlite source region. The maximum amount of CO_2 that can be dissolved in a kimberlitic melt, 20 wt%, could have a source region in the transition zone (~16 GPa). The presence of majorite inclusions in some kimberlite-derived diamonds

may support this theory, as these particular garnets have been shown to form at pressures ≥13.5 GPa, the uppermost limit of the transition zone (Ringwood et al., 1992).

If the $\overline{V}_{CO_2}$ compression curve used is not the ideal one (K_T = 0.36 GPa, K'' = 15.12, CO_2 = 4.8 wt%), but instead the curve based on the starting composition (K_T = 0.08 GPa, K'' = 21.84, CO_2 = 5.5 wt%) or the composition with CO_2 determined by difference (K_T = 2.00 GPa, K'' = 8.92, CO_2 = 3.5 wt%), the elastic parameters of a kimberlite compression curve change. To demonstrate this, we used the CO_2 only kimberlite composition (Table 6-1) and calculated Birch-Murnaghan compression curves based on the different values of $\overline{V}_{CO_2}$ determined from the different $\overline{V}_{CO_2}$ compression curves (Table 6-2, Figure 6-2).

Table 6-2. Birch-Murnaghan EOS elastic parameters for kimberlite melt with only 10.0 wt% CO_2 based on different $\overline{V}_{CO_2}$ compression curves.

	Ideal	Starting	By Difference
ρ_0 (g/cm^3)	2.56	2.58	2.55
K_T (GPa)	9.80	8.87	13.07
K'	9.60	11.35	6.80

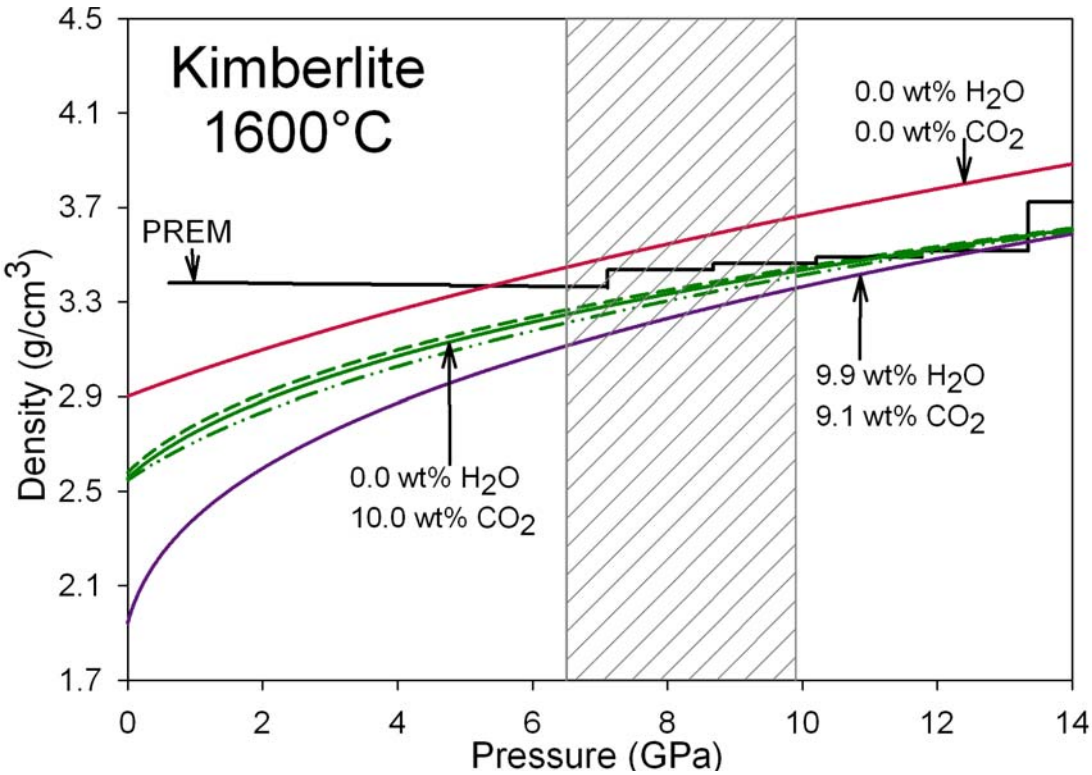

Figure 6-2. Birch-Murnaghan compression curves for a kimberlite melt with only 10.0 wt% CO_2 compared to the "dry" curve and the proposed primary melt – compositions in Table 6-1. The solid green curve is based on the ideal $\overline{V}_{CO_2}$ values, the dashed (- - -) green curve is based on the starting composition CO_2 value, and the dashed/dotted (– · · –) green curve is based on the By Diff CO_2 value.

The differences in the 10.0 wt%CO_2 kimberlite compression curves determined from the different $\overline{V}_{CO_2}$ curves are very small (Figure 6-2). As could be expected, the curve that used $\overline{V}_{CO_2}$ calculated from a higher CO_2 content (Starting amount-5.5 wt% CO_2) is slightly above the ideal curve (4.8 wt% CO_2), while the curve that used $\overline{V}_{CO_2}$ calculated from a lower CO_2 content (By Diff amount-3.5 wt% CO_2) is slightly below the ideal curve. All three curves have similar compressional behaviors and crossover with PREM at relatively the same point (~11 GPa).

We do not know how much CO_2 is present in our experiments during the run, but we are confident that it is there. The $\overline{V}_{CO_2}$ values we calculated are ideal, but given the good fit of the compression curve to the density calculations of kimberlite melts, we feel

that they are a good first approximation. Also, given the relatively small variance in the kimberlite curves based on different possible CO_2 contents of experimental melts and their $\overline{V}_{CO_2}$ values, we are confident that the ideal values are close to reality. The $\overline{V}_{CO_2}$ values determined by these experiments can be used to calculate the density of carbonated mantle melts. The density calculations can then be applied to magma mobility in the mantle and planetary differentiation scenarios where CO_2 is present.

Appendices

Appendix A

Experiments

This appendix gives the details of the experiments. Included is a schematic diagram of the interior of an octahedron (Figure A-1), tables summarizing the conditions of carbonated (Table A-1), non-carbonated (Table A-2), and "andesite" (Table A-3) experiments along with back-scatted electron (BSE) microprobe images of analyzed carbonated (Figures A-2 through A-10), non-carbonated (Figures A-11 through A-18), and "andesite" (Figure A-19) experiments. Following those are the conversion steps from Equation (1-1) to (2-4) to calculate $\overline{V}_{CO_2}$.

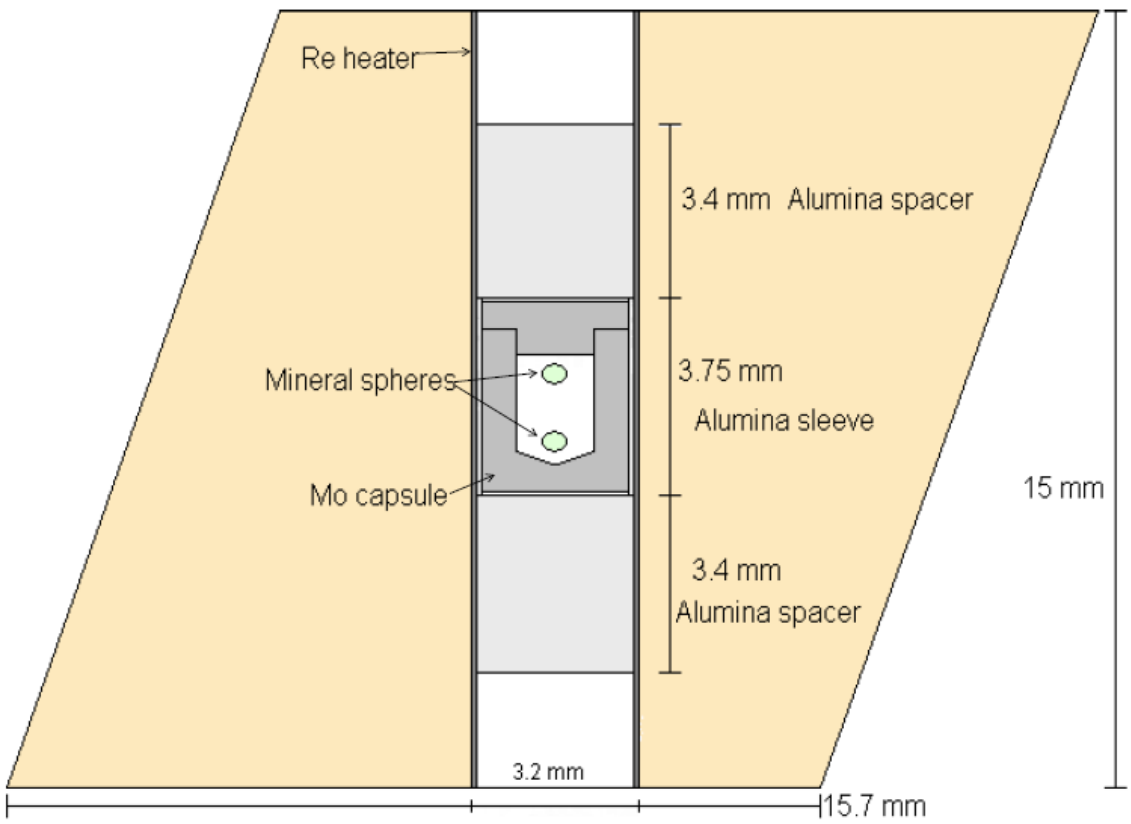

Figure A-1. Cross section of ceramic octahedron with experimental set up. Drawn to scale.

Table A-1. Experimental run conditions and results for carbonated experiments.

Sample		Pressure (bars of oil)	Pressure (GPa)	Temp (°C)	Ramp Rate (°C/min)	Time (sec)	Spheres (μm)		Position	Spacers (mm)	Sleeve (mm)	Notes	Alumina
A457	DG-5-1	58.2-56.6	4.7	1815	n/a	25	Fo 100	640x640 600x640	NB				Yes
A460	DG-5-4	59.0-57.7	4.8	1825	n/a	30	Fo 100	650x480 650x460	Float	3.44	3.78		Yes
A464	DG-5-7	55.4	4.6	1800-1810	n/a	30	Fo 100	600x700 750x500	NB	3.34 3.37	3.75		
A488	DG-5-9	51.1-50.0	4.3	1800	450	30	Fo 100	510x530 480x450	Sink	3.35 3.45	3.75		No
A508	DG-5-11	69.9	5.6	1850	400	30	Fo 90	440x370 390x370	Sink	3.40 3.20	3.70		Yes
A555	DG-5-14	76.7	6.1	1950	350	30	Fo 90	500x460 450x520	NB	3.40 3.43	3.76	reseating	Yes
A561	DG-5-16	79.2	6.3	1950	350	30	Fo 90	500x380 530x430	Float	3.34 3.32	3.80		Yes
QP153	DG-5-17	112	1.0	1779		30	none	n/a	n/a	n/a	n/a	looking for bubbles	
A650	DG-5-18	58.4-58.5	4.8	1850	350	30	Fo 100	600x520 560x510	Float	3.25 3.22	3.84		
A675	DG-5-19	48.4-48.2	4.1	1800	350	30	Fo 100	570x430 520x430	Sink	3.38 3.39	3.73		
A696	DG-5-20	56.3-56.5	4.7	1800	350	30	none	n/a	n/a	3.31 3.32	3.72		
A707	DG-5-21	56.4-56.3	4.7	1800	350	30	Fo 100	650x570 630x590	NB	3.38 3.39	3.73		No
A718	DG-5-22	73.6	5.9	1950	350	35	Fo 90	580x510 580x470	NB	3.32 3.33	3.82		
A725	DG-5-23	70.9-71.1	5.7	1950	350	45	Fo 90	540x490 500x480	NB	3.39 3.40	3.79		

The following figures are back-scattered electron images of polished carbonated experiments. Arrows indicate top of the capsule during run.

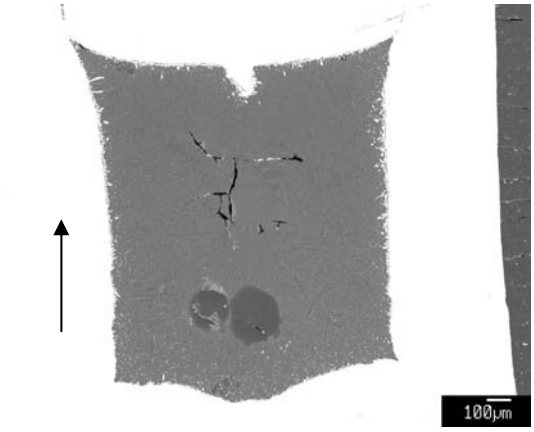

Figure A-2. DG-5-9

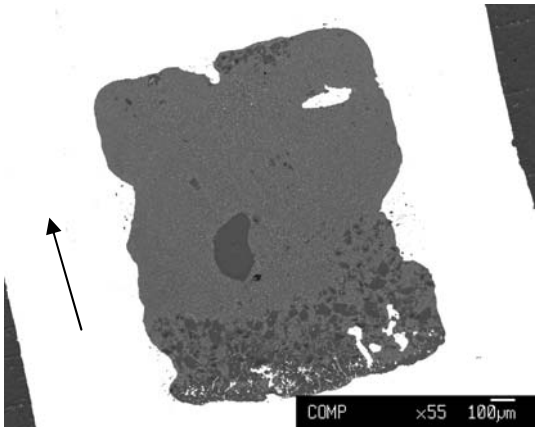

Figure A-3. DG-5-11

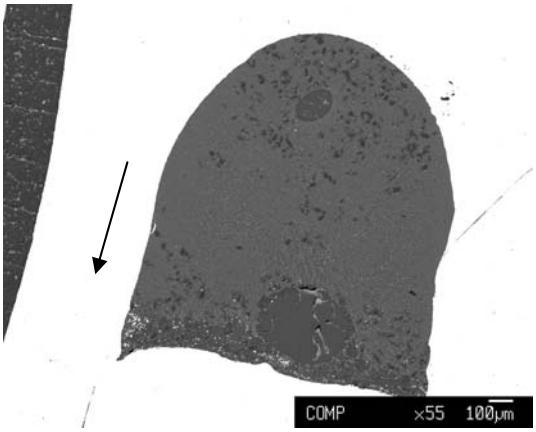

Figure A-4. DG-5-14

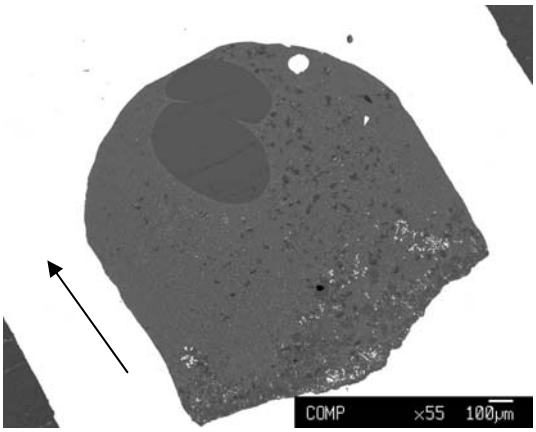

Figure A-5. DG-5-16

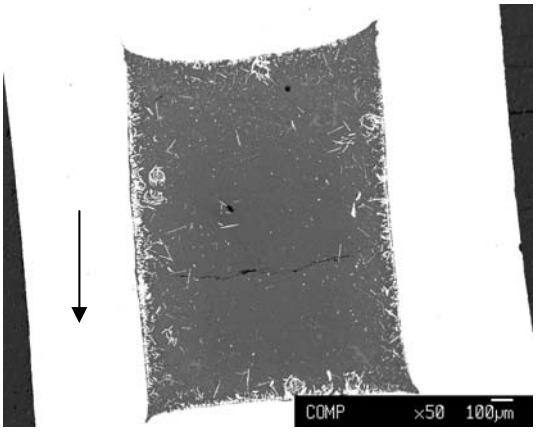

Figure A-6. DG-5-17

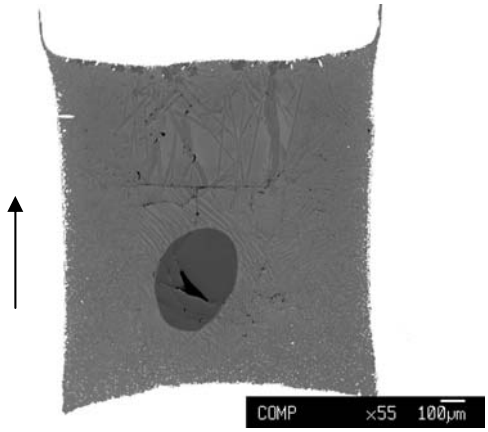

Figure A-7. DG-5-19

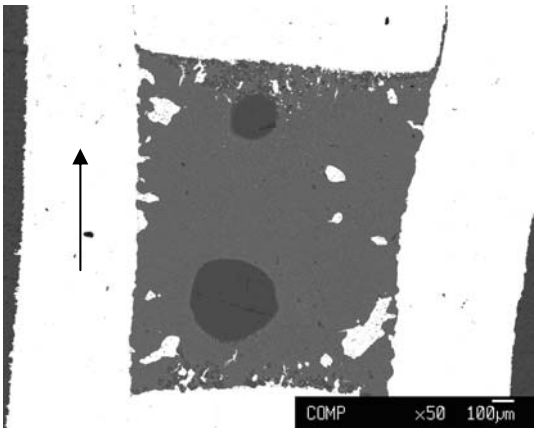

Figure A-8. DG-5-21

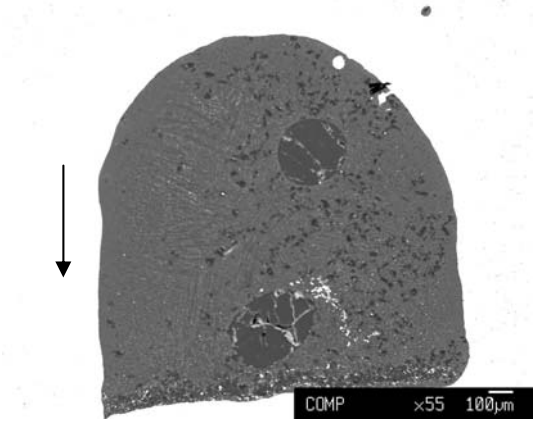

Figure A-9. DG-5-22

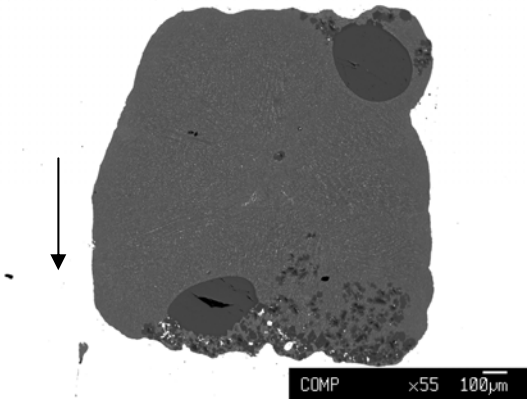

Figure A-10. DG-5-23

Table A-2. Experimental run conditions and results for non-carbonated experiments.

Sample		Pressure (bars of oil)	(GPa)	Temp (°C)	Ramp Rate (°C/min)	Time (sec)	Spheres (μm)	Position	Spacers (mm)	Sleeve (mm)	Notes	Alumina
A496	DG-N-3	45.6-44.9	3.9	1850	400	30	Fo 100 510x420 470x490	Sink	3.45 3.38	3.70	1845-1852	No
A501	DG-N-7	48.7	4.1	1850	400	30	Fo 100 480x420 430x360	Float	3.40 3.50	3.80		No
A562	DG-N-8	65.8	5.3	1950	350	30	Fo 90 420x460 580x420	Not sink	3.30 3.40	3.76	One sphere	No
A591	DG-N-12	62.6-62.4	5.1	1925	350	30	Fo 90 600x500 600x400	Not float	3.37 3.39	3.76	One sphere	No
A592	DG-N-13	69.9-68	5.6	1925	350	30	Fo 90 950x500 850x600	Float	3.30 3.40	3.70		Yes
A598	DG-N-14	62.1	5.1	1925	350	30	Fo 90 800x500 550x450	NB	3.35	3.63		No
A603	DG-N-15	59.4-59.1	4.9	1925	350	30	Fo 90 770x590 830x500	Not sink	3.30 3.35	3.82	One sphere	
A608	DG-N-17	58.6-58.4	4.8	1925	350	30	Fo 90 570x530 550x590	NB/Float	3.40 3.41	3.74		No
A612	DG-N-18	54	4.5	1925	350	30	Fo 90 600x530 490x550	Not sink	3.24 3.26	3.89	One sphere	No
A617	DG-N-19	50.2-49.8	4.2	1900	350	30	Fo 90 640x510 520x580	NB	3.40	3.77	Furnace ASU capsule	Yes
A626	DG-N-20	45.4-44.9	3.9	1850	350	30	Fo 100 580x510 600x520	Sink	3.31 3.36	3.80		No
A654	DG-N-22	54.0-54.1	4.5	1925	350	45	Fo 90 620x580 600x580	Sink	3.19 3.20	3.80		No
A655	DG-N-23	48.6-48.7	4.1	1850	350	30	Fo 100 560x470 590x550	NB	3.28 3.29	3.90		No
A670	DG-N-26	51.6	4.3	1850	350	45	Fo 100 640x460 640x500	Float	3.28 3.29	3.75		No
A724	DG-N-32	71.1	5.7	1975	350	45	Fo 90 560x460 650x440	Not Sink	3.40 3.41	3.79	Furnace overnight	No
A729	DG-N-33	66.4-66.7	5.4	1975	350	23	Fo 90 630x570 610x560	NB	3.34 3.35	3.75	Furnace 1.5 hr	

The following figures are back-scattered electron images of polished non-carbonated experiments. Arrows indicate top of the capsule during run.

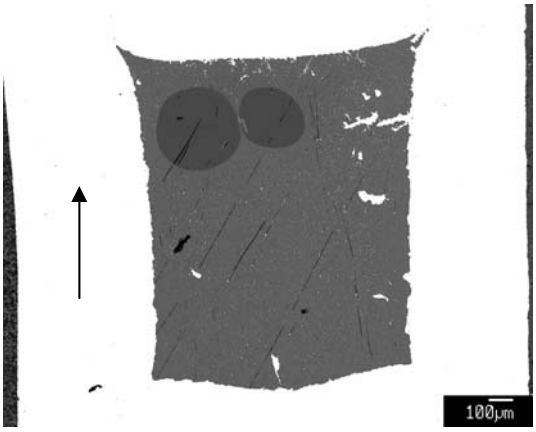

Figure A-11. DG-N-7

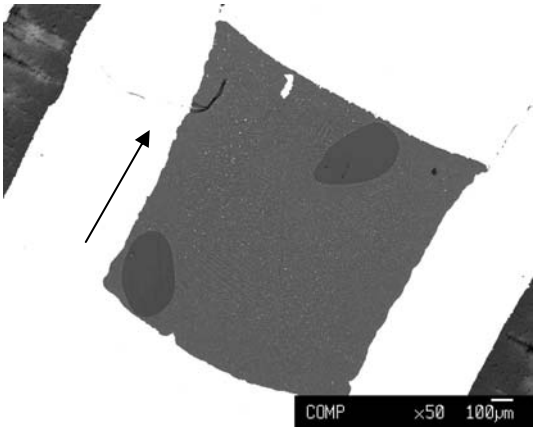

Figure A-12. DG-N-14

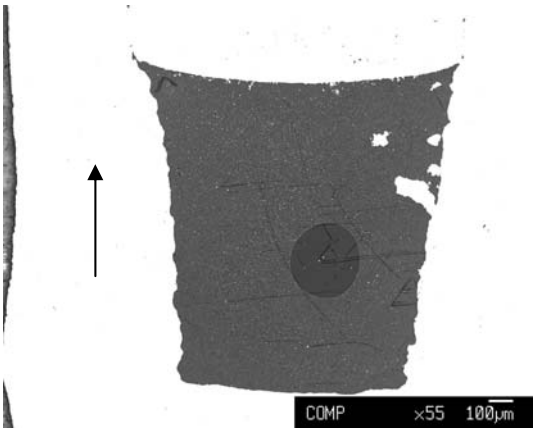

Figure A-13. DG-N-17

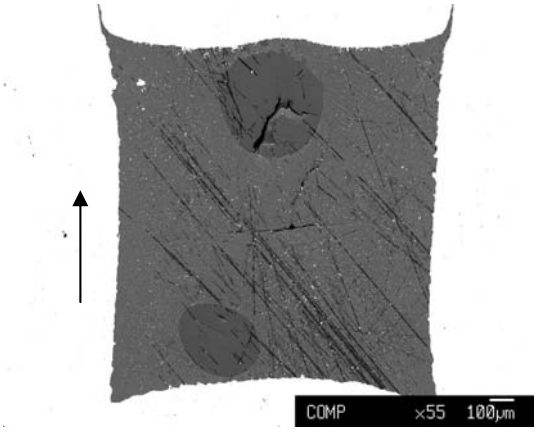

Figure A-14. DG-N-19

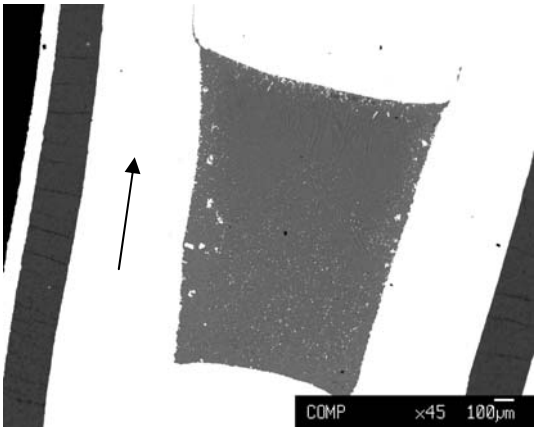

Figure A-15. DG-N-20

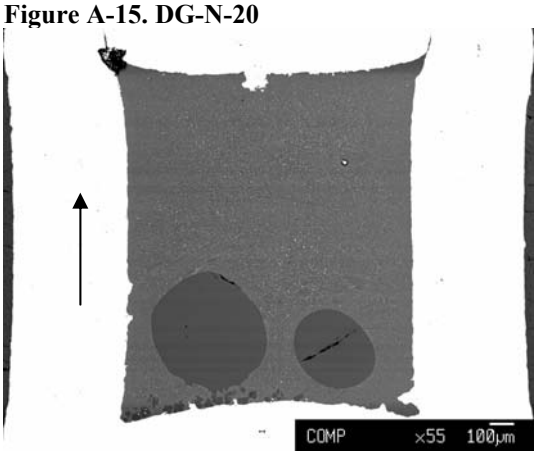

Figure A-16. DG-N-22

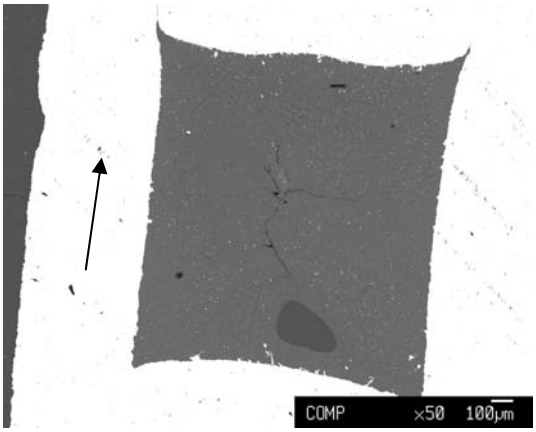

Figure A-17. DG-N-23

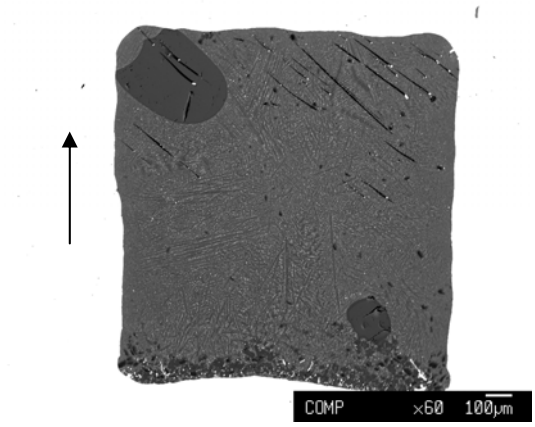

Figure A-18. DG-N-33

Table A-3. Experimental run conditions for "andesite" experiment.

Sample		Pressure (bars of oil)	Pressure (GPa)	Temp (°C)	Ramp Rate (°C/min)	Time (sec)	Spheres (μm)	Spacers (mm)	Sleeve (mm)	Notes Alumina
A683	And-5-1	46.9-47.0	4.0	1900	350	60	none	3.27 3.27	3.71	No

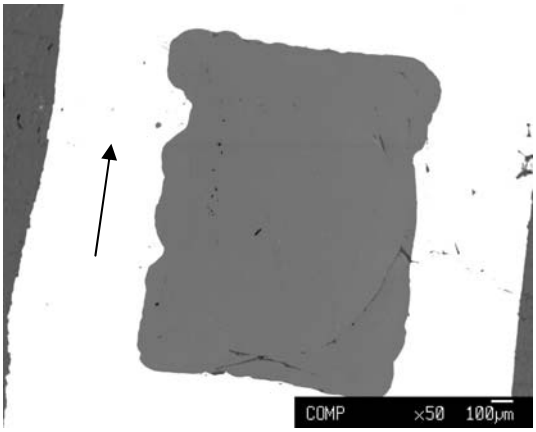

Figure A-19. And-5-1

Conversion steps from the equation of Bottinga and Weill (1970) (Equation 1-1) to the one used for calculating $\overline{V}_{CO_2}$ (Equation 2-4).

$$\rho = \sum_i X_i M_i / X_i \overline{V}_i$$

$$X_A \overline{V}_A + X_B \overline{V}_B + \ldots = \sum_i X_i M_i / \rho$$

$$\overline{V}_A = \left(\sum_i X_i M_i / \rho - X_B \overline{V}_B \right) \Big/ X_A$$

$$\overline{V}_A = \left(\sum_i X_i M_i / \rho - X_B M_B / \rho_B \right) \Big/ X_A$$

$$\overline{V}_A = \left[\sum_i X_i M_i / \rho - \left(\sum_i X_i M_i - X_A M_A \right) \Big/ \rho_B \right] \Big/ X_A$$

$$\overline{V}_{CO_2}^{P,T} = \left\{ \left(\sum_i M_i X_i \Big/ \rho_{CO_2}^{P,T} \right) - \left[\left(\sum_i M_i X_i - M_{CO_2} X_{CO_2} \right) \Big/ \rho_N^{P,T} \right] \right\} \Big/ X_{CO_2}$$

Appendix B

Electron Microprobe

In this section we outline our attempts at using the electron microprobe to detect carbon directly along with the results. For discussion of our Ag-coated attempts see Chapter 3. After unable to accurately detect the carbon in out samples using the Ag-coat and an accelerating voltage of 15 kV, a current of 2.5×10^{-8} A, and a beam diameter of 20 μm, we altered the operating conditions. Because we were also trying to detect O directly, we altered operating conditions to an accelerating voltage of 12 kV, a current of 2.0×10^{-8} A, and a beam diameter of 20 μm, but to no avail.

Because we had some success detecting carbon in gold-coated (Au-coat) carbonates, we then switched to an Au-coat for the experiments. The coat was applied simultaneously to the samples and standards to bypass any issues with different coat thickness between the standards and samples. However, we have not had much success with the detection of carbon in quenched silicate melts. The wt% totals are extremely high (110-130) for the Au-coated experiments, most obviously due to the high amount of oxygen detected (50-55 wt% rather than 45 wt% expected, see Tables B-3 through B-10).

We also tried using different carbon standards (SiC, calcite and dolomite) and different operating conditions, hoping to minimize the amount of carbon detected in samples without carbon. This would then allow us to subtract out the background carbon form the carbonated samples. This also has not yet worked. To ensure that the water used in grinding the samples was not dissolving carbonates (Brooker, 1998; Brooker et al., 2001a; Dasgupta et al., 2007; Wallace and Green, 1988), we used kerosene and anhydrous alcohol in place of water for some carbonated experiments which we then

analyzed with the microprobe and FTIR, but no difference in results were apparent. See Table B-2 for all Au-coated operating conditions and the experiments analyzed and Tables B-3 through B-10 for the analytical results.

Two ways to detect elements using the microprobe are by area and by time. Analysis by area takes the first order peak determined on the standard and uses the upper and lower background limits set around that peak and to determine how much of the element is in the sample by calculating the area under the curve. This is most used when analyzing for an element whose peak may move relative to the standard peak. Analysis by time is more common and uses the first order peak determined on the standard and searches for the same peak on the sample. One problem when analyzing for carbon with the microprobe is the presence of oxygen. The Kα carbon peak using the LDE2 spectrometer is located at ~124 mm, but there is a shoulder in the peak that could be a secondary oxygen peak at ~130 mm. Because the amount of oxygen is so much greater than that of carbon, interference from this potential oxygen peak can raise the background in the location of the carbon peak. When analyzing carbon by area, this will increase the amount of carbon detected if the background for carbon analysis is placed too high, but lower it if the background is set to exclude the oxygen peak. When analyzing carbon by time, the effect of the oxygen peak is less obvious, but still may cause the amount of carbon detected to be too large.

Table B-1. Operating conditions, standards, and experiments analyzed with an Ag-coat by the electron microprobe.

Date	Exp. Analyzed	Standards	Elements	Test	Accl. Volt. (KeV)	Current (nA)	Probe Dia. (µm)	Std Conditions Peak/Back (s)	Notes
3/7/08	DG-5-1 DG-5-4 DG-5-8	SiC Andradite Olivine Capsule (DG-5-1)	C Fe, Al, Ca Mg, Si, O Mo		15	25	20		
4/30/08	DG-5-7 DG-5-8	SiC Chromite Andradite Olivine Capsule (DG-5-1)	C Cr Fe, Al, Ca, O, Mg, Si Mg, Si, O Mo		15	25	20	O as time	Ag paste Samples coated on 4/1 Standards coated separately
5/22/08	DG-5-1 DG-5-4	SiC Olivine Andradite Capsule (DG-5-1)	C Mg, Si, O Fe, Al, Ca Mo		15	25	20	30/10 30/15 O 20/10 Mg, Si, Fe, Al, Ca, Mo Time not area	Sample DG-5-4 charging
8/29/08	DG-5-4 DG-5-9 DG-N-3	SiC Olivine Kaersutite Capsule (DG-5-4)	C Mg, Si, O Fe, Al, Ca Mo		12	20	20	C as time	Samples coated on 8/27 Standards coated separately
9/5/08	DG-5-4 DG-5-9 DG-N-3 DG-N-7	SiC Olivine Kaersutite Capsule (DG-5-4)	C Mg, Si, O Fe, Al, Ca Mo	1 2 3	12 12 12	20 25 20	20 20 20	O on area O as time O on area, no C	
2/27/09	DG-5-14 DG-5-16 DG-N-9	SiC Olivine Kaersutite Capsule	C Mg, Si, O Fe, Al, Ca Mo		15	25	20	C on time	Samples and standards coated together

Table B-2. Operating conditions, standards, and experiments analyzed with an Au-coat by the electron microprobe. Experiments marked with * were ground and cleaned using kerosene and anhydrous alcohol.

Date	Exp. Analyzed	Standards	Elements	Test	Accl. Volt. (KeV)	Current (nA)	Probe Dia. (µm)	Std Conditions Peak/Back (s)	Notes
8/27/09	DG-5-11 DG-5-14 DG-5-16 DG-N-9 DG-N-13 DG-N-14 DG-N-19	SiC	C		15	25	20		
		Olivine	Mg, Si, O						
		Kaersutite	Fe, Al, Ca						
		Capsule (DG-N-9)	Mo						
11/6/09	DG-N-22 DG-N-21 DG-5-17 DG-N-17 DG-N-24	Dolomite	C	1	15	20	10	30/10	Samples and standards on 11/6
		Olivine	Mg, Si, O	2	15	20	10	15/10	
		Kaersutite	Fe, Al, Ca	3	15	25	20	10/5	
		Capsule	Mo	4	15	25	20	30/10	
12/4/09 12/5/09	DG-5-17* DG-N-22	Dolomite	C	1	12	20	10		Samples and standards on 12/3
		Olivine	Mg, Si, O	2a	10	20	20		
		Kaersutite	Fe, Al, Ca	2b	10	20	20	Calcite	
		Capsule (DG-5-17)	Mo	4	10	20	50		
				5a	10	40	50		
				5b	10	40	50	C on Area	
				6	10	60	50		
				7	10	80	50		
				8	10	100	50		
				9	10	80	50	10/5	
1/22/10	And-5-1* DG-5-19*	Dolomite	C	1	12	20	50	10/5	Samples and standards on 1/21
		Olivine	Mg, Si, O	2	12	40	50	10/5	
		Kaersutite	Fe, Al, Ca	3	12	10	10	20/10	
		Capsule (And-5-1)	Mo						
3/25/10	DG-5-14 DG-5-16 DG-N-9 DG-N-17 DG-N-22 DG-N-25	Dolomite	C		15	25	20	20/10	Samples and standards on 3/25
		Olivine	Mg, Si, O						
		Kaersutite	Fe, Al, Ca						
		Capsule (DG-5-14, DG-5-16)	Mo						
3/26/10	DG-5-22 DG-N-31	Dolomite	C	1	15	25	20	20/10	Samples and standards on 3/26
		Olivine	Mg, Si, O	2	10	40	50	20/10	
		Kaersutite	Fe, Al, Ca	3	10	80	50	20/10	
		Capsule (DG-5-22)	Mo						
4/16/10	DG-N-33 DG-N-22 DG-5-23 DG-N-22	Dolomite	C	1	15	25	20	20/10	Samples and standards on 4/15
		Olivine	Mg, Si, O	2	10	80	50	20/10	
		Kaersutite	Fe, Al, Ca	3	10	60	50	20/10	
		Capsule (DG-N-22, DG-5-23)	Mo						

These tables show an average of microprobe data for each experiment analyzed and calculated oxide amounts on a given date under the same conditions, i.e. an analysis taken with an accelerating voltage = 15 kV, a current = 2.5×10^{-8} A, a beam diameter = 20 μm, and SiC as the carbon standard were not averaged with an analysis taken with an accelerating voltage = 12 kV, a current = 2.0×10^{-8} A, a beam diameter = 20 μm, and carbonate as the carbon standard. Also shown are the CO_2 amounts determined from microprobe analyses (Probe Carbon), and the amount of CO_2 determined by the difference from at total of 100 (By Difference). The Peak/Back (s) row indicates the amount of time spent analyzing for the carbon peak, and the time spent analyzing the background. The analyses without a Peak/Back value used a peak of 30 seconds and background of 10 seconds. Experiments with an * are those that were ground using kerosene and alcohol, rather than water.

Table B-3. Average electron microprobe values and resultant oxides values including the wt% CO_2 determined from the microprobe values and the amount when calculated by difference for carbonated experiments DG-5-1, 4, 7, 8, 9.

Sample	DG-5-1		DG-5-4				DG-5-7	DG-5-8		DG-5-9
Date/Coat	3-7 Ag	5-22 Ag	3-7 Ag	5-22 Ag	9-5 Ag1	9-5 Ag2	4-30 Ag	8-27 Au	4-30 Ag	9-5 Ag1
Accel. Volt. (KeV)	15	15	15	15	12	12	15	15	15	12
Current (nA)	25	25	25	25	20	25	25	25	25	20
Probe Dia. (µm)	20	20	20	20	20	20	20	20	20	20
C Std	SiC	SiC	SiC	SiC	SiC	SiC	SiC	SiC	SiC	SiC
Peak/Back (s)										
# of Analyses	6	26	7	17	9	5	17	4	20	22
Meas. Elm %										
Mg	17.97	14.56	13.24	14.33	17.35	17.19	15.02	14.36	15.19	16.46
Al	2.46	3.58	3.01	4.02	4.41	2.70	4.12	2.65	3.97	4.01
Si	17.82	19.43	22.01	18.18	21.52	24.25	20.13	19.28	19.03	20.08
Ca	3.01	6.20	9.11	5.30	6.81	6.18	6.33	6.67	5.60	5.69
Fe	13.50	7.83	6.02	6.26	8.62	7.65	7.98	8.13	8.93	7.82
Mo	1.60	1.63	1.56	1.74	1.70	1.61	1.81	2.76	3.09	2.37
O	38.93	44.42	42.31	44.20	55.05	29.96	43.73	42.33	41.66	46.20
C	0.95	2.00	0.99	2.74	2.07	1.97	1.41	1.32	1.19	1.31
Total	96.23	99.65	98.25	96.76	117.53	91.52	100.52	97.48	98.67	103.94
MgO	29.81	24.14	21.96	23.77	28.78	28.51	24.91	23.81	25.18	27.29
Al_2O_3	4.65	6.77	5.69	7.59	8.33	5.10	7.78	5.00	7.51	7.57
SiO_2	38.11	41.57	47.10	38.89	46.03	51.88	43.06	41.24	40.72	42.96
CaO	4.21	8.67	12.75	7.41	9.53	8.65	8.85	9.33	7.84	7.96
FeO	17.37	10.08	7.75	8.05	11.09	9.84	10.26	10.46	11.49	10.06
MoO_3	2.40	2.44	2.34	2.61	2.56	2.41	2.72	4.13	4.64	3.56
Probe Carbon										
CO_2	3.48	7.32	3.63	10.05	7.57	7.23	5.18	4.83	4.36	4.81
Total	100.02	100.99	101.20	98.36	113.89	113.63	102.76	98.80	101.74	104.21
By Difference										
CO_2	3.46	6.33	2.42	11.69	0.00	0.00	2.42	6.03	2.62	0.60
Total	100.00	100.00	99.99	100.00	106.31	106.40	100.00	100.00	99.99	100.00

Table B-4. Average electron microprobe values and resultant oxides values including the wt% CO_2 determined from the microprobe values and the amount when calculated by difference for carbonated experiments DG-5-11, 14, 16, 19.

Sample	DG-5-11	DG-5-14			DG-5-16			DG-5-19*		
Date/Coat	8-27 Au	2-27 Ag	8-27 Au	3-25 Au1	2-27 Ag	8-27 Au	3-25 Au1	1-22 Au1	1-22 Au2	1-22 Au3
Accel. Volt. (KeV)	15	15	15	15	15	15	15	12	12	12
Current (nA)	25	25	25	25	25	25	25	20	40	10
Probe Dia. (µm)	20	20	20	20	20	20	20	50	50	10
C Std	SiC	SiC	SiC	Dol	SiC	SiC	Dol	Dol	Dol	Dol
Peak/Back (s)				20/10			20/10	10/5	10/5	20/10
# of Analyses	4	23	3		21	3	6	2	2	2
Meas. Elm %										
Mg	14.36	15.82	18.22	16.93	16.57	15.79	17.72	16.89	16.76	19.16
Al	2.65	2.99	2.84	2.70	2.32	1.46	2.92	4.31	4.31	3.32
Si	19.28	21.58	21.24	21.42	21.63	22.38	22.55	20.64	20.49	18.62
Ca	6.67	6.66	6.84	7.00	7.03	8.26	7.27	6.17	6.16	4.69
Fe	8.13	5.53	5.80	6.23	6.64	7.24	6.27	8.68	8.70	10.53
Mo	2.76	2.34	1.77	2.48	2.33	1.82	2.09	2.99	3.05	3.37
O	42.33	40.72	50.62	48.11	43.76	44.13	51.61	52.37	51.83	50.31
C	1.32	0.63	0.90	4.75	0.79	1.27	6.19	6.46	6.94	6.12
Total	97.48	96.27	108.23	109.62	101.07	102.35	116.62	118.50	118.23	116.12
MgO	23.81	26.24	30.21	28.07	27.48	26.18	29.38	28.01	27.79	31.76
Al_2O_3	5.00	5.64	5.37	5.10	4.38	2.76	5.51	8.13	8.14	6.27
SiO_2	41.24	46.17	45.43	45.83	46.27	47.87	48.25	44.16	43.83	39.83
CaO	9.33	9.31	9.57	9.79	9.84	11.56	10.17	8.63	8.61	6.56
FeO	10.46	7.12	7.46	8.01	8.55	9.32	8.07	11.17	11.19	13.55
MoO_3	4.13	3.51	2.65	3.73	3.50	2.73	3.13	4.49	4.58	5.06
Probe Carbon										
CO_2	4.83	2.30	3.31	17.40	2.88	4.64	22.69	23.65	25.43	22.42
Total	98.80	100.29	104.01	117.94	102.89	105.07	127.19	128.24	129.57	125.46
By Difference										
CO_2	6.03	2.01	0.00	0.00	0.00	0.00	0.00	0.00	0.00	0.00
Total	100.00	100.00	100.69	100.54	100.01	100.43	104.50	104.58	104.14	103.04

Table B-5. Average electron microprobe values and resultant oxides values including the wt% CO_2 determined from the microprobe values and the amount when calculated by difference for carbonated experiments DG-5-17.

Sample	DG-5-17*										
Date/Coat	11-6 Au4	12-4/5 Au1	12-4/5 Au2a	12-4/5 Au2b	12-4/5 Au4	12-4/5 Au5a	12-4/5 Au5b	12-4/5 Au6	12-4/5 Au7	12-4/5 Au8	12-4/5 Au9
Accel. Volt. (KeV)	15	12	10	10	10	10	10	10	10	10	10
Current (nA)	25	20	20	20	20	40	40	60	80	100	80
Probe Dia. (µm)	20	10	20	20	50	50	50	50	50	50	50
C Std	Dol	Dol	Dol	Cal	Dol	Dol	Dol	Dol	Dol	Dol	Dol
Peak/Back (s)	30/10										10/5
# of Analyses	4	2	2	2	2	2	2	2	2	2	2
Meas. Elm %											
Mg	14.61	17.32	18.18	18.25	18.36	17.83	17.82	17.80	18.18	18.25	18.25
Al	4.30	4.57	4.78	4.76	4.72	4.79	4.81	4.82	4.49	4.47	4.51
Si	19.60	21.53	22.44	22.76	22.31	22.50	22.79	22.53	22.38	22.49	22.39
Ca	6.32	6.72	6.70	6.67	6.73	7.00	6.98	6.91	6.62	6.61	6.62
Fe	8.63	9.04	9.16	8.91	9.47	9.22	9.26	9.26	9.19	9.16	9.16
Mo	7.01	4.22	4.09	4.07	4.36	4.74	4.78	4.83	5.39	5.35	5.31
O	49.36	58.85	62.14	62.68	61.25	59.89	59.10	60.59	59.51	60.44	60.60
C	2.96	4.32	4.57	6.90	4.86	3.94	4.02	5.41	3.73	4.41	5.02
Total	112.78	126.56	132.05	134.99	132.04	129.89	129.55	132.13	129.48	131.16	131.84
MgO	24.23	28.72	30.15	30.26	30.44	29.56	29.55	29.51	30.15	30.26	30.26
Al_2O_3	8.12	8.63	9.03	8.98	8.91	9.05	9.09	9.11	8.47	8.44	8.51
SiO_2	41.94	46.06	48.01	48.69	47.73	48.14	48.74	48.20	47.88	48.11	47.90
CaO	8.84	9.40	9.37	9.33	9.41	9.79	9.77	9.66	9.26	9.25	9.26
FeO	11.10	11.63	11.78	11.46	12.18	11.86	11.91	11.91	11.82	11.78	11.78
MoO_3	10.51	6.33	6.14	6.10	6.53	7.10	7.16	7.24	8.09	8.03	7.97
Probe Carbon											
CO_2	10.85	15.81	16.73	25.28	17.79	14.44	14.73	19.80	13.65	16.14	18.38
Total	115.58	126.58	131.20	140.11	132.99	129.93	130.96	135.43	129.31	132.00	134.05
By Difference											
CO_2	0.00	0.00	0.00	0.00	0.00	0.00	0.00	0.00	0.00	0.00	0.00
Total	104.73	110.77	114.47	114.83	115.20	115.50	116.23	115.63	115.66	115.86	115.67

Table B-6. Average electron microprobe values and resultant oxides values including the wt% CO_2 determined from the microprobe values and the amount when calculated by difference for carbonated experiments DG-5-22, 23.

Sample	DG-5-22			DG-5-23		
Date/Coat	3-26 Au1	3-26 Au2	3-26 Au3	4-16 Au1	4-16 Au2	4-16 Au3
Accel. Volt. (KeV)	15	10	10	15	10	10
Current (nA)	25	40	80	25	80	60
Probe Dia. (µm)	20	50	50	20	50	50
C Std	Dol	Dol	Dol	Dol	Dol	Dol
Peak/Back (s)	20/10	20/10	20/10	20/10	20/10	20/10
# of Analyses	8	3	3	5	3	3
Meas. Elm %						
Mg	16.91	17.72	17.68	17.03	18.27	18.37
Al	2.78	2.63	2.59	3.35	3.58	3.66
Si	21.00	21.86	21.82	20.89	22.38	22.17
Ca	6.91	7.10	7.03	6.98	6.92	6.77
Fe	7.22	7.62	7.60	6.89	7.39	7.16
Mo	2.00	2.18	2.12	2.64	2.57	2.57
O	47.86	49.72	50.12	50.24	53.15	53.43
C	4.18	3.91	4.36	2.69	3.14	3.75
Total	108.84	112.74	113.34	110.71	117.39	117.87
MgO	28.03	29.38	29.32	28.25	30.30	30.46
Al_2O_3	5.25	4.96	4.90	6.33	6.76	6.91
SiO_2	44.92	46.76	46.69	44.69	47.87	47.42
CaO	9.66	9.94	9.84	9.76	9.68	9.47
FeO	9.28	9.81	9.78	8.86	9.51	9.21
MoO_3	3.00	3.28	3.19	3.96	3.86	3.85
Probe Carbon						
CO_2	15.30	14.31	15.98	9.87	11.49	13.75
Total	115.45	118.44	119.69	111.72	119.47	121.08
By Difference						
CO_2	0.00	0.00	0.00	0.00	0.00	0.00
Total	100.15	104.13	103.72	101.85	107.97	107.32

Table B-7. Average electron microprobe values and resultant oxides values including the wt% CO_2 determined from the microprobe values and the amount when calculated by difference for non-carbonated experiments DG-N-3, 7, 9, 13, 14.

Sample	DG-N-3			DG-N-7			DG-N-9			DG-N-13	DG-N-14
Date/Coat	?	9-5 Ag1	9-5 Ag3	?	9-5 Ag1	9-5 Ag3	2-27 Ag	8-27 Au	3-25 Au1	8-27 Au	8-27 Au
Accel. Volt. (KeV)		12	12		12	12	15	15	15	15	15
Current (nA)		20	20		20	20	25	25	25	25	25
Probe Dia. (µm)		20	20		20	20	20	20	20	20	20
C Std		SiC			SiC		SiC	SiC	Dol	SiC	SiC
Peak/Back (s)									20/10		
# of Analyses	10	10	5	7	10	5	23	2	6	7	6
Meas. Elm %											
Mg	15.45	17.95	17.93	15.24	17.55	17.42	16.28	18.39	15.61	17.32	17.33
Al	3.88	4.27	4.45	3.99	4.05	4.20	2.81	1.94	2.70	2.08	3.83
Si	18.95	21.69	21.47	18.89	21.66	21.67	21.52	21.90	20.39	23.64	19.64
Ca	5.50	3.60	3.60	5.58	3.37	3.40	3.94	3.14	3.75	4.11	3.64
Fe	9.12	9.03	9.47	8.80	7.21	6.84	9.46	7.59	8.78	8.72	9.66
Mo	2.63	1.97	1.66	3.76	3.29	3.49	2.42	3.06	2.27	0.47	3.38
O	41.74	51.94	51.28	41.65	48.46	47.98	43.39	48.48	41.70	52.34	50.79
C	1.25	1.10	na	1.05	0.88	na	0.60	0.97	5.36	1.17	1.08
Total	98.51	111.56	109.87	98.97	106.47	105.00	100.42	105.45	100.54	109.84	109.34
MgO	25.63	29.77	29.73	25.27	29.11	28.89	27.00	30.49	25.88	28.72	28.73
Al_2O_3	7.33	8.06	8.42	7.54	7.66	7.94	5.31	3.66	5.09	3.92	7.24
SiO_2	40.53	46.41	45.94	40.40	46.34	46.36	46.03	46.85	43.62	50.58	42.02
CaO	7.69	5.04	5.03	7.81	4.71	4.76	5.52	4.39	5.24	5.74	5.09
FeO	11.73	11.62	12.19	11.32	9.27	8.80	12.17	9.76	11.29	11.22	12.42
MoO_3	3.94	2.95	2.49	5.64	4.93	5.24	3.63	4.58	3.40	0.71	5.06
Probe Carbon											
CO_2	4.58	4.04	0.00	3.86	3.22	0.00	2.20	3.55	19.63	4.28	3.94
Total	101.42	107.89	103.79	101.85	105.24	101.98	101.86	103.28	114.16	105.18	104.52
By Difference											
CO_2	3.16	0.00	0.00	2.01	0.00	0.00	0.35	0.27	5.47	0.00	0.00
Total	100.00	103.84	103.79	100.00	102.02	101.98	100.00	100.00	100.00	100.90	100.57

Table B-8. Average electron microprobe values and resultant oxides values including the wt% CO_2 determined from the microprobe values and the amount when calculated by difference for non-carbonated experiments DG-N-17, 19, 21, 24, 25, 31, 33.

Sample	DG-N-17		DG-N-19	DG-N-21		DG-N-24	DG-N-25	DG-N-31			DG-N-33
Date/Coat	11-6 Au4	3-25 Au1	8-27 Au	11-6 Au1	11-6 Au2	11-6 Au4	3-25 Au1	3-25 Au1	3-26 Au2	3-26 Au3	4-16 Au1
Accel. Volt. (KeV)	15	15	15	15	15	15	15	15	10	10	15
Current (nA)	25	25	25	25	25	25	25	25	40	80	25
Probe Dia. (µm)	20	20	20	20	20	20	20	20	50	50	20
C Std	Dol	Dol	SiC	Dol	Dol	Dol	Dol	Dol	Dol	Dol	Dol
Peak/Back (s)	30/10	20/10		30/10	15/10	30/10	20/10	20/10	20/10	20/10	20/10
# of Analyses	3	8	5	4	1	1	7	9	3	3	5
Meas. Elm %											
Mg	18.97	17.57	16.63	16.69	16.47	18.02	16.16	17.87	20.35	20.19	17.83
Al	3.83	3.96	3.92	2.57	3.41	2.80	3.02	2.79	2.56	2.51	3.17
Si	21.79	20.57	20.19	19.95	20.89	23.98	20.47	22.45	26.31	26.11	22.20
Ca	3.15	3.02	3.53	2.75	4.13	4.74	4.05	4.81	3.66	3.72	3.88
Fe	7.26	6.87	9.06	7.12	9.27	8.35	8.68	9.76	8.37	8.48	7.87
Mo	4.17	3.17	3.66	15.13	3.86	0.40	2.59	2.00	1.55	1.53	2.06
O	55.82	50.38	47.66	50.69	48.09	53.40	50.95	50.73	57.82	58.22	55.86
C	3.31	5.05	1.21	3.91	3.46	6.12	5.91	2.91	3.08	3.45	1.61
Total	118.30	110.60	105.85	118.81	109.58	117.81	111.82	113.31	123.70	124.21	114.47
MgO	31.46	29.14	27.58	27.68	27.31	29.88	26.79	29.63	33.75	33.48	29.56
Al_2O_3	7.23	7.49	7.41	4.86	6.44	5.29	5.71	5.27	4.84	4.74	5.99
SiO_2	46.61	44.00	43.18	42.68	44.69	51.30	43.79	48.04	56.29	55.85	47.50
CaO	4.41	4.22	4.93	3.85	5.78	6.63	5.67	6.73	5.12	5.21	5.43
FeO	9.34	8.84	11.66	9.16	11.93	10.74	11.16	12.55	10.77	10.91	10.13
MoO_3	6.26	4.76	5.49	22.70	5.79	0.61	3.88	3.00	2.32	2.30	3.08
Probe Carbon											
CO_2	12.14	18.52	4.42	14.33	12.68	22.42	21.67	10.66	11.29	12.65	5.91
Total	117.45	116.97	104.67	125.25	114.62	126.88	118.67	115.87	124.37	125.14	107.59
By Difference											
CO_2	0.00	1.55	0.00	0.00	0.00	0.00	3.00	0.00	0.00	0.00	0.00
Total	105.30	100.00	100.25	110.92	101.94	104.45	100.00	105.21	113.09	112.49	101.68

Table B-9. Average electron microprobe values and resultant oxides values including the wt% CO_2 determined from the microprobe values and the amount when calculated by difference for non-carbonated experiment DG-N-22.

Sample	DG-N-22						
Date/Coat	11-6 Au1	11-6 Au2	11-6 Au3	3-25 Au1	4-16 Au1	4-16 Au2	4-16 Au3
Accel. Volt. (KeV)	15	15	15	15	15	10	10
Current (nA)	25	25	25	25	25	80	60
Probe Dia. (µm)	20	20	20	20	20	50	50
C Std	Dol	Dol	Dol	Dol	Dol	Dol	Dol
Peak/Back (s)	30/10	15/10	10/5	20/10	20/10	20/10	20/10
# of Analyses	5	2	1	7	5	3	3
Meas. Elm %							
Mg	13.33	12.93	12.73	16.11	18.83	19.56	19.53
Al	2.82	2.81	2.44	3.72	4.08	4.63	4.52
Si	14.52	13.84	13.37	19.11	22.09	23.64	23.83
Ca	1.64	1.54	1.43	3.14	3.36	3.80	3.71
Fe	2.60	2.37	2.23	9.02	8.85	9.40	9.12
Mo	2.66	2.91	2.77	3.22	3.06	3.37	3.71
O	54.59	55.55	55.64	42.41	56.53	61.43	62.17
C	3.28	5.11	6.58	5.16	2.07	3.01	2.94
Total	95.44	97.04	97.19	101.89	118.88	128.84	129.52
MgO	22.10	21.44	21.11	26.71	31.23	32.44	32.39
Al_2O_3	5.33	5.31	4.61	7.04	7.70	8.74	8.53
SiO_2	31.07	29.60	28.60	40.89	47.27	50.57	50.98
CaO	2.29	2.15	2.00	4.39	4.70	5.32	5.19
FeO	3.34	3.05	2.87	11.60	11.39	12.10	11.73
MoO_3	3.99	4.36	4.16	4.84	4.60	5.06	5.57
Probe Carbon							
CO_2	12.02	18.72	24.11	18.90	7.58	11.02	10.76
Total	80.15	84.63	87.46	114.36	114.46	125.25	125.16
By Difference							
CO_2	31.87	34.10	36.65	4.54	0.00	0.00	0.00
Total	100.00	100.00	100.00	100.00	106.88	114.23	114.39

Table B-10. Average electron microprobe values and resultant oxides values including the wt% CO_2 determined from the microprobe values and the amount when calculated by difference for non-carbonated experiment DG-N-22.

Sample	DG-N-22 continued									
Date/Coat	12-4/5 Au1	12-4/5 Au2a	12-4/5 Au2b	12-4/5 Au4	12-4/5 Au5a	12-4/5 Au5b	12-4/5 Au6	12-4/5 Au7	12-4/5 Au8	12-4/5 Au9
Accel. Volt. (KeV)	12	10	10	10	10	10	10	10	10	10
Current (nA)	20	20	20	20	40	40	60	80	100	80
Probe Dia. (µm)	10	20	20	50	50	50	50	50	50	50
C Std	Dol	Dol	Cal	Dol	Dol	Dol	Dol	Dol	Dol	Dol
Peak/Back (s)										10/5
# of Analyses	2	2	2	2	2	2	2	2	2	2
Meas. Elm %										
Mg	16.13	16.03	16.14	16.24	16.95	16.98	16.94	16.64	16.66	16.71
Al	3.89	4.13	4.20	4.06	3.74	3.78	3.76	3.99	4.00	4.03
Si	21.04	20.70	20.86	20.30	20.59	20.81	20.73	20.81	20.82	20.80
Ca	3.68	3.45	3.44	3.39	3.25	3.23	3.19	3.39	3.45	3.45
Fe	8.46	8.98	9.02	9.30	9.61	9.64	9.51	9.25	9.15	9.27
Mo	2.71	2.84	2.78	2.84	2.80	2.79	2.90	2.87	2.78	2.77
O	46.41	46.61	47.10	45.68	44.44	42.99	45.17	43.42	44.58	44.82
C	5.01	5.69	7.81	6.49	5.69	5.31	6.60	5.52	5.93	6.32
Total	107.31	108.40	111.32	108.27	107.05	105.52	108.78	105.87	107.34	108.16
MgO	26.75	26.57	26.76	26.92	28.11	28.16	28.09	27.59	27.62	27.71
Al_2O_3	7.34	7.79	7.93	7.66	7.06	7.14	7.09	7.53	7.55	7.61
SiO_2	45.01	44.27	44.62	43.42	44.04	44.52	44.35	44.51	44.53	44.50
CaO	5.15	4.82	4.81	4.74	4.55	4.51	4.46	4.74	4.82	4.83
FeO	10.88	11.55	11.60	11.96	12.36	12.40	12.23	11.90	11.76	11.92
MoO_3	4.06	4.26	4.16	4.25	4.20	4.18	4.34	4.31	4.17	4.15
Probe Carbon										
CO_2	18.34	20.85	28.60	23.78	20.83	19.44	24.16	20.21	21.71	23.16
Total	117.53	120.12	128.47	122.73	121.14	120.35	124.74	120.78	122.16	123.86
By Difference										
CO_2	0.81	0.73	0.13	1.05	0.00	0.00	0.00	0.00	0.00	0.00
Total	100.00	100.00	100.00	100.00	100.31	100.91	100.57	100.57	100.45	100.71

As stated previously, our samples contained metastable quench crystals which complicate analysis. To avoid these, we created a carbonated "andesite" (And-5, Table B-11) using the same materials used to create the synthetic komatiite mixes. Because of the much higher Si and Al contents and lower Mg# of the andesite, this mix quenched to a glass, much preferred in analysis. We placed the andesite mix in a Mo capsule, without any mineral spheres, and melted it in the multi-anvil at 1900°C and 4.0 GPa for 60 seconds. The experiment was ground using kerosene and alcohol, coated with Au, and then analyzed with the electron microprobe using various operating conditions (Table B-12). The amount of C detected in the andesite (~4.5 wt% C) was similar to that detected in the experimental melts (~5.7 wt% C), indicating that the problem of detecting C is most likely not the presence of quench crystals.

Table B-11. Starting composition for carbonated "andesite" mix.

Oxide	And-5
SiO_2	59.50
Al_2O_3	18.17
FeO	7.11
MgO	3.56
CaO	6.53
CO_2	5.13
Total	100.00
Mg#	47.13

Table B-12. Average electron microprobe values and resultant oxides values including the wt% CO_2 determined from the microprobe values and the amount when calculated by difference for carbonated experiment And-5.

Sample	And-5-1*		
Date/Coat	1-22 Au1	1-22 Au2	1-22 Au3
Accel. Volt. (KeV)	12	12	12
Current (nA)	20	40	10
Probe Dia. (µm)	50	50	10
C Std	Dol	Dol	Dol
Peak/Back (s)	10/5	10/5	20/10
# of Analyses	4	4	4
Meas. Elm %			
Mg	2.20	2.21	2.20
Al	10.98	10.95	10.98
Si	28.56	28.90	27.96
Ca	5.92	5.92	6.03
Fe	5.86	5.95	6.03
Mo	1.41	1.43	1.44
O	54.51	54.54	54.84
C	4.46	5.11	3.89
Total	113.89	115.00	113.36
MgO	3.64	3.66	3.65
Al_2O_3	20.75	20.68	20.75
SiO_2	61.10	61.83	59.81
CaO	8.28	8.29	8.44
FeO	7.53	7.65	7.75
MoO_3	2.12	2.15	2.16
Probe Carbon			
CO_2	16.33	18.71	14.24
Total	119.76	122.98	116.79
By Difference			
CO_2	0.00	0.00	0.00
Total	103.42	104.26	102.54

In an effort to accurately determine the amount of CO_2 present in these experiments with the electron microprobe, we used the conventional method of "by difference." Any deficit from an analytical total of 100 is assumed to indicate the presence of a volatile, in this case CO_2. Carbonated and non-carbonated experiments were carbon-coated and analyzed with the microprobe using an accelerating voltage of 15 kV, a current of 2.5×10^{-8} A, and a beam diameter of 20 μm. The standards used were almandine for Si, Al, and Fe; diopside for Ca and Mg; and $CaMoO_4$ for Mo; oxygen was calculated by stoichiometry. The totals were all close to 100 wt% (98-102 wt%) for the non-carbonated experiments (Table B-13) indicating that any carbon previously detected by the microprobe is erroneous. The totals of the carbonated experiments (Table B-14) were also close to 100 wt% except for DG-5-9 (98.81 wt%) and DG-5-19 (97.90 wt%). This may indicate that the carbon detected for the carbonated experiments is also wrong. Since two experiments did have deficits reinforces the idea that CO_2 is present in the melt during the run but escapes after the run is completed. Unfortunately, there is no way of knowing the amount of CO_2 present during the run, which directly affects the calculation of $\overline{V}_{CO_2}$.

Table B-13. Average electron microprobe oxide values including the wt% CO_2 calculated by difference for C-coated carbonated experiments DG-5-9, 14, 16, 19, 21, 22, 23.

Sample	DG-5-9	DG-5-14	DG-5-16	DG-5-19	DG-5-21	DG-5-22	DG-5-23
Date/Coat	6-17 C	6-17 C	6-17 C	6-17 C	6-17 C	6-17 C	6-17 C
Accel. Volt. (KeV)	15	15	15	15	15	15	15
Current (nA)	25	25	25	25	25	25	25
Probe Dia. (µm)	20	20	20	20	20	20	20
# of Analyses	10	10	10	9	10	10	10
Meas. Ox%							
MgO	27.09	30.25	29.03	27.92	28.03	29.68	29.31
Al_2O_3	7.72	4.69	4.45	7.12	6.89	5.32	6.18
SiO_2	42.38	45.64	45.19	41.72	43.53	44.55	44.04
CaO	8.16	9.24	9.65	7.92	8.74	8.51	8.63
FeO	10.41	7.45	8.89	9.90	7.90	8.79	8.50
MoO_3	3.06	3.70	3.37	3.32	5.47	3.22	3.94
By Difference							
CO_2	1.19	0.00	0.00	2.10	0.00	0.00	0.00
Total	100.00	100.98	100.58	100.00	100.56	100.07	100.60

Table B-14. Average electron microprobe oxide values including the wt% CO_2 calculated by difference for C-coated non-carbonated experiments DG-N-7, 14, 20, 22, 23.

Sample	DG-N-7	DG-N-14	DG-N-20	DG-N-22	DG-N-23
Date/Coat	6-17 C	6-17 C	6-17 C	6-17 C	6-17 C
Accel. Volt. (KeV)	15	15	15	15	15
Current (nA)	25	25	25	25	25
Probe Dia. (µm)	20	20	20	20	20
# of Analyses	10	10	10	10	10
Meas. Ox%					
MgO	28.26	30.31	29.36	28.61	29.40
Al_2O_3	7.58	6.63	7.66	7.25	7.34
SiO_2	46.71	43.36	45.26	44.19	43.95
CaO	4.79	4.30	4.94	4.69	4.49
FeO	9.09	11.61	9.71	11.12	9.95
MoO_3	5.32	4.64	3.48	5.46	5.19
By Difference					
CO_2	0.00	0.00	0.00	0.00	0.00
Total	101.74	100.84	100.42	101.32	100.33

Appendix C

FTIR

Though we were not successful in detecting carbon in any form in our samples with FTIR, the conditions we used and our attempts are presented here. All analytical conditions are present in Table C-1 along with the amount of CO_3^{2-} calculated from composition to be in each sample.

Table C-1. Micro-FTIR analytical conditions with approximate amount of CO_3^{2-} present in sample.

Date	Sample	Scans	Res. (cm^{-1})	Spot size (µm)	CO_3^{2-} (wt%)
11/21/2008	DG-5-1	500	4	100	7.81
	DG-5-1	500	4	170	7.81
8/19/2009	Dolomite	500	4	100	59.32
	Calcite crystal	300	8	100	59.95
	Calcite powdered	300	8	100	59.95
	DG-5-9	300	8	170	7.81
	DG-N-3	300	8	170	0.00
	DG-5-7	50	8	transmission	7.81
8/28/2009	DG-5-4	300	8	170	7.81
	DG-5-11	300	8	170	7.81
	DG-N-7	300	8	170	0.00
2/4/2010	DG-5-17	300	8	100	7.81
	And-5	300	8	100	6.99
	MHA27	300	8	100	0.283
	MHA26	300	8	100	0.373
	MHA44	300	8	100	0.483
	Juli12	300	8	100	0.575

We began with carbonated experiment DG-5-1 using 500 scans with a resolution of 4 cm^{-1}, and a square spot size of 100 µm (Figures C-1, C-9, C-10). We later used a 170 µm spot because it gave a better average of the heterogeneous run product (Figures C-2, C-9, C-10). A single peak existed at approximately 1420 cm^{-1}, rather than a doublet. This is possible if CO_3^{2-} is in a lattice coordinated with a cation such as Ca, Mg, or Fe. To be sure of our peak, we also analyzed natural carbonated andesites which actually had

the carbonate doublet. Natural samples of dolomite and calcite, however, did have a single peak in same area (Figure C-3).

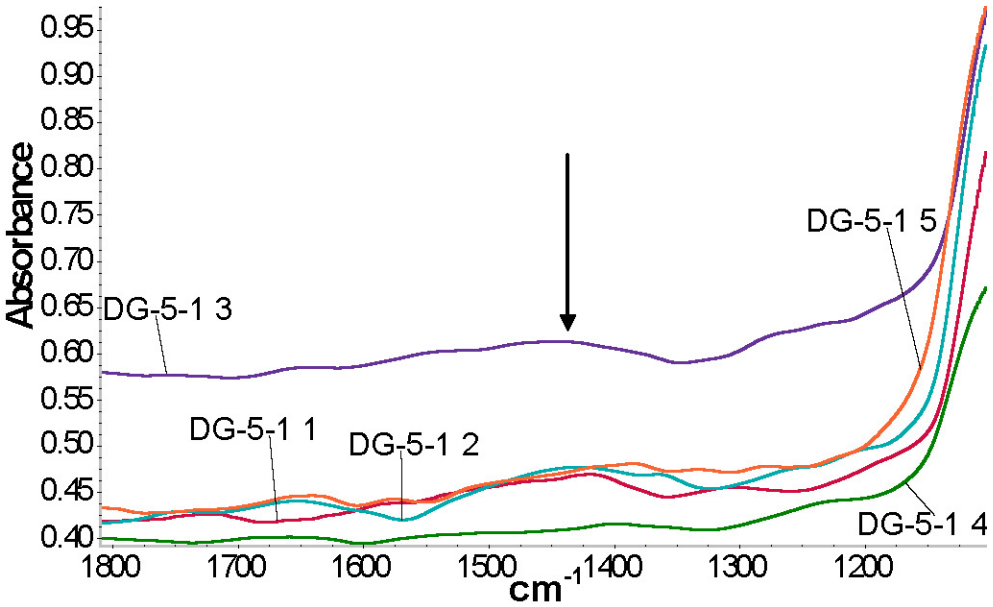

Figure C-1. Micro-FTIR analyses of carbonated experiment DG-5-1 using 100 µm spot size. Five different analyses from different spots on the sample are shown. For the location of each spot see Figure C-10. Arrow indicates potential carbonate peak.

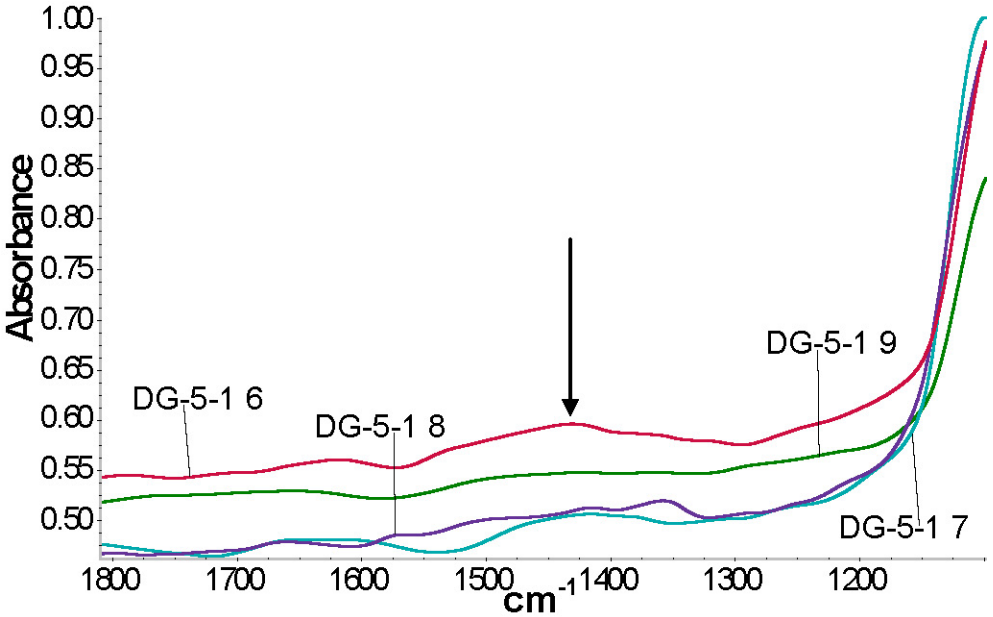

Figure C-2. Micro-FTIR analyses of carbonated experiment DG-5-1 using 170 µm spot size. Four different analyses from different spots on the sample are shown. For the location of each spot see Figure C-10. Arrow indicates potential carbonate peak.

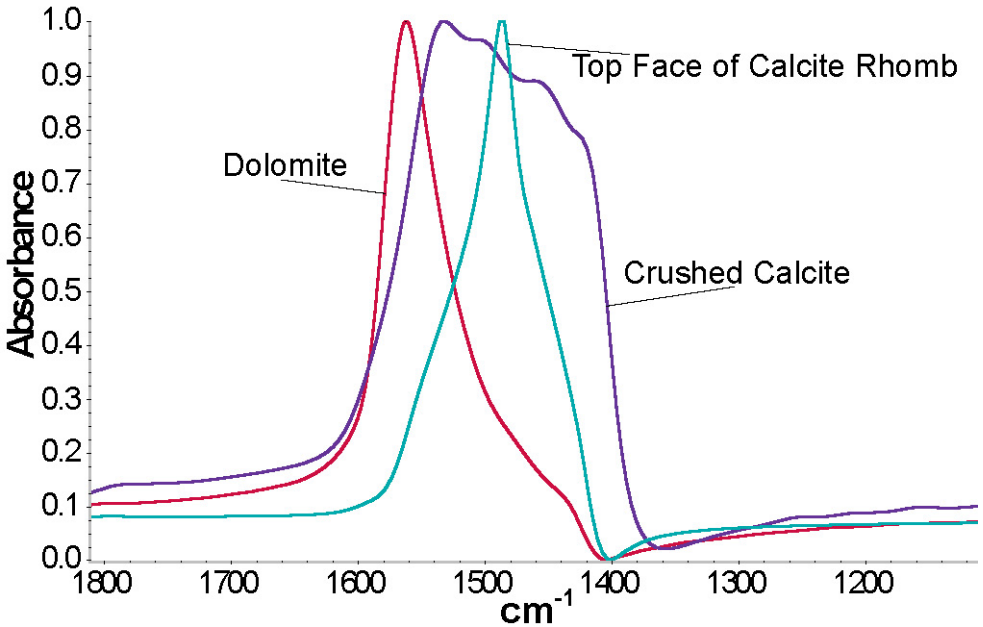

Figure C-3. Spectra were taken in micro-reflectance mode. Dolomite conditions were 500 scans, 4 cm resolution, 100 µm spot. Calcite crystal and pressed powder of the same crystal conditions were 300 scans, 8 cm^{-1} resolution, and 100 µm spot. The pressed powder was analyzed to test the effect of many different crystal orientations on the resultant peak position.

We then analyzed a non-carbonated experiment, DG-N-3, and found the same peak (Figures C-4, C-17, C-18). We then thought the peak was not in fact a carbonate signal but a Si overtone. To double check we then analyzed samples that had melted more, as experiment DG-5-1 had small amounts of unmelted alumina (see Figure C-9), and therefore had a smoother surface (DG-5-9, DG-5-11), and the peak all but disappeared (Figures C-5, C-13, C-14, C-15). To be sure, we ground one experiment using only kerosene and anhydrous alcohol to ensure that the water used for the other experiments was not dissolving any carbonate present (DG-5-17), but no carbonate peak was detected (Figures C-5, C-16). To ensure that the method we were using (reflectance) was not the cause of the undetectable carbonate, we used transmission on the bench on a carbonated sample, DG-5-7. In order to set up the sample for transmission, we used a SiC pick to powder the quenched melt, avoiding the Mo capsule and the mineral spheres.

The powder (0.128 mg) was then mixed with KBr (4.778 mg) and pressed into a disc and placed in the bench transmission beam. There was not an obvious carbonate peak present (Figure C-6). This method of plucking out the sample is not ideal due to the potential loss and/or contamination of the sample. We tried doubly polishing some samples and successfully got them to 120-360 µm thick, unfortunately this is not thin enough for the beam to pass through. In order to be thin enough, the required thickness of the sample would have to be ~80 µm or less. We did not test this because the presence of Mo blebs would still have distorted the beam.

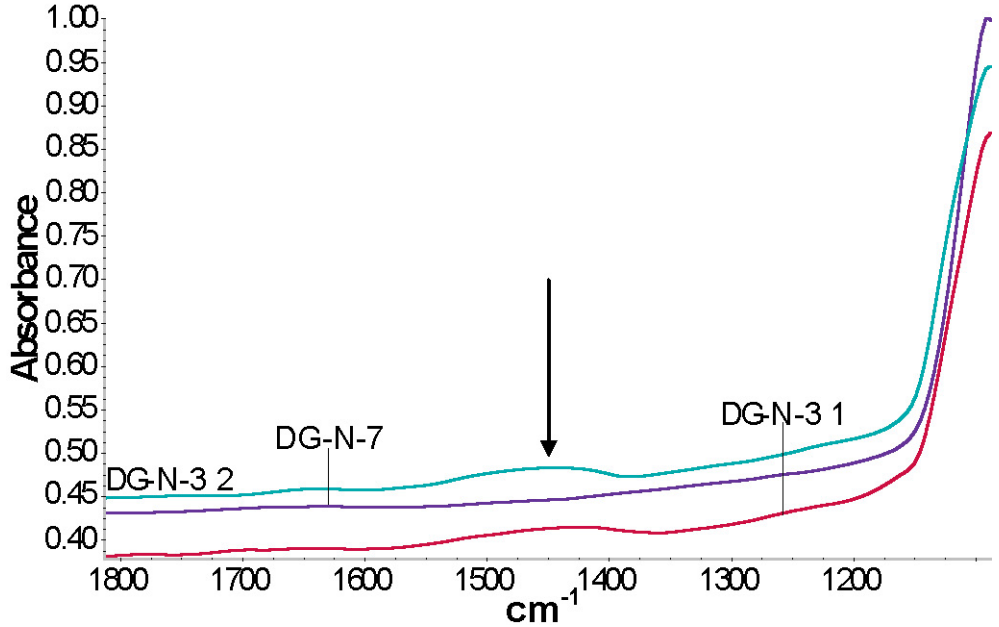

Figure C-4. Micro-FTIR analyses of non-carbonated experiments DG-N-3 and DG-N-7 using 300 scans, 8 cm^{-1} resolution, 170 µm spot size. Two different analyses from different spots on DG-N-3 and one spot from DG-N-7 are shown. For the location of each spot see Figures C-17 through C-20. Arrow indicates potential carbonate peak.

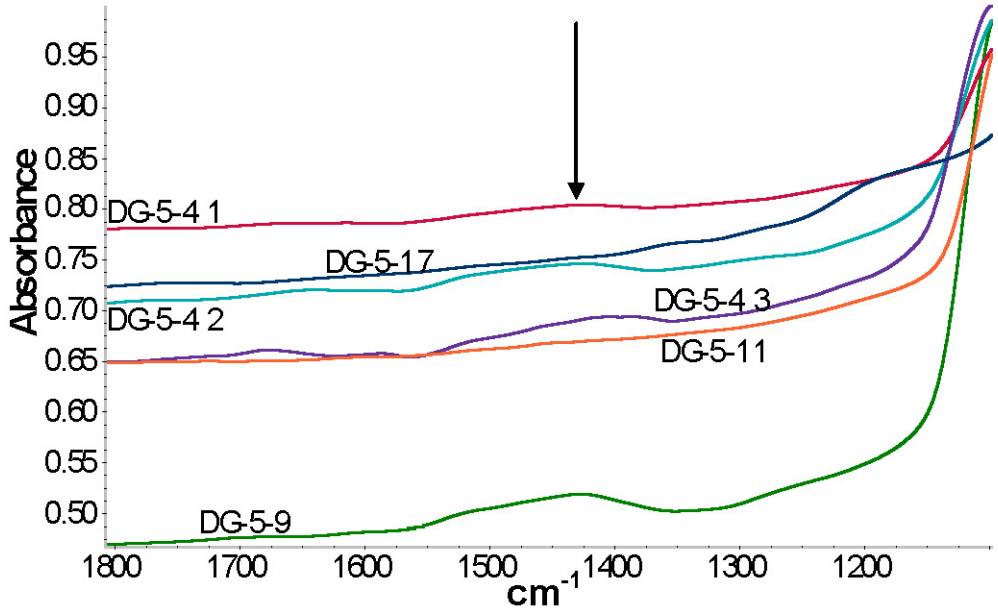

Figure C-5. Micro-FTIR analyses of carbonated experiments DG-5-4, DG-5-9, DG-5-11, and DG-5-17 using 300 scans, 8 cm^{-1} resolution, 170 µm spot size, 100 µm spot size for DG-5-17. Three different analyses from different spots on DG-5-4 and one spot from the other experiments are shown. For the location of each spot see Figures C-11 through C-16. Experiments DG-5-9, DG-5-11, and DG-5-17 had smoother surfaces, while DG-5-4 had a rougher surface. Notice that the "carbonate" peak is visible in all DG-5-4 analyses and in DG-5-9, but is not seen for DG-5-11 or DG-5-17.

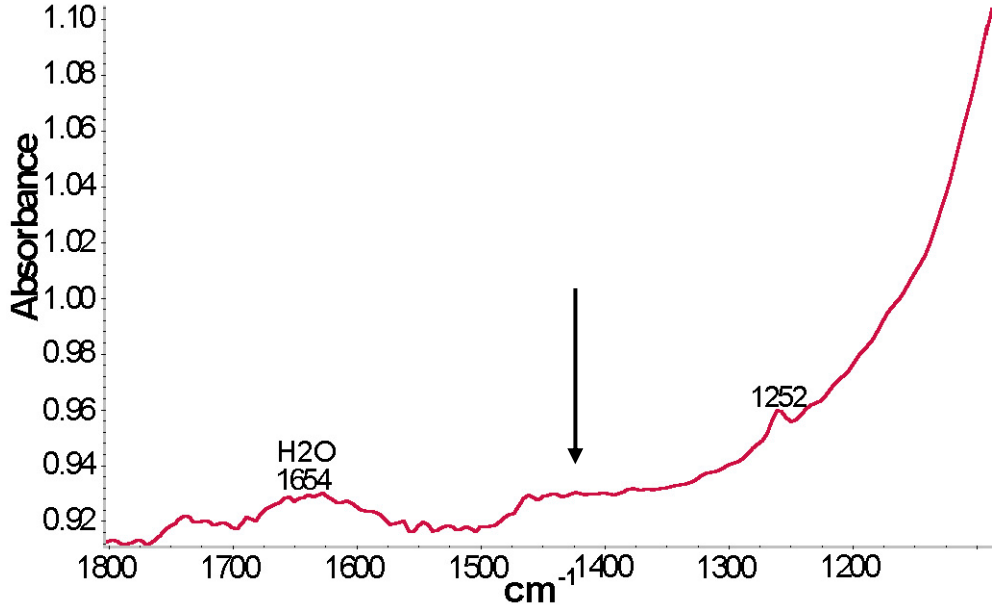

Figure C-6. Transmission results of powdered and pressed carbonated experiment DG-5-7, there was no obvious carbonate peak present.

We then placed the carbonated "andesite" glass (And-5) under the microscope (Figure C-21) to be analyzed in reflectance mode in case our inability to detect carbon

was due to sample heterogeneity or surface roughness due to the quench crystals. No carbonate peak was obvious (Figure C-7). In case the detection limit of CO_3^{2-} was too high, we analyzed some natural carbonated andesites with 0.283-0.575 wt% CO_3^{2-}. There were small but measurable carbonate peaks at 1430 and 1520 cm^{-1}, confirming a very low detection limit (Figure C-8).

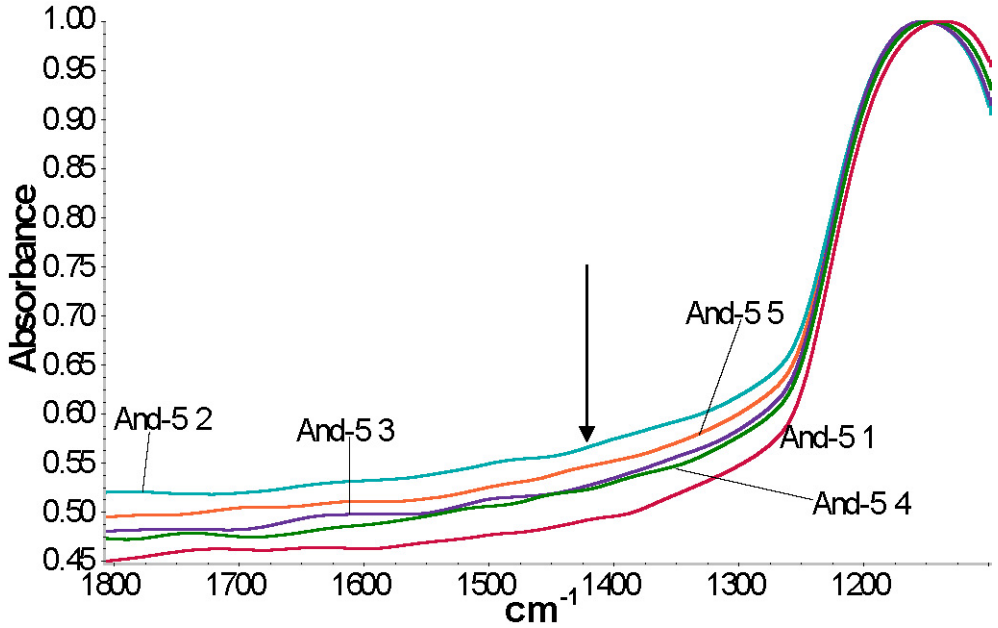

Figure C-7. Micro-FTIR analyses of carbonated experiment And-5 using 100 µm spot size. Five different analyses from different spots on the sample are shown. For the location of each spot see Figure C-21.

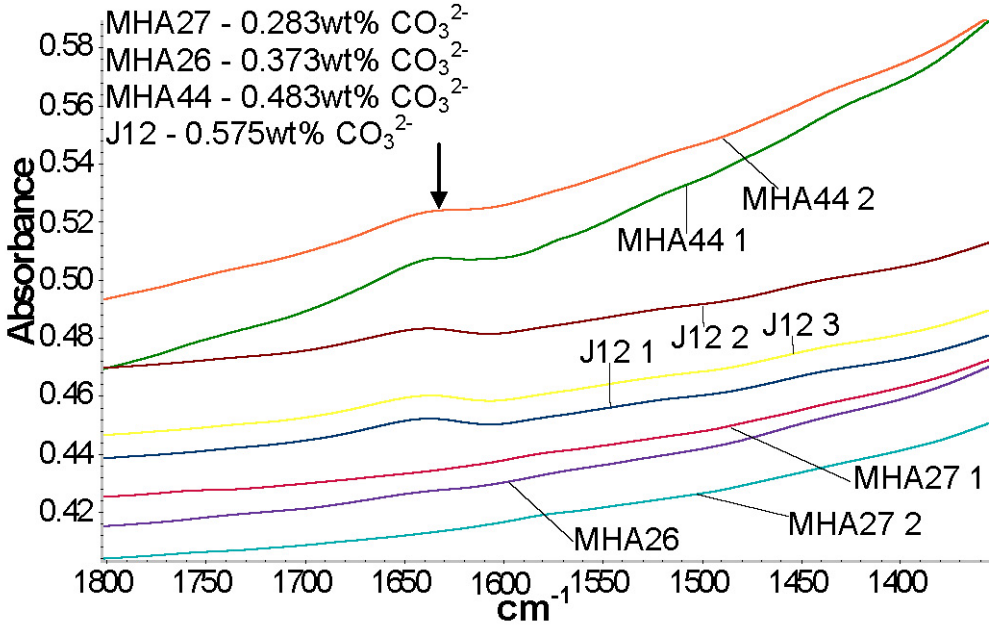

Figure C-8. Micro-FTIR analyses of carbonated natural andesites using 100 µm spot size. Four different andesites with varying carbonate contents are shown. Arrow indicates carbonate peak.

The following images show micro-FTIR analysis spots for experiments analyzed. The actual spot is shown for those available. The capsules are approximately 1100 µm across and 1400 µm tall, all images are arranged so the top of the capsule is at the top of the image, and the images of the analysis spot are roughly to scale and oriented with the capsule images.

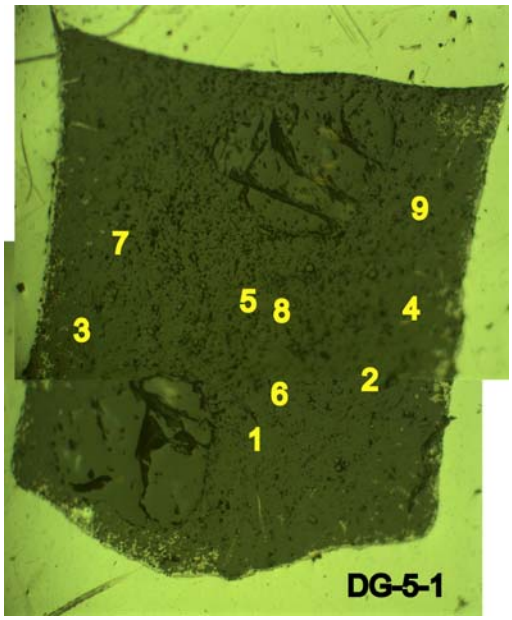

Figure C-9. Reflected light image of carbonated experiment DG-5-1, numbers indicate FTIR analysis spots.

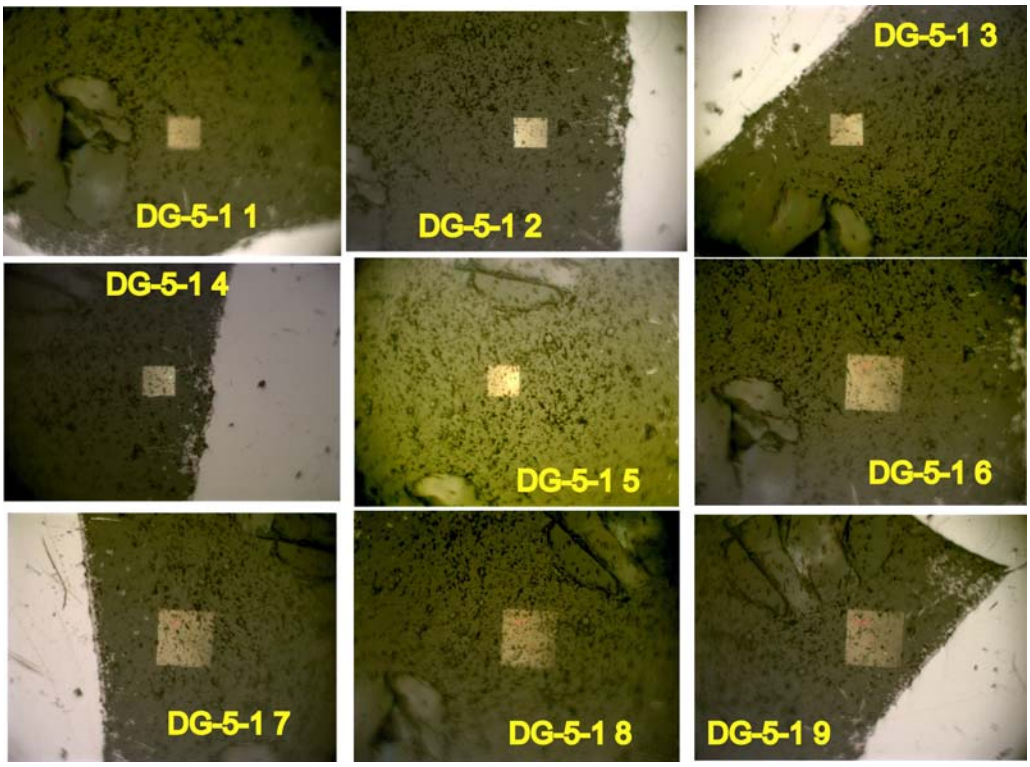

Figure C-10. Reflected light images of carbonated experiment DG-5-1 FTIR analysis spots. Spots 1 through 5 used 100 µm, 6 through 9 used 170 µm.

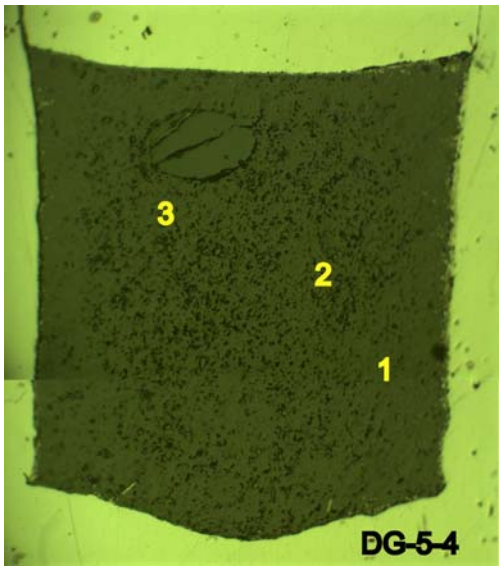

Figure C-11. Reflected light image of carbonated experiment DG-5-4, numbers indicate FTIR analysis spots.

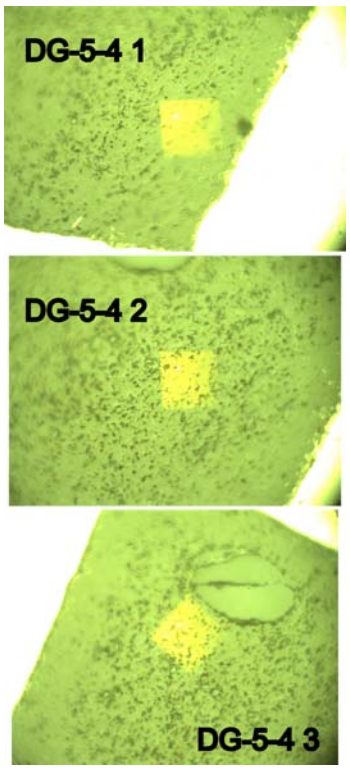

Figure C-12. Reflected light images of DG-5-4 FTIR analysis spots, 170 µm.

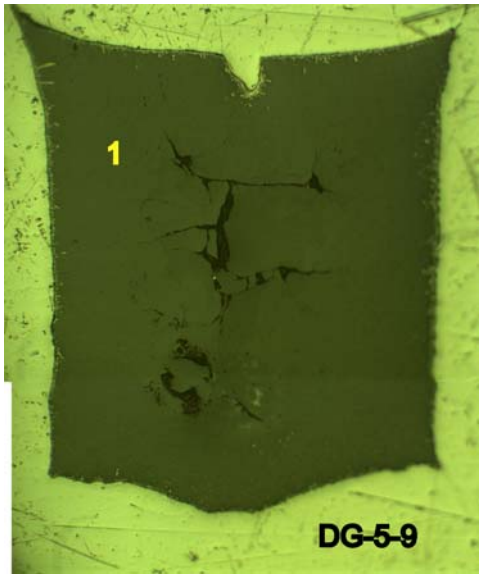

Figure C-13. Reflected light image of carbonated experiment DG-5-9, number indicates FTIR analysis spot.

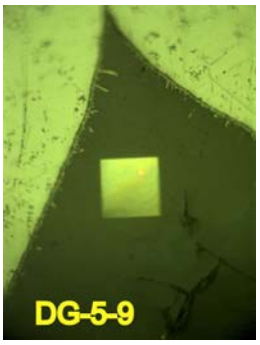

Figure C-14. Reflected light image of DG-5-9 FTIR analysis spot, 170 µm.

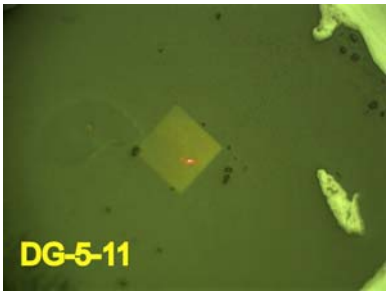

Figure C-15. Reflected light image of carbonated experiment DG-5-11 FTIR analysis spot, 170 µm.

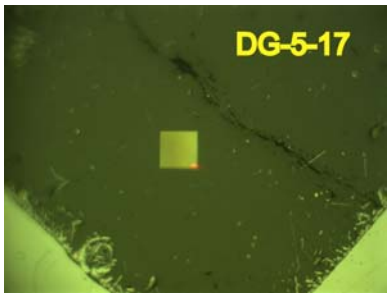

Figure C-16. Reflected light image of carbonated experiment DG-5-17 FTIR analysis spot, 100 µm.

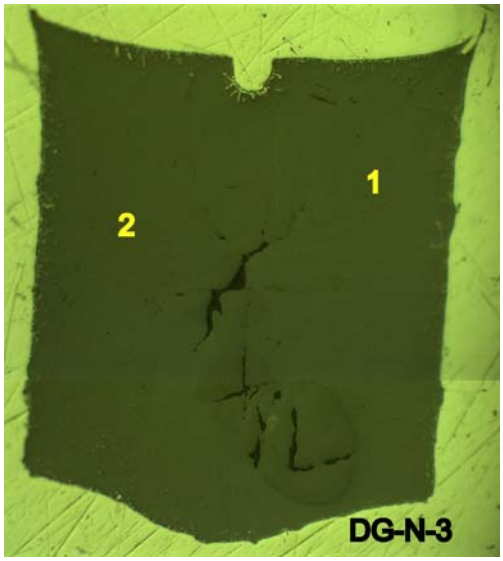

Figure C-17. Reflected light image of non-carbonated experiment DG-N-3, numbers indicate FTIR analysis spots.

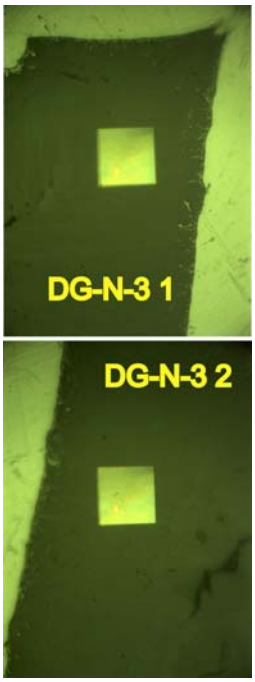

Figure C-18. Reflected light images of DG-N-3 FTIR analysis spots, 170 µm.

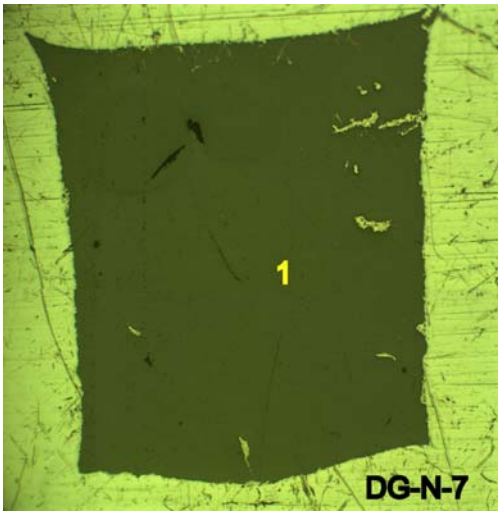

Figure C-19. Reflected light image of non-carbonated experiment DG-N-7, number indicates FTIR analysis spot.

Figure C-20. Reflected light image of DG-N-7 FTIR analysis spot, 170 µm.

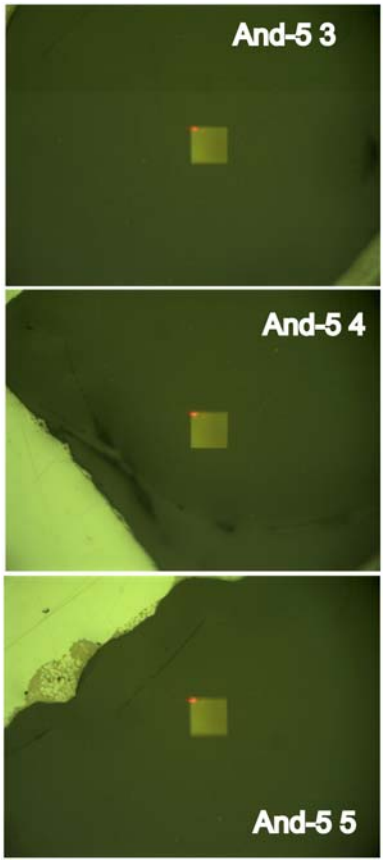

Figure C-21. Reflected light images of three And-5 FTIR analysis spots, 100 µm.

References

Agee, C. B. (2008a) Static compression of hydrous silicate melt and the effect of water on planetary differentiation. *Earth and Planetary Science Letters*. **265** (3-4): 641-654.

Agee, C. B. (2008b) Compressibility of water in magma and the prediction of density crossovers in mantle differentiation. *Philosophical Transactions of the Royal Society of London Series A-Mathematical Physical and Engineering Sciences*. **366** 4239-4252.

Agee, C. B. and D. Walker. (1988) Static compression and olivine flotation in ultrabasic silicate liquid. *Journal of Geophysical Research-Solid Earth and Planets*. **93** (B4): 3437-3449.

Agee, C. B. and D. Walker. (1993) Olivine flotation in mantle melt. *Earth and Planetary Science Letters*. **114** (2-3): 315-324.

Anderson, A. T. (1975) Some basaltic and andesitic glasses. *Reviews of Geophysics and Space Physics*. **13** (1): 37-55.

Bockris, J. O., J. W. Tomlinson and J. L. White. (1956) The structure of the liquid silicates - Partial molar volumes and expansivities. *Transactions of the Faraday Society*. **52** (3): 299-310.

Bond, W. L. (1951) Making small spheres. *Review of Scientific Instruments*. **22** (5): 344-345.

Bottinga, Y. and D. F. Weill. (1970) Densities of liquid silicate systems calculated from partial molar volumes of oxide components. *American Journal of Science*. **269** (2): 169-182.

Bourgue, E. and P. Richet. (2001) The effects of dissolved CO_2 on the density and viscosity of silicate melts: A preliminary study. *Earth and Planetary Science Letters*. **193** (1-2): 57-68.

Bowen, N. L. (1928) *The Evolution of the Igneous Rocks*. Princeton University Press, Princeton, pp. 332.

Brey, G. P., L. N. Kogarko and I. D. Ryabchikov. (1991) Carbon dioxide in kimberlitic melts. *Neues Jahrbuch Fur Mineralogie-Monatshefte*. (4): 159-168.

Brooker, R. A. (1998) The effect of CO_2 saturation on immiscibility between silicate and carbonate liquids: An experimental study. *Journal of Petrology*. **39** (11-12): 1905-1915.

Brooker, R. A., S. C. Kohn, J. R. Holloway and P. F. McMillan. (2001a) Structural controls on the solubility of CO_2 in silicate melts Part I: bulk solubility data. *Chemical Geology*. **174** (1-3): 225-239.

Brooker, R. A., S. C. Kohn, J. R. Holloway and P. F. McMillan. (2001b) Structural controls on the solubility of CO_2 in silicate melts Part II: IR characteristics of carbonate groups in silicate glasses. *Chemical Geology*. **174** (1-3): 241-254.

Canil, D. and C. M. Scarfe. (1990) Phase relations in peridotite + CO_2 systems to 12 GPa - Implications for the origin of kimberlite and carbonate stability in the Earth's upper mantle. *Journal of Geophysical Research-Solid Earth and Planets*. **95** (B10): 15805-15816.

Circone, S. and C. B. Agee. (1996) Compressibility of molten high-Ti mare glass: Evidence for crystal-liquid density inversions in the lunar mantle. *Geochimica et Cosmochimica Acta*. **60** (14): 2709-2720.

Dalton, J. A. and D. C. Presnall. (1998) Carbonatitic melts along the solidus of model lherzolite in the system CaO-MgO-Al_2O_3-SiO_2-CO_2 from 3 to 7 GPa. *Contributions to Mineralogy and Petrology*. **131** (2-3): 123-135.

Dasgupta, R. and M. M. Hirschmann. (2007) Effect of variable carbonate concentration on the solidus of mantle peridotite. *American Mineralogist*. **92** (2-3): 370-379.

Dasgupta, R. and D. Walker. (2008) Carbon solubility in core melts in a shallow magma ocean environment and distribution of carbon between the Earth's core and the mantle. *Geochimica et Cosmochimica Acta*. **72** (18): 4627-4641.

Dasgupta, R., M. M. Hirschmann and N. D. Smith. (2007) Partial melting experiments of peridotite CO_2 at 3 GPa and genesis of alkalic ocean island basalts. *Journal of Petrology*. **48** (11): 2093-2124.

Dixon, J. E. (1997) Degassing of alkalic basalts. *American Mineralogist*. **82** (3-4): 368-378.

Dixon, J. E. and V. Pan. (1995) Determination of the molar absorptivity of dissolved carbonate in basanitic glass. *American Mineralogist*. **80** (11-12): 1339-1342.

Dixon, J. E., E. M. Stolper and J. R. Holloway. (1995) An experimental study of water and carbon dioxide solubilities in mid ocean ridge basaltic liquids 1. Calibration and solubility models. *Journal of Petrology*. **36** (6): 1607-1631.

Dobson, D. P., A. P. Jones, R. Rabe, T. Sekine, K. Kurita, T. Taniguchi, T. Kondo, T. Kato, O. Shimomura and S. Urakawa. (1996) In-situ measurement of viscosity and density of carbonate melts at high pressure. *Earth and Planetary Science Letters*. **143** (1-4): 207-215.

Dziewonski, A. M. and D. L. Anderson. (1981) Preliminary Reference Earth Model. *Physics of the Earth and Planetary Interiors*. **25** (4): 297-356.

Eggler, D. H. (1978) Effect of CO_2 upon partial melting of peridotite in system Na_2O-CaO-Al_2O_3-MgO-SiO_2-CO_2 to 35 kb, with an analysis of melting in a peridotite-H_2O-CO_2 system. *American Journal of Science*. **278** (3): 305-343.

Eggler, D. H. and M. Rosenhauer. (1978) Carbon dioxide in silicate melts 2. Solubilities of CO_2 and H_2O in $CaMgSi_2O_6$ (diopside) liquids and vapors at pressures to 40 kb. *American Journal of Science*. **278** (1): 64-94.

Fine, G. and E. Stolper. (1985) The speciation of carbon dioxide in sodium aluminosilicate glasses. *Contributions to Mineralogy and Petrology*. **91** (2): 105-121.

Fine, G. and E. Stolper. (1986) Dissolved carbon dioxide in basaltic glasses - Concentrations and speciation. *Earth and Planetary Science Letters*. **76** (3-4): 263-278.

Genge, M. J., G. D. Price and A. P. Jones. (1995) Molecular dynamics simulations of $CaCO_3$ melts to mantle pressures and temperatures - Implications for carbonatite magmas. *Earth and Planetary Science Letters*. **131** (3-4): 225-238.

Ghosh, S., E. Ohtani, K. Litasov, A. Suzuki and T. Sakamaki. (2007) Stability of carbonated magmas at the base of the Earth's upper mantle. *Geophysical Research Letters*. **34** (22): doi:10.1029/2007GL031349.

Graham, E. K., J. A. Schwab, S. M. Sopkin and H. Takei. (1988) The pressure and temperature-dependence of the elastic properties of single-crystal fayalite Fe_2SiO_4. *Physics and Chemistry of Minerals*. **16** (2): 186-198.

Hazen, R. M. (1976) Effects of temperature and pressure on crystal structure of forsterite. *American Mineralogist*. **61** (11-1): 1280-1293.

Hazen, R. M. (1977) Effects of temperature and pressure on crystal structure of ferromagnesian olivine. *American Mineralogist*. **62** (3-4): 286-295.

Hirose, K. (1997) Partial melt compositions of carbonated peridotite at 3 GPa and role of CO_2 in alkali basalt magma generation. *Geophysical Research Letters*. **24** (22): 2837-2840.

Hushur, A., M. H. Manghnani, J. R. Smyth, F. Nestola and D. J. Frost. (2009) Crystal chemistry of hydrous forsterite and its vibrational properties up to 41 GPa. *American Mineralogist*. **94** 751-760.

Isaak, D. G., E. K. Graham, J. D. Bass and H. Wang. (1993) The elastic properties of single-crystal fayalite as determined by dynamical measurement techniques. *Pure and Applied Geophysics*. **141** 393-414.

Jacobs, M. H. G. and B. H. W. S. de Jong. (2007) Placing constraints on phase equilibria and thermophysical properties in the system MgO-SiO_2 by a thermodynamically consistent vibrational method. *Geochimica Et Cosmochimica Acta*. **71** (14): 3630-3655.

Kajiyoshi, K. (1986) *High temperature equation of state for mantle minerals and their anharmonic properties*. M.S. Thesis, Okayama Univ., Okayama, Japan. pp. 30.

King, P. L. and J. R. Holloway. (2002) CO_2 solubility and speciation in intermediate (andesitic) melts: The role of H_2O and composition. *Geochimica et Cosmochimica Acta*. **66** (9): 1627-1640.

Kopylova, M. G., S. Matveev and M. Raudsepp. (2007) Searching for parental kimberlite melt. *Geochimica et Cosmochimica Acta*. **71** (14): 3616-3629.

Kumazawa, M. and O. L. Anderson. (1969) Elastic moduli, pressure derivatives, and temperature derivatives of single crystal olivine and single crystal forsterite. *Journal of Geophysical Research*. **74** (25): 5961-5972.

Kuramoto, K. (1997) Accretion, core formation, H and C evolution of the Earth and Mars. *Physics of the Earth and Planetary Interiors*. **100** (1-4): 3-20.

Lange, R. A. (1994) The effects of H_2O, CO_2 and F on the density and viscosity of silicate melts. *Reviews in Mineralogy*. **30** 331-369.

Lange, R. A. and I. S. E. Carmichael. (1987) Densities of Na_2O-K_2O-CaO-MgO-FeO-Fe_2O_3-Al_2O_3-TiO_2-SiO_2 liquids - New measurements and derived partial molar properties. *Geochimica et Cosmochimica Acta*. **51** (11): 2931-2946.

Lange, R. L. and I. S. E. Carmichael. (1990) Thermodynamic properties of silicate liquids with emphasis on density, thermal expansion, and compressibility. *Reviews in Mineralogy*. **24** 25-64.

Liu, Q. and R. A. Lange. (2003) New density measurements on carbonate liquids and the partial molar volume of the $CaCO_3$ component. *Contributions to Mineralogy and Petrology*. **146** (3): 370-381.

Liu, W. and B. S. Li. (2006) Thermal equation of state of $(Mg_{0.9}Fe_{0.1})_2SiO_4$ olivine. *Physics of the Earth and Planetary Interiors*. **157** (3-4): 188-195.

Matsui, T. and M. H. Manghnani. (1985) Thermal expanison of single-crystal forsterite to 1023 K by Fizeau interferometry. *Physics and Chemistry of Minerals*. **12** 201-210.

McDonough, W. F. and S. S. Sun. (1995) The composition of the Earth. *Chemical Geology*. **120** (3-4): 223-253.

McGuire, A. V., C. A. Francis and M. D. Dyar. (1992) Mineral standards for electron microprobe analysis of oxygen. *American Mineralogist*. **77** (9-10): 1087-1091.

Mysen, B. O., D. H. Eggler, M. G. Seitz and J. R. Holloway. (1976) Carbon dioxide in silicate melts and crystals 1. Solubility measurements. *American Journal of Science*. **276** (4): 455-479.

Palme, H. and H. S. C. O'Neill. (2003) Cosmochemical estimates of mantle composition, pp. 1-38. In *The Mantle and Core* (ed. R. W. Carlson) Vol. 2 *Treatise on Geochemistry* (eds. H. D. Holland and K. K. Turekian), Elsevier-Pergamon, Oxford.

Pan, V., J. R. Holloway and R. L. Hervig. (1991) The pressure and temperature dependence of carbon dioxide solubility in tholeiitic basalt melts. *Geochimica et Cosmochimica Acta*. **55** (6): 1587-1595.

Ringwood, A. E. (1966) The chemical composition and origin of the Earth, pp. 287-356. In *Advances in Earth Science* (ed. P. M. Hurley), M. I. T. Press, Cambridge, MA.

Ringwood, A. E., S. E. Kesson, W. Hibberson and N. Ware. (1992) Origin of Kimberlites and Related Magmas. *Earth and Planetary Science Letters*. **113** (4): 521-538.

Shartsis, L., S. Spinner and W. Capps. (1952) Density, expansivity, and viscosity of molten alkali silicates. *Journal of the American Ceramic Society*. **35** (6): 155-160.

Shaw, A. M., M. D. Behn, S. E. Humphris, R. A. Sohn and P. M. Gregg. (2010) Deep pooling of low degree melts and volatile fluxes at the 85°E segment of the Gakkel Ridge: Evidence from olivine-hosted melt inclusions and glasses. *Earth and Planetary Science Letters*. **289** 311-322.

Smyth, J. R. (1975) High temperature crystal chemistry of fayalite. *American Mineralogist*. **60** 1092-1097.

Sparks, R. S. J., L. Baker, R. J. Brown, M. Field, J. Schumacher, G. Stripp and A. Walters. (2006) Dynamical constraints on kimberlite volcanism. *Journal of Volcanology and Geothermal Research*. **155** (1-2): 18-48.

Stolper, E. and J. R. Holloway. (1988) Experimental determination of the solubility of carbon dioxide in molten basalt at low pressure. *Earth and Planetary Science Letters*. **87** (4): 397-408.

Sumino, Y. (1979) The elastic constants of Mn_2SiO_4, Fe_2SiO_4, and Co_2SiO_4, and the elastic properties of olivine group minerals at high temperatures. *Journal of Physics of the Earth*. **27** 209-238.

Suzuki, A. and E. Ohtani. (2003) Density of peridotite melts at high pressure. *Physics and Chemistry of Minerals*. **30** (8): 449-456.

Suzuki, I. (1975) Thermal expansion of periclase and olivine, and their anharmonic properties. *Journal of Physics of the Earth*. **23** 145-159.

Suzuki, I., O. L. Anderson and Y. Sumino. (1983) Elastic properties of a single-crystal forsterite Mg_2SiO_4, up to 1,200K. *Physics and Chemistry of Minerals*. **10** (1): 38-46.

Suzuki, I., K. Seya, H. Takei and Y. Sumino. (1981) Thermal expansion of fayalite, Fe_2SiO_4. *Physics and Chemistry of Minerals*. **7** (2): 60-63.

Takahashi, E. (1986) Melting of a dry peridotite KLB-1 up to 14 GPa - Implications on the origin of peridotitic upper mantle. *Journal of Geophysical Research-Solid Earth and Planets*. **91** (B9): 9367-9382.

Taran, Y., T. P. Fischer, B. Pokrovsky, Y. Sano, M. A. Armienta and J. L. Macias. (1998) Geochemistry of the volcano-hydrothermal system of El Chichon Volcano, Chiapas, Mexico. *Bulletin of Volcanology*. **59** (6): 436-449.

Taylor, W. R. (1990) The dissolution mechanism of CO_2 in aluminosilicate melts - Infrared spectroscopic constraints on the cationic environment of dissolved $[CO_3]^{2-}$. *European Journal of Mineralogy*. **2** (5): 547-563.

Thibault, Y. and J. R. Holloway. (1994) Solubility of CO_2 in a Ca-rich leucitite - Effects of pressure, temperature, and oxygen fugacity. *Contributions to Mineralogy and Petrology*. **116** (1-2): 216-224.

Tomlinson, J. W., M. S. R. Heynes and J. O. Bockris. (1958) The structure of liquid silicates 2. Molar volumes and expansivities. *Transactions of the Faraday Society*. **54** (12): 1822-1833.

Turekian, K. K. and S. P. Clark. (1975) The non-homogeneous accumulation model for terrestrial planet formation and the consequences for the atmosphere of Venus. *Journal of the Atmospheric Sciences*. **32** 1257-1261.

Vinet, P., J. H. Rose, J. Ferrante and J. R. Smith. (1989) Universal features of the equation of state of solids. *Journal of Physics-Condensed Matter*. **1** (11): 1941-1963.

Wallace, M. E. and D. H. Green. (1988) An experimental determination of primary carbonatite magma composition. *Nature*. **335** (6188): 343-346.

Wendlandt, R. F. and B. O. Mysen. (1980) Melting phase relations of natural peridotite + CO_2 as a function of degree of partial melting at 15kbar and 30kbar. *American Mineralogist*. **65** (1-2): 37-44.

Wyllie, P. J. and I. D. Ryabchikov. (2000) Volatile components, magmas, and critical fluids in upwelling mantle. *Journal of Petrology*. **41** (7): 1195-1206.

Zhang, Y. X. and A. Zindler. (1993) Distribution and evolution of carbon and nitrogen in Earth. *Earth and Planetary Science Letters*. **117** (3-4): 331-345.